VOLUME 3, ISSUE 1, MARCH 2026

THE JOURNAL OF CRIS

Featured Article

Developing Online Analyzer for Monitoring of THPS-Based Biocides in Large Seawater Injection Network

p. 19

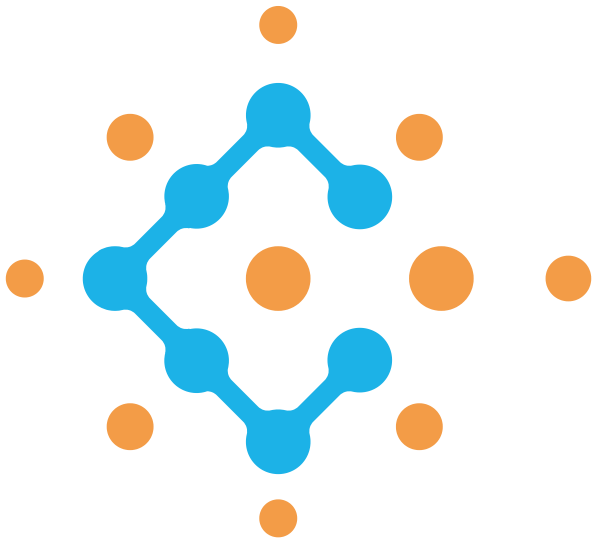

Table of **Contents**

Board Message

Dear Esteemed Readers,

It is with immense pride and excitement that we welcome you to the first issue of volume 3 of our society's technical journal. Building on the foundation laid in our inaugural issue, this edition signifies our unwavering commitment to fostering innovation, sharing knowledge, and strengthening connections within our professional community.

As our field continues to evolve, so too does the scope of ideas and challenges we face. This journal remains dedicated to providing a platform where groundbreaking research, practical insights, and diverse perspectives converge. It is our hope that these contributions spark dialogue, inspire action, and drive meaningful progress.

In this issue, you will find an enriched selection of articles that delve deeper into the complexities of our discipline. Each piece reflects the dedication and expertise of our contributors, as well as the collective vision of our society to lead and inspire. I encourage you to explore the content thoughtfully and consider how these insights might shape your work and broaden your understanding.

The success of this endeavor would not be possible without the support and collaboration of our authors, reviewers, and editorial team. Their hard work and passion have once again made this journal a testament to the vibrancy and depth of our community.
As we move forward, let us continue to celebrate the spirit of curiosity, innovation, and excellence that unites us. Thank you for your ongoing engagement and support. Together, we are shaping the future of our field.

Warm regards,

Letter From The Editor

Dear Colleagues,

Welcome to the first issue of Volume 3 of the Journal of Chemicals Research and Innovation Society. As we embark on another year of scientific exploration and knowledge sharing, we are excited to continue our mission of fostering groundbreaking research and collaboration in the chemical sciences.

Building on the foundation laid in our previous volumes, this issue presents a diverse collection of studies that showcase innovative methodologies, novel discoveries, and practical advancements across various fields of chemistry. Each contribution reflects the dedication and expertise of our research community, and we are proud to provide a platform for such impactful work.

I extend my deepest gratitude to our authors, reviewers, and editorial team for their unwavering commitment to excellence. Your contributions ensure that this journal remains a trusted source of scientific progress and a hub for meaningful discourse.

As we move forward, I encourage you to actively engage with the journal, whether through submitting your research, participating in discussions, or sharing insights with your peers. Together, we can continue to drive innovation and push the boundaries of chemical research.

Thank you for your continued support, and I look forward to the discoveries and advancements that lie ahead.

Best regards,

Shakeel Ahmed, Ph.D.,
Editor-in-Chief
Journal of Chemicals Research and Innovation Society

Emerging Viral Protease Inhibitors: Advances and Prospects for Broad-Spectrum Antiviral Therapy, Part I

Murtadha A. Alshaikh Jafar[2], Hussain H. Alsadah[2], Shah A. Khan[3], Ohood K. Almuzaini[4], Saad M. Wali[4], Samar A. Abubshait[5,6], Abir S. Abdel-Naby[1], Hagar H. Alhaddad[1], Abdulaziz H. Al Khzem[1], Mohammed F. Aldawsari[7], Shaima M. AlHejji[8], and Mansour S. Alturki[1,*]

[1]Department of Pharmaceutical Chemistry, College of Pharmacy, Imam Abdulrahman Bin Faisal University, Dammam Saudi Arabia

[2]College of Pharmacy, Imam Abdulrahman Bin Faisal University, Dammam, Saudi Arabia

[3]College of Pharmacy, National University of Science and Technology, Muscat, Oman

[4]Department of Pharmacology and Toxicology, Umm Al-Qura University, Makkah

[5]Department of Chemistry, College of Science, Imam Abdulrahman Bin Faisal University, Dammam, Saudi Arabia

[6]Basic and Applied Scientific Research Center, Imam Abdulrahman Bin Faisal University, Dammam, Saudi Arabia

[7]Department of Pharmaceutics, College of Pharmacy, Prince Sattam Bin Abdulaziz University, Al-kharj, Saudi Arabia

[8]Department of Pharmaceutical Sciences, College of Clinical Pharmacy, King Faisal University, Al-Ahsa, Saudi Arabia

* Correspondence: msalturki@iau.edu.sa

1. Abstarct

Background/Objective: Since the emergence of SARS-CoV-2, there has been heightened global attention on viral infections and the urgent need for novel antiviral therapies. This study focuses on recent advancements in the development of novel protease inhibitors that target a critical stage of the viral life cycle. **Methods:** PubMed and Google Scholar search engines were used in August 2025 to identify relevant studies published between 2020 and 2025. **Results:** Various in silico, in vitro, and in vivo studies were selected to identify novel viral protease inhibitors. Many studies on SARS-CoV-2 Mpro have reported compounds with inhibitory activity in the micromolar to nanomolar range. Several investigational molecules have been shown to potently suppress viral replication. Inhibitors directed at both catalytic (active) and allosteric (non-competitive) sites have also been explored, enabling the discovery of structurally diverse compounds with the potential for broad-spectrum antiviral activity. **Conclusions:** Mpro and PLpro have emerged as the most extensively studied viral proteases, reflecting a focus driven by the urgency of the pandemic. Several compounds have demonstrated promising

inhibitory activities. While other viral proteases remain less explored, they represent valuable targets for further investigation and optimization of antiviral therapy. The compound libraries generated through these efforts may serve as a critical foundation for developing the next generation of antivirals.

Keywords: SARS-CoV-2; MPro; Main protease; Protease inhibitors.

2. Introduction

Viruses are intracellular parasites that depend on host cells for reproduction. Once inside, they remove their capsids, transcribe and translate their RNA, replicate their genomes, assemble new virions, and release them. Viral proteases, which are enzymes encoded by the virus, cleave specific peptide bonds in viral or host proteins, a process essential for viral maturation. These proteases employ serine, cysteine, and aspartic acid residues for catalysis. [1-2] Recent viral research, especially during the SARS-CoV-2 pandemic, has highlighted viral proteases as promising targets for the development of antiviral drugs.

SARS-CoV-2 proteases

SARS-CoV-2 uses several proteases in its replication cycle, including the main protease (Mpro or 3CLpro), papain-like protease (PLpro), and host enzyme TMPRSS2.

Mpro is a cysteine protease functioning as a homodimer, each protomer containing three domains. Domains I and II form β-barrels resembling trypsin-like serine proteases, whereas Domain III has five α-helices linked by a loop. The N-terminal “finger” helps form the substrate-binding cleft between Domains I and II, where the catalytic dyad (His41 and Cys145) is located. [3] Its active site has five sub-pockets (S1–S5), with substrate selectivity mainly determined by the P1, P2, and P1′ residues. Although Mpro contains 12 cysteines, only Cys85, Cys145, and Cys156 are solvent-exposed, and Cys300 serves as an allosteric site. [4]

PLpro consists of four subdomains: an N-terminal ubiquitin-like domain, a thumb domain, a finger domain, and a palm domain. The Finger domain features a zinc ribbon motif formed by four conserved cysteines (C189, C192, C224, and C226). Its catalytic triad (C111, H272, and D286) drives proteolysis. The BL2 loop can shift to a closed conformation, thereby reducing inhibitor access to the active site. [5]

Transmembrane Serine Protease 2 (TMPRSS2) is a human serine protease crucial for SARS-CoV-2 entry. It activates the viral spike (S) protein by cleaving it at the S1/S2 site (RRAR685) and other positions, such as Arg815/Ser816 (S2′) and the T1/T2 regions, enabling membrane fusion. X-ray studies (1.95 Å resolution) revealed a catalytic triad — Ser441, His296, and Asp345 — responsible for proteolytic activity. Structural and computational analyses have highlighted additional substrate-binding sites (S2–S4) and key residues, such as Asp435, Lys342, and Gln438, which define substrate recognition and specificity. [6]

PLpro consists of four subdomains: an N-terminal ubiquitin-like domain, a thumb domain, a finger domain, and a palm domain. The Finger domain features a zinc ribbon motif formed by four conserved cysteines (C189, C192, C224, and C226). Its catalytic triad (C111, H272, and D286) drives proteolysis. The BL2 loop can shift to a closed conformation, thereby reducing inhibitor access to the active site. [5]

Transmembrane Serine Protease 2 (TMPRSS2) is a human serine protease crucial for SARS-CoV-2 entry. It activates the viral spike (S) protein by cleaving it at

the S1/S2 site (RRAR685) and other positions, such as Arg815/Ser816 (S2′) and the T1/T2 regions, enabling membrane fusion. X-ray studies (1.95 Å resolution) revealed a catalytic triad—Ser441, His296, and Asp345—responsible for proteolytic activity. Structural and computational analyses have highlighted additional substrate-binding sites (S2–S4) and key residues, such as Asp435, Lys342, and Gln438, which define substrate recognition and specificity. [6]

This review compiles research from 2020 to 2025, focusing on characterizing viral proteases to support the design and discovery of novel viral protease inhibitors. This section focuses on SARS-CoV2 Mpro/3CLpro inhibitors. The second part will target SARS-CoV2 proteases and include DENV, HCV, Norovirus, HIV-1, ZIKV, and HSV-1.

We used Google Scholar and PubMed search engines to identify as many papers as possible related to viral protease inhibition from 2020 to 2025. Articles were searched in August 2025. Figure 1 illustrates the PRISMA flow diagram. Elicit AI for scientific research was used as a tool to assist in collecting data and revising the extracted data. We screened sources to meet these criteria: (Inclusion & Exclusion criteria)

a.Novel Viral Protease Inhibitors: Does this study report the discovery or identification of novel viral protease inhibitors?
b.Optimization studies and reviews were excluded .
c.Protease Inhibition Mechanism: Does this study demonstrate antiviral activity specifically through the protease-inhibitionmechanism?
d.Study Design: Is this study an original research article?
e.Publication Timeframe: Was study published between January 2020 and August 2025?
f.Novel vs. Established Inhibitors: Does this study focus on novel inhibitors or established inhibitors with novel modifications (rather than solely on previously known inhibitors without modifications)?
g.Antiviral Application: Does this study investigate protease inhibitors for anti-viral applications (rather than non-viral applications)?
h.Studies evaluating previously known molecules were excluded .

3. Results and Discussion

SARS-CoV2 proteases Mpro/3CLpro inhibitors:

Extensive virtual screening, molecular docking, molecular dynamics (MD) simulations, and high-throughput biochemical assays have identified both natural products and FDA-approved drugs with potential inhibitory effects against SARS-CoV-2 Mpro, an enzyme crucial for viral polyprotein processing.

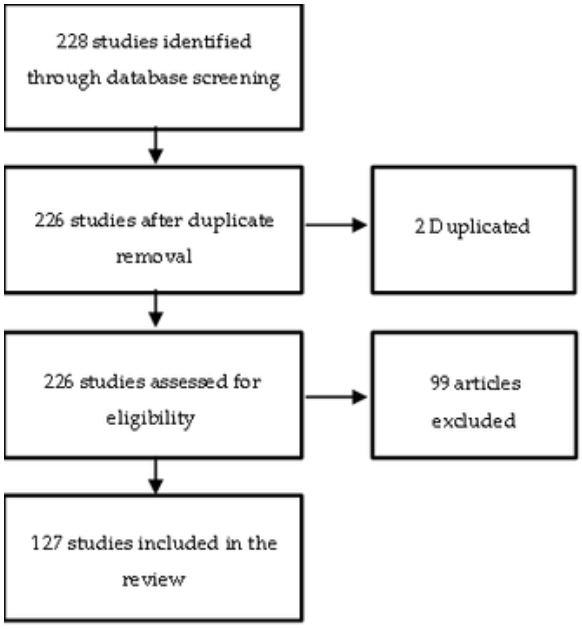

Figure 1. Review PRISMA.

Screening of 1200 FDA-approved compounds using FlipGFP-3CLpro and FRET-based 3CLpro assays in 293T, VeroE6/TMPRSS2, and human intestinal organoids (HIOs) identified three potent inhibitors:

- Auranofin (IC_{50} = 2.6 μM)
- Endoxifen (IC_{50} = 2.6–13.1 μM)
- Pimozide (IC_{50} = 2.6–13.1 μM)

These compounds inhibited replication of both SARS-CoV-2 and human norovirus (HuNoV), showing strong repurposing potential. Among them, endoxifen and pimozide were the most effective, with endoxifen showing possible multi-target activity, including inhibition of PLpro and viral entry factors. The study suggests further research is needed to clarify mechanisms and drug–host interactions due to assay discrepancies. [7]

Structure-based screening of 3987 FDA-approved drugs identified six inhibitors of SARS-CoV-2 Mpro, with IC_{50} values ranging from 21.5 to 75.5 μM: Boceprevir, Ombitasvir, Paritaprevir, Tipranavir, Ivermectin, and Micafungin. Binding interactions include:

- Cys145: Boceprevir, Tipranavir, Ivermectin
- Cys145 & His41: Paritaprevir
- Glu166: Ombitasvir, Micafungin

Among these, ivermectin emerged as the most promising candidate, fully inhibiting 3CLpro (IC_{50} = 21.53 μM) and requiring the homodimeric form of the enzyme for activity — a distinct functional feature. [8]

Natural compound inhibitors from Ashwagandha, Structure-based virtual screening, and 100 ns MD simulations revealed four withanolides — Withanoside II, IV, V, and Sitoindoside IX — with strong binding affinities (–62.5 to –87.0 kcal/mol). Withanoside V was the most potent, showing stable interactions with the catalytic dyad His41–Cys145 and surrounding residues (Met49, Leu141, Phe140, Met165, Leu167, and Pro168). Its selectivity and strong binding suggest its potential as a clinically developable antiviral agent against SARS-CoV-2. [9]

Docking and MD simulations of 50 natural coumarins against SARS-CoV-2, SARS-CoV, and MERS-CoV Mpro structures identified glycycoumarin as the best hit (binding energy, – 11.89 kcal/mol; free energy, – 60.31 kJ/mol). Hydrogen bonds were formed with His41, Cys145, Ser144, Gln189, Asn142, His164, and Glu166. It is predicted to have good absorption and plasma distribution; however, possible interactions with CYP450-metabolized drugs require further study. [10]

Virtual screening of natural compounds revealed that peonidin-3-O-glucoside and quercetin-3-O-α-L-arabinopyranoside are potent inhibitors with a strong affinity for Glu166, a residue critical for substrate binding. These compounds demonstrated higher dynamic stability than the control inhibitor, N3, indicating their promising antiviral potential. [11]

Biochemical high-throughput screening and Fluorescent HTS identified 13 inhibitors (IC_{50} = 0.2–23 μM) targeting Mpro's cysteine catalytic dyad:

Table 1. IC50 values of inhibitors of SARS-CoV-2 Mpro hits.

Compound	IC50 (μM)
Thimerosal	0.6 ± 0.1
Phenylmercuric acetate	0.4 ± 0.06
Bronopol	4.4 ± 0.6
Tannic acid	2.1 ± 0.2
Hematoporphyrin	3.9 ± 0.6

3,4-Didesmethyl-5-deshydroxy-3′-ethoxyscleroin	10.6 ± 1.3
2,3,4-Trihydroxy-4′-ethoxybenzophenone	9.0 ± 1.5
Chloranil	4.1 ± 0.8
Plumbagin	17.1 ± 9
Vanitiolide	4.6 ± 0.6
Evans blue	0.2 ± 0.06
Chicago Sky Blue	7.7 ± 1.6
Protoporphyrin IX	23 ± 2.4

Competitive inhibition analysis confirmed that Evans blue, tannic acid, and phenylmercuric acetate act by binding near the Cys145 catalytic residue. [12]

Docking and MD simulations of 20 neem seed compounds against multiple viral targets found:
·Desacetylgedunin → active against Mpro and ACE2
·Azadiradione → binds to the spike protein
·Azadirachtin H → inhibits RNA-dependent RNA polymerase (RdRp)
These compounds demonstrated comparable binding energies to lopinavir and remdesivir, indicating multi-target antiviral potential. [13]

Acanthus montanus phytochemicals natural compounds — Kaempferol, Quercetin, Naringin, Rutin, Progesterone, and Stigmasterol — showed strong binding with key residues in viral or host enzymes.
·Naringin: hydrogen bonds with Ala348, Glu398, Asn394, Gly395, Asn397
·Rutin: multiple H-bonds including Asn394, Gly395, Tyr515, Arg514
·Quercetin: H-bonds with Phe390, Asn394, Asp382
·Stigmasterol & Progesterone: mainly hydrophobic interactions
These interactions suggest moderate inhibitory potential through non-covalent stabilization. [14]

Salvianolic acid A and curcumin exhibited strong docking scores (–9.7 and –9.2 kcal/mol, respectively) with a high affinity for Glu166 and Cys145. Salvianolic acid A exhibited a dominant electrostatic binding energy (–65.5 kcal/mol) and stronger activity than that of lopinavir. [15] Rutin, identified through blind docking on PDB 6Y84, had a binding energy of–9.55 kcal/mol with H-bonds to His41, Leu141, Glu166, Gln192, and π–sulfur interaction with Cys145, outperforming ritonavir in terms of docking affinity. [16]

Natural compounds such as Withanoside V, Glycycoumarin, Rutin, Salvianolic acid A, and Desacetylgedunin, alongside FDA-approved molecules such as endoxifen, pimozide, and ivermectin, show strong potential to inhibit SARS-CoV-2 Mpro through stable interactions with the catalytic dyad (His41–Cys145) and key residues (Glu166, Gln189, and Met165). [7-16] These findings support further in vitro, crystallographic, and animal model validation to assess the therapeutic viability of these compounds against COVID-19 and related coronaviruses.

Extensive structure-based virtual screening (SBVS) and molecular dynamics (MD) simulations have been widely employed to identify potent and selective Mpro inhibitors. Collectively, these studies consistently target the catalytic dyad His41–Cys145 and the S1/S2 binding pockets, with a strong focus on optimizing binding affinity, stability, and pharmacokinetics.

Virtual screening of 1,000 protease-like molecules led to the identification of two [1,2,4]-triazolopyrimidin-7-one derivatives , ZINC000621278586 and ZINC000621285995, which strongly

interacted with His41 and Cys45 and displayed stable binding energies (–129.3 and –116.5 kJ/mol, respectively). ZINC000621278586 is superior owing to its low toxicity and non-inhibition of cytochrome P450 enzymes [17]. Screening of the Specs compound library identified four novel scaffolds exhibiting micromolar IC_{50} values: AG-690/13507628 (2.806 μM), AG-690/13507724 (2.961 μM), AG-690/13507757 (19.19 μM), and AG-690/13508164 (16.905 μM, low cytotoxicity; π-π stacking with His41 and hydrogen bonding with Thr25 and Asn142 were key for activity) [18].

A large-scale fragment-guided screening of 235 million compounds yielded noncovalent inhibitors with nanomolar affinities and broad-spectrum antiviral activities. Compound 19 (IC_{50} = 0.077 μM) emerged as the most potent, exhibiting nanomolar activity, favorable pharmacokinetics, and human protease selectivity [19].

Natural Product-Derived and Polyphenolic Inhibitors from Siparuna glycycarpa, the aporphine alkaloid bulbocapnine, inhibited 3CLpro, PLpro, and Spike proteins and demonstrated strong stability and favorable ADMET properties [20]. Six polyphenols from Broussonetia papyrifera, notably kazinol F, showed high binding affinity (–56.23 kcal/mol) and stable interactions with His41 and Cys145, supported by hydrogen, π–σ, and van der Waals contacts [21].

High-throughput screening of quinazolinone derivatives identified compound 9b (IC_{50} ≈ 10 μM) that interacts with His41, Cys145, and Glu166; however, limited absorption and drug-likeness suggested the need for optimization [22].

A deep learning-based covalent/noncovalent classifier screened ~39,000 compounds and identified six covalent scaffolds that bind Cys145; compound 13 showed optimal reactivity (IC_{50} = 4.9 μM) and selectivity for coronavirus proteases [23].

Further machine learning and docking on 5,903 ZINC compounds discovered multitarget inhibitors (Spike, 3CLpro, Nucleocapsid); ZINC003873365 displayed the highest affinities (–19.7 to –15.1 kcal/mol) [24].

Fragment-based and advanced AI approach screening of 360 compounds identified compound 13, with nanomolar activity (30–50 nM) against Omicron and 229E strains, showing synergistic antiviral effects and strong binding at His41, Met165, and Asn142 [25]. Compound A also exhibited low binding energy and robust interactions with Cys145 and Glu166 [26].

An advanced Q-learning–based fragment design (ADQN-FBDD) approach was used to generate compound #46, which formed covalent bonds with Cys145 and hydrogen bonds with Gly143 and Glu166. Optimized analogs 46-14-1, 46-14-2, and 46-14-3 were proposed to enhance polarity and flexibility [27].

Natural screenings identified withacoagulin H from Withania (IC_{50} = 6.82 nM) [28] and ZINC19286315 (–6.2 kcal/mol) as stable binders [29]. Pharmacophore modeling produced compounds 21–22 with micromolar activity, hydrogen bonding to His163 and Asn142, and moderate intestinal absorption. [30]. Screening of the ASINEX library yielded compound 23 (IC_{50} = 2.8 μM), which was enhanced by CF_3 and acetamide substitutions [31].

STL522228, identified via screening of FDA-approved and natural libraries,

displayed potent Mpro inhibition (IC_{50} = 2.5 μM, Kd = 31.2 nM), superior antiviral activity to remdesivir, and strong binding at His41, Gln189, and Glu166 [32]. Compound 25 covalently binds to Cys145 and shows metabolic stability but low solubility [33].

The dual-target inhibitor VK13 potently inhibited both cathepsin L (Ki = 0.55 nM) and 3CLpro (Ki = 2.6 nM) through specific interactions with Glu166, His163, and Gln189 [34]. SIMR-2418 binds noncovalently and covalently to Cys145 and His41 (IC_{50} = 8.9 μM) [35].

High-throughput screening identified azanitrile 28 and pyridyl ester 29 with sub-100 nM affinities for Cys145 acylation [36]. Covalent inhibitors, such as compound 30, achieved potency comparable to that of GC376, confirming that alkynylamide warheads and heterocyclic rings enhance activity [37].

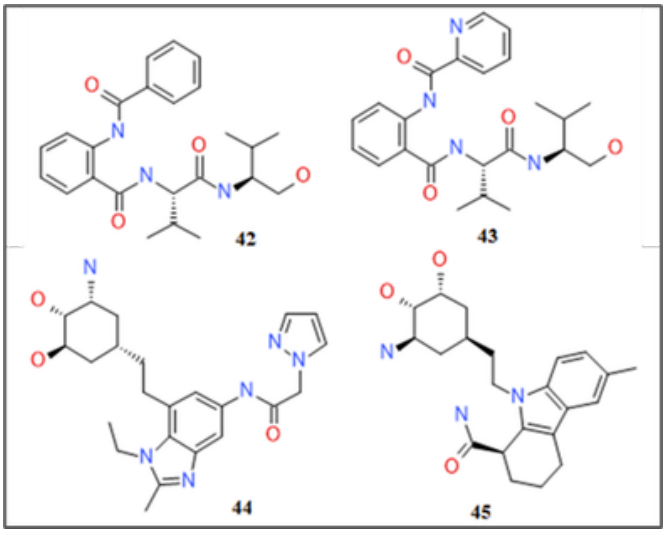

Nonpeptide, Phytochemical, and DrugBank Hits, Ensemble docking pinpointed compound 31 (IC_{50} = 0.69 μM) with favorable binding (–48.01 kcal/mol) via Gly143, Ser144, and Cys145 contacts [38]. Phytochemicals, including ursolic acid, carvacrol, and oleanolic acid, exhibited moderate binding (–4 to –6 kcal/mol) through hydrogen bonds and hydrophobic interactions [39]. Usnic acid exhibited stable inhibition (–8.6 kcal/mol) via hydrogen and π–π interactions with His41 and Glu166 [40], respectively.

DrugBank screening revealed thiophene sulfonamide inhibitors (3-[(4-chloroanilino) sulfonyl] thiophene-2-carboxylic acid) and (N-(2-thienylmethyl)-2,5-thiophenedisulfonamide) with stronger Mpro binding and safety profiles than lopinavir or ritonavir [41].

The largest computational study (606 million molecules) identified 12 small-molecule inhibitors adhering to Lipinski and Veber criteria; compound 38 in figure.1 showed the highest ligand efficiency, surpassing the co-crystallized inhibitor N3 [42].

Figure 1.

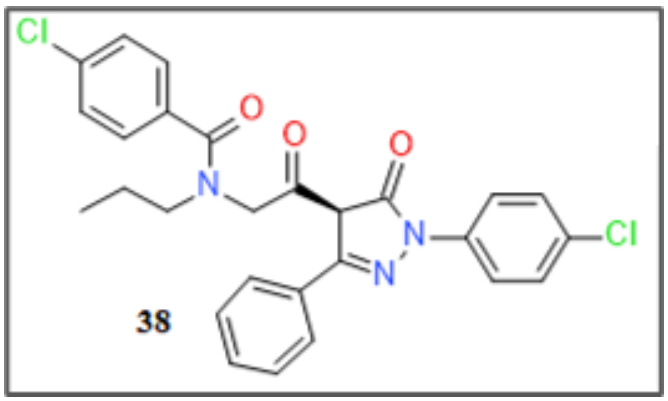

Subsequent ligand- and structure-based screening of commercial libraries produced optimized compounds 42 and 43 (figure.2, which demonstrated strong specificity for SARS-CoV-2 (IC_{50} ≈ 40 μM, EC_{50} ≈ 1–2 μM) and robust hydrogen bonding with residues C145, S144, and H163 [43].

Extensive fragment-based virtual screening of 191,678 fragments and subsequent fragment linking, docking (Glide), ADMET filtering, MM-GBSA energy calculations, and MD simulations yielded 15 SARS-CoV-2 Mpro inhibitors with binding energies ranging from −70.00 to −80.97 kcal/mol.

Compounds 44 and 45 in figure.2 formed stable complexes via hydrogen bonds with G143, S144, C145, E166, Q189, and T190 and were identified as potent candidates [44].

Extensive fragment-based virtual screening of 191,678 fragments and subsequent fragment linking, docking (Glide), ADMET filtering, MM-GBSA energy calculations, and MD simulations yielded fifteen SARS-CoV-2 Mpro inhibitors with binding energies from −70.00 to −80.97 kcal/mol. Compounds 44 and 45 in figure.2 formed stable complexes via hydrogen bonds with G143, S144, C145, E166, Q189, and T190, and were identified as potent candidates [44].

Figure 2

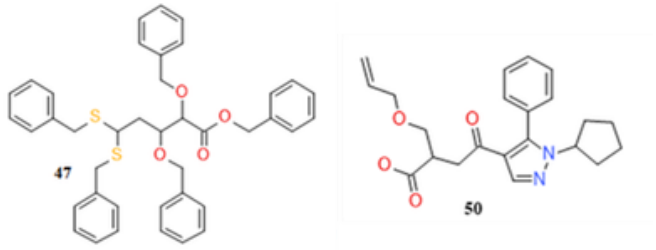

Virtual screening of over 3.5 million Enamine and Specs compounds identified two molecules, 46 and 47, with 47.11% and 37.67% inhibition at 100 μM, and MM/GBSA values of −66.07 and −78.32 kcal/mol, respectively. Compound 47 in figure.3 exhibited superior binding free energy and lower toxicity (LD_{50} = 2000 mg/kg), while 46 formed π–π stacking with His41 and hydrogen bonds with Gln189, Gln192, Thr190, and Arg188 [45].

High-throughput screening of 1280 pharmacologically active compounds revealed 65 inhibitors, with the top 20 showing submicromolar inhibition. Ebselen (EC_{50} = 27 nM), PD 404,182, ZPCK, and aporphine alkaloids demonstrated strong inhibition through covalent or hydrogen bonding with Cys145 and Q189 residues.

Ebselen was most potent, forming a selenosulfide bond with thiol residues [46]. Further screening confirmed Ebselen as a covalent inhibitor (IC_{50} = 0.67 μM), forming bonds with Cys145 and van der Waals contacts with T24–T25, demonstrating excellent safety (LD_{50} > 4600 mg/kg) [47].

Structure-guided design yielded spirocyclic inhibitors targeting SARS-CoV-2 and MERS-CoV 3CLpro active sites via H-bonding with His41, Glu166, and Gln189. Compound 10b (IC_{50} = 0.24 ± 0.01 μM, Safety Index ≈1250) was most active but exhibited partial non-selectivity due to Cathepsin L inhibition [48].

Pharmacophore modeling and screening of 213.5 million compounds identified 5 hits with binding free energies between −11.65 and −7.90 kcal/mol. Compound 50 in figure.3 displayed superior affinity through van der Waals and H-bond interactions with His41, Cys145, Met165, and Glu166, though optimization is required to enhance ADMET and potency [49].

Heterocyclic derivatives analyzed via docking, DFT, and MD simulations showed C4 and C5 as potent binders (−8.6 and −8.0 kcal/mol). 55 formed H-bonds with Glu166 and His44, while 56 interacted with Cys145, Met49, and Met165 [50].

Among 38 flavonoids, three glycosylated types — Quercetin-3-O-rhamnoside, Myricetin 3-rutinoside, and Rutin — were predicted inhibitors (−9.7 to −9.2 kcal/mol). Rutin was most stable, binding via H-bonds with Thr26, His41, and Glu166, though bioavailability was limited by glycosylation [51].

A 10-million-compound screen from the Topscience database identified compound 34 (IC_{50} = 6.12 μM) and 36 (IC_{50} = 4.47 μM) as

potent Mpro inhibitors. Both form strong H-bonds with Gln189 and Thr190 and π–π interactions with His41. Toxicological profiling is still required [52].

In silico docking showed glabridin, catechin, and fisetin inhibited Mpro (−8.25 to −8.1 kcal/mol). Glabridin exhibited highest affinity via H-bonds with Glu166, Arg188, and Gly143 [53].

A deep learning model (MproI-GEN) generated novel inhibitors gen_1502 and gen_3854 with ΔG < −45 kcal/mol. Both formed strong H-bonds with catalytic residues (Cys145, Glu166, and His163), showing promising target specificity [54].

DFT and docking identified a rhenium tricarbonyl complex 34 (IC_{50} = 7.5 μM) with selective Mpro inhibition; amine-functionalized analogs exhibited higher activity due to favorable charge interactions within the active site [55].

Dihydroindeno[1,2-b]pyrrol-4(1H)-one derivative 5f demonstrated −7.28 kcal/mol binding energy, forming multiple H-bonds and hydrophobic contacts within the active site [56].

Virtual screening of 688 naphthoquinoids identified 64 (Mpro IC_{50} = 0.41 μM) and 65 (PLpro IC_{50} = 1.9 μM) in figure.4. 64 acted as a reversible, selective Mpro inhibitor via polar and hydrophobic interactions at S1–S2 subsites [57].

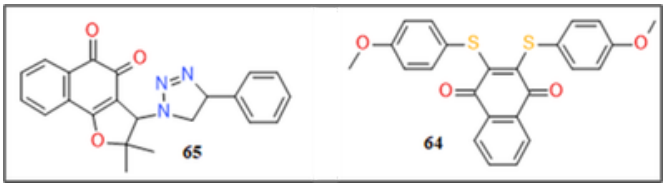

Figure 3

Repositioning norovirus inhibitors led to (NIP-22c) (IC_{50} = 165.7 nM), which retained potency against Mpro variants, including E166V mutants. It formed multiple hydrophobic and H-bond interactions with Glu166, His163, and Cys145 but showed rapid hepatic metabolism [58].

Affinity-based DNA-encoded library screening yielded three peptide-like covalent inhibitors (IC_{50} = 30–140 nM). Optimization produced MP1 (IC_{50} = 24 nM, EC_{50} = 2.3 μM), binding covalently to Cys145 and H-bonding with His163 and Glu166. Despite potency, poor metabolic stability and P-gp efflux were noted [59].

Pyrazolo[3,4-d]pyrimidin-4(5H)-one derivatives exhibited −7.5 to −8.2 kcal/mol affinities. Compound 8 inhibited Omicron Mpro (P132H) via H-bonds with Glu166, Asn142, and Cys145 [60].

Screening 149 polyphenols revealed 31 dual Mpro/PLpro inhibitors, with Taxifolin (Mpro) and Morin (PLpro) showing strongest affinities. Their hydroxyl and carbonyl groups at C3, C5, and C7 positions formed multiple H-bonds, defining key SAR features [61].

Isatin derivative screening (79 scaffolds, 15 million analogs) identified four hits (−8.6 to −8.4 kcal/mol) with good ADMET profiles, binding to His41, Cys145, and Glu166 at the Mpro catalytic dyad [62].

Consensus screening of 4.3 million ZINC compounds yielded a 2-thiobenzimidazole analog 26 (IC_{50} = 14.9 μM), interacting with Gly143, Ser144, and His41 within S1′ and oxyanion subpockets [63].

Daturataturin A and Daturametelin J from Datura spp. exhibited strong binding (−8.6 kcal/mol) and H-bonding with Asn142, Ser144, His163, and Glu166, though poor solubility and potential cardiotoxicity were noted [64].

Acyloxymethyl ketone-based compound 74 (IC_{50} = 230 nM) selectively inhibited Mpro by forming a reversible complex with His164 and Cys145, showing efficacy against Beta, Delta, and Omicron variants and synergy with remdesivir [65].

Repositioned SARS-CoV-1 inhibitors YH-53 and 75 showed full viral inhibition at 25 μM, with 75 in figure.5 forming covalent and H-bond interactions with Cys145, His163, and Glu166. Despite strong in vitro potency (IC_{50} ≈ 5 μM), bioavailability was limited by hepatic metabolism [66].

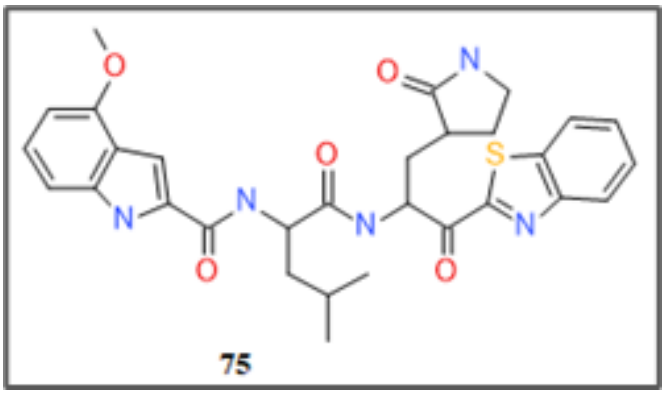

Figure 4

Cyanidin-3,5-di-O-glucoside (76), obtained from Punica granatum extract, bound to the catalytic residues Cys145 and His41 through hydrogen bonds, exhibiting inhibitory potential [67].

Ligand-based pharmacophore modeling and MD simulations identified (S,R)-(+)-fenoterol as a stable Mpro inhibitor, forming H-bonds with Gly143, Glu166, and Gln189 (ΔG = −55.55 kcal/mol) [68].

Pharmit-based screening of 60.2 million molecules led to the identification of compound M3, which formed H-bonds with Thr25, Gly143, Ser144, and Cys145, showing favorable pharmacokinetics and low predicted toxicity [69].

Selenium-containing benzisoselenazolone 1i inhibited Mpro with an IC_{50} of 87.64 nM via covalent bonding to Cys145. Despite their potency, non-specific cysteine reactivity and solubility issues have been noted [70].

FRET-based screening identified compound 1e (IC_{50} = 25 ± 3 μM) among six scaffolds that interacted with residues 141–145, His41, and Glu166. The triterpene backbone enhances hydrophobic stability [71].

Octahydroisochromene derivative 1e (IC_{50} = 95 μM) binds to the S2 pocket of 3CLpro through hydrophobic interactions, aligning imidazole and aldehyde groups to the active subpockets [72].

Finally, quantitative high-throughput screening (qHTS) of 10,755 compounds identified Walrycin B as the most potent inhibitor (IC_{50} = 0.26 μM), which binds to S1/S1′ near Cys145 and effectively blocks SARS-CoV-2 replication [73].

3. Results and Discussion

Extensive high-throughput screening, structure-based virtual screening, and molecular dynamics studies have identified a diverse range of SARS-CoV-2 main protease (Mpro/3CLpro) inhibitors, including FDA-approved drugs, synthetic scaffolds, and natural products. Most active compounds consistently target the catalytic dyad His41–Cys145 and adjacent residues, such as Glu166, Gln189, Met165, and Thr190, confirming these as critical pharmacophore regions.

Repurposed drugs such as ivermectin, endoxifen, pimozide, boceprevir, and auranofin have demonstrated measurable inhibitory activity, while Ebselen and GC376 have repeatedly served as benchmark covalent inhibitors. Natural metabolites, including Withanoside V, Glycycoumarin, Rutin, Salvianolic acid A, and Desacetylgedunin, exhibited high binding

affinities and stable conformations, supporting their potential as safe antiviral scaffolds.

Advanced AI-driven and fragment-based discovery approaches have further yielded nanomolar-range noncovalent inhibitors with improved pharmacokinetics and selectivity. Collectively, these findings highlight Mpro as a robust antiviral target and provide a broad chemical foundation for future optimization, in vitro validation, and translational development of COVID-19 therapeutics.

References

1.Ryu, Wang-Shick. “Virus Life Cycle.” Molecular Virology of Human Pathogenic Viruses (2017): 31–45. doi:10.1016/B978-0-12-800838-6.00003-5

2.Steinkühler, Christian. "Viral proteases." Encyclopedia of molecular Pharmacology. Springer, Berlin, Heidelberg, 2008. 1284-1287.

3.Ullrich, Sven, and Christoph Nitsche. "The SARS-CoV-2 main protease as drug target." Bioorganic & medicinal chemistry letters 30.17 (2020): 127377.

4.Hu, Qing, et al. "The SARS-CoV-2 main protease (Mpro): structure, function, and emerging therapies for COVID-19." MedComm 3.3 (2022): e151.

5.Gao, Xiaopan, et al. "Crystal structure of SARS-CoV-2 papain-like protease." Acta Pharmaceutica Sinica B 11.1 (2021): 237-245.

6.Fraser, Bryan J., et al. "Structure and activity of human TMPRSS2 protease implicated in SARS-CoV-2 activation." Nature chemical biology 18.9 (2022): 963-971.

7.Hayashi, Tsuyoshi, et al. "Identification of FDA-Approved Drugs That Inhibit SARS-CoV-2 and Human Norovirus Replication." Biological and Pharmaceutical Bulletin 48.7 (2025): 994-1000.

8.Mody, Vicky et al. “Identification of 3-chymotrypsin like protease (3CLPro) inhibitors as potential anti-SARS-CoV-2 agents.” Communications biology vol. 4,1 93. 20 Jan. 2021

9.Tripathi, Manish Kumar, et al. "Identification of bioactive molecule from Withania somnifera (Ashwagandha) as SARS-CoV-2 main protease inhibitor." Journal of Biomolecular Structure and Dynamics 39.15 (2021): 5668-5681.

10.Abdizadeh, Rahman, Farzin Hadizadeh, and Tooba Abdizadeh. "In silico analysis and identification of antiviral coumarin derivatives against 3-chymotrypsin-like main protease of the novel coronavirus SARS-CoV-2." Molecular Diversity 26.2 (2022): 1053-1076.

11. Majumder, Ranabir, and Mahitosh Mandal. "Screening of plant-based natural compounds as a potential COVID-19 main protease inhibitor: an in silico docking and molecular dynamics simulation approach." Journal of Biomolecular Structure and Dynamics 40.2 (2022): 696-711.

12. Coelho, Camila, et al. "Biochemical screening for SARS-CoV-2 main protease inhibitors." PloS one 15.10 (2020): e0240079.

13. Singh, Kamalpreet, et al. "Virtual screening of compounds presents in Azadirachta indica (Neem) seed that can interfere with the targets of SARS-CoV-II viral entry, viral RNA replication, and post-translational modification of viral proteins."

14. Odunowo, Omobolaji. "In-silico Investigation and Potential Therapeutic Approaches of Acanthus montanus for COVID-19: Computer-aided Drug Design Perspective." Journal of Advances in Medicine and Medical Research 37.4 (2025): 327-343.

15. Ibrahim, Mahmoud AA, et al. "In silico drug discovery of major metabolites from spices as SARS-CoV-2 main protease inhibitors." Computers in Biology and Medicine 126 (2020): 104046.
16. Das, Sourav, et al. "An investigation into the identification of potential inhibitors of SARS-CoV-2 main protease using molecular docking study." Journal of Biomolecular Structure and Dynamics 39.9 (2021): 3347-3357.
17. Kavitha, Kuppuswamy, Subramaniam Sivakumar, and Balasubramanian Ramesh. "1, 2, 4 triazolo [1, 5-a] pyrimidin-7-ones as novel SARS-CoV-2 Main protease inhibitors: In silico screening and molecular dynamics simulation of potential COVID-19 drug candidates." Biophysical Chemistry 267 (2020): 106478.
18.Zheng, Lei, et al. "Discovery of novel inhibitors of SARS-CoV-2 main protease." Journal of Biomolecular Structure and Dynamics 40.23 (2022): 12526-12534.
19. Luttens, Andreas, et al. "Ultralarge virtual screening identifies SARS-CoV-2 main protease inhibitors with broad-spectrum activity against coronaviruses." Journal of the American Chemical Society 144.7 (2022): 2905-2920.
20. Gomes, Brendo Araujo, et al. "Predicting the Anti-SARS-CoV-2 Potential of Isoquinoline Alkaloids from Brazilian Siparunaceae Species Using Chemometric Tools." International Journal of Molecular Sciences 26.2 (2025): 633.
21. Ghosh, Rajesh, et al. "Identification of polyphenols from Broussonetia papyrifera as SARS CoV-2 main protease inhibitors using in silico docking and molecular dynamics simulation approaches." Journal of Biomolecular Structure and Dynamics 39.17 (2021): 6747-6760.
22. Hue, Bui Thi Buu, et al. "Discovery of a novel benzimidazole conjugated quinazolinone derivative as a promising SARS-CoV-2 3CL protease inhibitor." RSC advances 14.46 (2024): 33820-33829.
23. Wang, Liying, et al. "Discovery of novel SARS-CoV-2 3CL protease covalent inhibitors using deep learning-based screen." European journal of medicinal chemistry 244 (2022): 114803.
24. Aqeel, Imra, et al. "In-silico study of approved drugs as potential inhibitors against 3CLpro and other viral proteins of CoVID-19." PloS one 20.6 (2025): e0325707.
25. Pérez-Vargas, Jimena, et al. "A novel class of broad-spectrum active-site-directed 3C-like protease inhibitors with nanomolar antiviral activity against highly immune-evasive SARS-CoV-2 Omicron subvariants." Emerging microbes & infections 12.2 (2023): 2246594.
26. Khorsandi, Zahra, et al. "Design and synthesis of novel phe-phe hydroxyethylene derivatives as potential coronavirus main protease inhibitors." Journal of Biomolecular Structure and Dynamics 40.17 (2022): 7940-7948.
27. Tang, Bowen, et al. "AI-aided design of novel targeted covalent inhibitors against SARS-CoV-2." Biomolecules 12.6 (2022): 746.
28. Verma, Surjeet, Chirag N. Patel, and Muktesh Chandra. "Identification of novel inhibitors of SARS-CoV-2 main protease (Mpro) from Withania sp. by molecular docking and molecular dynamics simulation." Journal of computational chemistry 42.26 (2021): 1861-1872.
29. Kumar, Durgesh, et al. "Promising inhibitors of main protease of novel corona virus to prevent the spread of COVID-19 using docking and molecular dynamics simulation." Journal of Biomolecular Structure and Dynamics 39.13 (2021): 4671-4685.

30. Varadharajan, Venkatramanan, Gokulakrishnan Sivasundari Arumugam, and Sethupathi Shanmugam. "Isatin-based virtual high throughput screening, molecular docking, DFT, QM/MM, MD and MM-PBSA study of novel inhibitors of SARS-CoV-2 main protease." Journal of Biomolecular Structure and Dynamics 40.17 (2022): 7852-7867.
31. Deodato, Davide, Nadeem Asad, and Timothy M. Dore. "Discovery of 2-thiobenzimidazoles as noncovalent inhibitors of SARS-CoV-2 main protease." Bioorganic & Medicinal Chemistry Letters 72 (2022): 128867.
32. Onyango, Harrison, et al. "In Silico Identification of New Anti-SARS-CoV-2 Main Protease (Mpro) Molecules with Pharmacokinetic Properties from Natural Sources Using Molecular Dynamics (MD) Simulations and Hierarchical Virtual Screening." Journal of Tropical Medicine 2022.1 (2022): 3697498.
33. Poli, Adi NR, et al. "Design of novel and highly selective SARS-CoV-2 main protease inhibitors." Antimicrobial agents and chemotherapy 68.10 (2024): e00562-24.
34. Konno, Sho, et al. "3CL protease inhibitors with an electrophilic arylketone moiety as anti-SARS-CoV-2 agents." Journal of Medicinal Chemistry 65.4 (2021): 2926-2939.

Authors

Murtadha A. Alshaikh is a pharmacy graduate with research interests in medicinal chemistry and anticancer drug discovery.

Hussain H. Alsadah is a pharmacy graduate whose work focuses on experimental pharmacology and bioactive compound evaluation.

Saad M. Wali is working on experimental pharmacology and toxicological evaluation of bioactive agents.

Hagar H. Alhaddad is a researcher whose work centers on synthetic medicinal chemistry and biological screening.

Abdulaziz H. Al Khzem is specialized in heterocyclic synthesis and drug development.

Mansour S. Alturki is a researcher with expertise in anticancer drug discovery, EGFR inhibitors, and computer-aided drug design.

Shah A. Khan is specialized in medicinal chemistry and heterocyclic synthesis for therapeutic applications.

Ohood K. Almuzaini is an academic with research interests in molecular pharmacology and drug safety.

Samar A. Abubshait is focusing on biomolecular and spectroscopic analysis.

Abir S. Abdel-Naby is expert in medicinal chemistry and computational drug design.

Mohammed F. Aldawsari is an academic with research interests in nanocarriers and advanced drug delivery systems.

Shaima M. AlHejji is a clinical pharmacy student with interests in pharmacotherapy and translational pharmaceutical research.

Aspergillus fumigatiaffinis isolated from Madinah Date Palm Soil as a Promising mineral mycosolubilizer

Metwally Ramadan Kottb, Shaher Mohammad AL-Johani, Sultan Mustafa Khada – Bakhsh*
Biology Department, College of Science, Taibah University, Madinah, Saudi Arabia
Corresponding author*: Ssultanbaksh@gmail.com

Abstract

Microbial communities have a great role in an organic agricultural system due to their involvement in soil mineral cycles and solubilization processes. From the Quba Date organic farm at Madinah,Saudi Arabia, 21 isolated fungi from the soil and plants were identified based on colony morphology and microscopic investigation. One promising fungal species was molecularly identified as Aspergillus fumigatiaffinis MKSA3. Some fungal species, namely, Aspergillus niger, A. fumigatiaffinis, and Trichoderma longibrachiatum, showedgreat potentiality in urease production detected by pink color observation after cultivation on Christensen's Urea Agar. The ability of selected fungal species to produce siderophores "iron-chelating compounds" was evaluated by chrome azurol S (CAS) agar plate assay. Only Two species, A.fumigatiaffinis and Penicillium oxalicum showed positive siderophores detected by an orange color zone around the colonies in the CAS plate assay. Six selected fungalspecies were tested as solubilizers for Zinc oxide,results showed that A.fumigatiaffinis recorded the highest efficiency of 216% followed by A. flavus (178%). In addition, the solubilization of Tricalcium phosphate was assayed and the highest solubilization index recorded in A. fumigatiaffinis reached 3.4 after 7 days of incubation followedby A. ustus andA. niger. The solubilization efficiency of A. fumigatiaffinis could be attributed to their great ability for acid production which reached 3.05 after 6 days of incubation. The application of A.fumigatiaffinis in agriculture as an eco-friendly biofertilizer requires further investigations into the impact of this promising species on plant growth, productivity, and safety.

Keywords: Fungi- Quba – Siderophores- Urease- Solubilization

1. Introduction

Various crops associated with microorganisms in the cultivated soil were known for improving soil properties[1]. Microorganisms also positively affect plant growth[2] and induce plant defense mechanisms[3]. Several plant growth-promoting fungi (PGPF) are applied commercially to reduce the usage of agrochemicals[4]. Soil microorganisms, bacteria, and fungi are essential for enhancing soil health throughseveral mechanisms. Fungi play a part in improving soil structure by forming hyphalnetworks that hold soil particles together and increase aggregatestability. This aggregation enhances aeration, water retention, and nutrient availability while promoting plant development. Additionally, there are symbiotic relationships between plant roots and fungi. A mycorrhizal

connection is a kind of relationship that encourages the exchange of nutrients, particularly nitrogen and phosphorus. These interactions strengthen plants' tolerance to stressorslike disease and drought. Researchindicates that the functionality and biodiversity of soil can be enhanced by a diversity of fungal communities, hence increasing ecosystem services[5].

Several mechanisms are adopted by PGPF for improving plant growth, such as Siderophores biosynthesis[6], phytohormones production[7] or induction in plants[8], and increasing the bioavailability of insoluble nutrients due to mobilization[9]. Successful fungal species isolated from various cultivated soils were recorded as siderophore producers, such as Aspergillus and Penicillium[10], urease producers[11], Phosphate solubilizers[12], and Zinc solubilizers[13]. This study aimedto survey the fungal diversity in the Quba organic farm and test its physiological properties to select promising candidates for application in eco-friendly agriculture in the future.

MATERIALS AND METHODS

Study Site and Sample Collection

Three samples from rhizosphere soils, two from running irrigation water, and five palm plantleaves, were collected from the Quba date farm.It is situated near the Quba region at Madinah KSA, 24.4496°N, 39.6273° E. Soil sampleswere collected in March 2024, after removing organic litter, using clean, dry, and sterile polythene bags along with a sterile soil core of 10 cm diameter and 10 cm depth[14].

Figure 1. Location of sample collection

Isolation of Fungi

The samples were collected in sterile bags and bottles and immediately transferred to the laboratory for fungal isolation. The isolation medium used was Czapek's yeast autolysate CYA[15] supplemented with chloramphenicol and rose bengal to suppress bacterial growth. Dilutionplate techniques [16] briefly, ten grams from each samplewere suspended in 90 ml sterile water and stirred at room temperature for 15 min, then separately subjected to serial dilutionup to the 3 dilutionand used as primary inoculum for fungal isolation, in which each plant received 1ml from each dilution. Inoculated plates were in triplicate and kept in an incubator at 28±2°C for 7 days for consistent fungal count and colony color. The filamentous fungal colonies came into view, were counted, and then purified on Potato Dextrose Agar (PDA), incubated at 28±2°C, to ensure colony purity. The purified colonies were subjected to identification.

Identification of FungalIsolates

The pure culture of the isolated fungi was identified based on morphological characteristics with appropriate keys as follows: genus Aspergillus[17], for the general taxonomy of soil fungi[18], Emericella[19], and Penicillium[20]. The complete genomicDNA was extracted from mycelia using the DNA Isolation Kit (Quick-DNA™ Fungal/Bacterial Miniprep Kit) for molecular identification of one promising fungal isolate. The rDNA-ITS region was amplified by applying the universal fungal primers ITS1 and ITS2,[21]. Purified rDNAs were amplified, sequenced, and identified using BLAST programs at the NCBI database. The phylogenetic tree analysis has been performed using Molecular Evolutionary Genetics analysis (MEGA) software.

Fungal Urease Assay Test

Twenty-one fungal isolates were evaluated to produce urease through cultivation on Christensen's Urea Agar[22]. The medium contains Peptone 1 g, Sodium chloride 5 g, Dextrose 1 g, Potassium phosphate, monobasic 2 g, and Urea 20 g, sterilized by filtration and added to the medium after autoclaving. Phenol red 0.012 g, and Agar 15 g.

Detection of Fungal Siderophore Production

The capability of selected fungal species for siderophore excretion (iron-binding compounds) was detected by a solid medium [23]. It is a universal assay for the recognition and determination of siderophores. To prepare the Iron (III solution, dissolve 1 mM $FeCl_3 \cdot 6H_2O$ in 10 mM HCl. For the 10 MM9 salts,mix 3 g of KH_2PO_4,
0.5 g of NaCl, and 10 g of NH_4Clin 1 L of water,and autoclave to sterilize. For the Fe-CAS-HDTMA solution, dissolve 605 mg of CAS in 500 mL of water in a glass bottle
1L while stirring, then 100 mL of the Iron (III) solution was added. After that, 729 mg of HDTMA was slowly incorporated in 400 mL of water, and stirred till dissolved. autoclave, and cooledto 50°C. To prepare CAS agar plates,in a 2 L flask,dissolve 6 g of NaOH in 750 mL of water,then add 30.24g of PIPES (free acid) and 100 mL of the 10 MM9 salts, followed by 15 g of Bacto agar.After autoclaving this mixture, cool it to 50°C. Next, whilestirring, add 30 mL of 10% casaminoacids, 10 mL of 20% glucose, 1 mL of 1 M $MgCl_2$, 1 mL of 100 mM $CaCl_2$, 1 mL of 1% nicotinic acid, and 1 mL of 1 M $MgSO_4 \cdot 7H_2O$ to the cooled solution. Carefully add 100 mL of the Fe-CAS-HDTMA solution along the flask'swall to avoidbubbles. Pour approximately 20 mL of the blue agar into sterile Petri dishes and allow the agar to solidify overnight at room temperature, then inoculate in the plate center with a 0.5 cm disc of tested fungal culture. The CAS reactionrate was detectedby measuring the change of CAS blue agar color intensity. The control platesof CAS-agar were uninoculated and incubated under the same conditions of CAS, and no color change results were recorded after long incubation periods (10-15 days).

Fungal Zinc Solubilization Assay

The main indicator of fungal Zinc Oxide solubilizing ability was the diameter of the agar's solubilization area (clear halo). The used medium was composed of. 10.0 g Dextrose, 1.0 g Ammonium sulfate, 0.2 g Potassium chloride, 0.1 g Dipotassium hydrogenphosphate, 0.2 g Magnesium sulfate,1.0 g Zinc oxide, 15.0 g agar, and 1000 mLdistilled water[24]. The six fungal species tested were inoculated on these

media for 144h and incubated at 28 ° C. Zinc Solubilization Efficiency (ZSE) was computed following this equation[25].

ZSE = Diameter of solubilization halo zone / Diameter of colony *100

Fungal species were cultivated in a broth medium containing the same previous ingredients except agar. pH measurements were made at intervals of 2, 4, and 6 days, in triplicate, pH measurement using an electrode (Milwaukee MW150 MAX).

Fungal Phosphate Solubilization Assay

Six isolated fungal species were screened for their potential to solubilize Tricalcium Phosphate(TCP) as insoluble inorganic phosphate sources on medium. A clear halo zone around the fungal colonyis an indicator of phosphate-solubilizing capacity.

Pikovskaya (PVK) medium contained: glucose, 10 g; Ca3(PO4)2, 5 g; (NH4)2SO4, 0.5 g; NaCl, 0.2 g; MgSO4.7H2O, 0.1 g; KCl, 0.2 g; yeast extract,0.5 g; MnSO4.H2O, 0.002 g; and FeSO4.7H2O, 0.002 g. [26]. Sterilized PVK medium was poured into sterilized 90mm Petri dishes, allowing them to solidify. In the center of each plate, 5 mm discs of tested fungal species were inoculated with three replicates and then incubated at 28°C. The colony diameterand clear zone distancearound each colony were measured after 3, 5, and 7 days. The Phosphate Solubilization Index (PSI) was recorded on each measurement day and calculated [27].

PSI = Colony diameter + Halo zone diameter / Colony diameter

RESULTS

Fungal diversity and abundance at Quba farm

Isolated fungi shown inTable 1 were 21 species (60250 CFU) belonging to 11 genera from the various sources under investigation: soil, water, and plant leaves. from Quba farm soil the abundance of the genus Aspergillus was represented by several speciesthe highest frequency was A. niger, followed by Trichoderma longibrachiatum, while A. fumigatiaffinis was rare as shown in Table 1. Molecular identification of A. fumigatiaffinis based on the 18S rDNA gene sequences, it's clear that MKSA3 fungal strain isolated from soil had 100% identities to the A. fumigatiaffinis sequence stored in the GenBank database. A phylogenetic tree utilizing the Neighbor-joining methodin MEGAX displayed cleargrouping and a high degreeof homology for A. fumigatiaffinis MKSA3 with related available species data in the NCBI database (Fig. 2). The gene sequence was deposited in GenBank under accession number PQ433223.

Table 1. Total count and distribution of fungal generacollected from Quba farm.

Isolation source	Total count	Number of genera	Number of species	Identified species	Frequency class
Soil	50000	5	12	*Aspergillus niger*	H
				A.flavus	H
				A. terreus	M
				A.ochraceus	L
				A. ustus	M
				A. fumigatiaffinis	R
				Trichoderma	M
				longibrachiatum	M
				Trichoderma sp.	L
				Fusarium	H
				oxysporum	L
				Penicillium oxalicum	M
				P.chrysogenum	
				Emericella nidulans	
Water	10000	4	7	*Fusarium sp.*	M
				Alternaria Alternata	H
				Cladosporium sp.	H
				Penicillium oxalicum	L
Plant phyllosphere	250	1	2	*Aspergillus niger*	H
				A.flavus	H

H= high M= moderate L= low R= rare

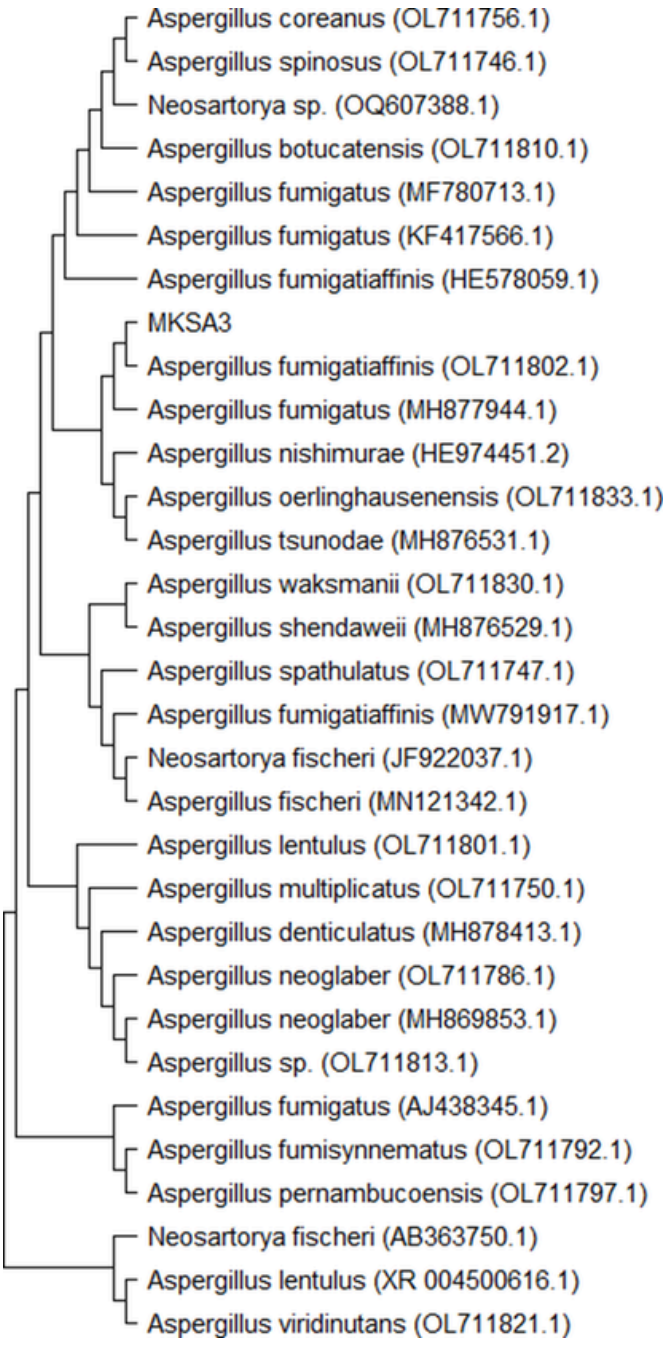

Figure 2. Phylogenetic relationship between Aspergillus isolate MKSA3 and the matching Aspergillus species(including the corresponding species from NCBI, signaled with GenBank accession number at the tip of each branch).

Physiological characterization of fungal species

The physiological assay of isolated fungi shown in Table 2 represents the activity of urease-producing fungi. A. fumigatiaffinis MKSA3 showed a pink color at Christensen's Urea Agar after 4 days of incubation at 28° C. In addition, T. longibrachiatum showed a similar pink color due to the activity of fungal ureases that liberate ammonia from the urea. The CAS assay, a colorimetric assay to measure the Fe- chelating function of siderophores followed in this study to screen isolated fungal species. Results showed that only two species, A. fumigatiaffinis MKSA3 and P. oxalicum produce siderophores based on a change of blue color to orange around the colony.

Table 2. Screening abilityof fungal speciesisolated from Quba farm to produce urease and siderophore.

Fungal species	Urease activity	Siderophore Production
Aspergillus niger	++	-
A. fumigatiaffinis	+++	+
A.flavus	++	-
A. terreus	++	-
A.ochraceus	-	-
Trichoderma longibrachiatum	+++	-
Trichoderma sp.	++	-
Penicillium oxalicum	++	+
P. chrysogenum	-	-
Emericella nidulans	+++	-
Alternaria alternata	-	-
Fusarium oxysporum	+	-
Cladosporium sp.	-	-

Potentiality of Fungal Zinc and Phosphate Solubilization

Fungal species from Quba farm soil namely, A. ustus, A. niger. A. fumigatiaffinis MKSA3, and P. oxalicum. solubilized and transformed insoluble zinc oxide compounds (ZnO) into a soluble form. The comparison between six fungal species in zinc solubilization efficiency (ZSE) showed that A. fumigatiaffinis MKSA3 recorded an efficiency of 216% followed by A. flavus (178%) as shown in Fig (3). The promising strain A. fumigatiaffinis MKSA3 showed efficiency for solubilizing insoluble zinc compounds, producing clearing zone diameters that reached up to 60 mm after six days ofincubation (Fig. 4). The solubilization efficiency of testedspecies combined with its acid production ability.The result observedwas that the

fungal speciesthat showed the greatest zone of solubilization in solid medium, similar zinc oxide solubilization in liquid medium was also observed. The pH of the broth medium inoculated by A. fumigatiaffinis MKSA3 has decreased from 7.0 to 3.05 as mentioned in Table 3.

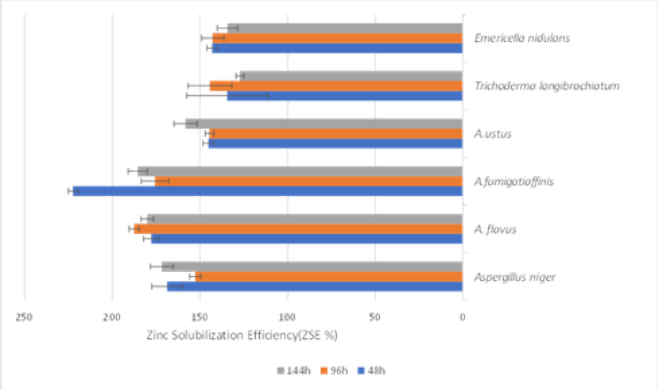

Figure 3. Efficiency of different fungalspecies on Zinc oxide solubilization after 48h.
(A) 96h (B) and 144h (C).

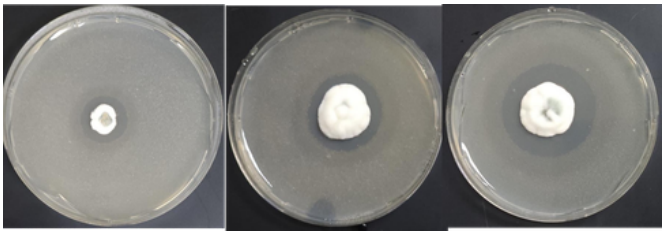

Figure 4. Efficiency of A. fumigatiaffinis MKSA3 (PQ433223) on Zinc oxide solubilization after 48h. (A) 96h (B) and 144h (C).

Table 3. pH changesin the liquid medium.

Fungal species	2nd day pH	4th day pH	6th day pH
Aspergillus niger	5.8	4.6	4
A. fumigatiaffinis	5.1	4.2	3.05
A.flavus	4.9	4	3.8
A.ustus	6	5.7	5.1
Trichoderma longibrachiatum	6.2	5.9	5.3
Emericella nidulans	5.8	4.7	4.2

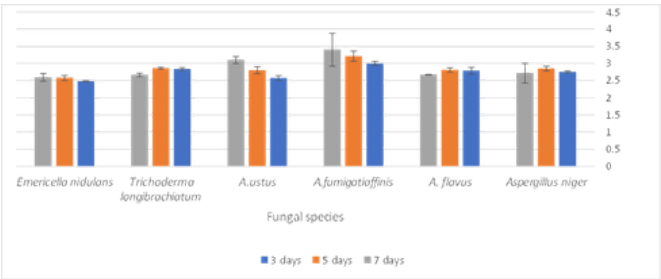

Figure 5. Efficiency of different fungalspecies on TCP solubilization after3, 5, and 7 days.

The screened fungi were competent to solubilize TCP on PVK solid medium by forming clear halozone differing according to the degree of solubilization. As shown in Fig. 5 the highest PSI was A. fumigatiaffinis MKSA3 reached 3.4 after 7 days of incubation followed by A. ustus and A. niger, while Emericella nidulans was weak phosphate solubilizers as clear in Fig.6.

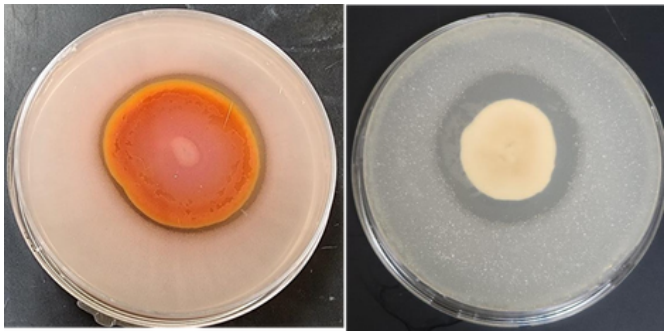

Figure 6. Solubilization of TCP indicated by halo zone around coloniesof two fungal species (A, Emericella nidulans and B, A. fumigatiaffinis MKSA3) on solid PVK medium after 7 days of incubation.

DISCUSSION

The core goal of the present study was to study mycobiotaon an organic farm near the Quba region in Madinah, Saudi Arabia. The survey of fungal species was determined to test their potential in the solubilization of minerals. A total of 21 species have been recorded, and the genus Aspergillus was the richestby showing a spectrum of 7 species; it comes next by Penicillium and Fusarium. These results agree with some mycobiota detected in regionssuch as the Sabkha and desert areasin Saudi Arabia[28-29]. However, the previous studies identified fungal diversity, but soil microbial diversity in the Madinah region was not sufficiently covered. In addition, the physiological characterization of isolated fungalspecies to select a promisingcandidate(s) that could be used in biomineralization. From the rhizosphere soil of Quba farm, one promising strain was identified as A.

fumigatiaffinis MKSA3; its gene sequencewas deposited in GenBank under accession numberPQ433223. This strain has not been recordedbefore in Saudi Arabian soil mycobiota. Siderophore production by fungi is a known method for increasing the availability of Iron for plants [30]. Several fungal species were previously recorded to produce siderophores, such as A. niger[31]. Trichoderma harzianum[32], and Penicillium sp.[29]. In thisstudy, only two species, A. fumigatiaffinis MKSA3 and P. oxalicum,out of twenty- one species, produce siderophores. This observation agrees with other investigators[33,34].

Urease production by fungi is another mechanism to enhance plant growth. Examples of fungal species previously recorded as urease producers are Chaetomium globosum, Aspergillus fumigatus, and A. nidulans [35]. Results for the current survey indicated that most of the tested fungalisolates showed a change in Christensen's Urea Agarto a pink color after 4 days of incubation due to the liberation of ammonia. The solubilization of minerals like Phosphate and Zinc is a common mechanism adoptedby fungi to increase plant growth through the increased availability of some insoluble minerals[36].

Surveys of zinc-solubilizing fungi in Saudi Arabia were not fully studied, especially in the Madina region.Fungal species from Quba farm soil namely, A. ustus, A. niger.
A. fumigatiaffinis MKSA3, and P. oxalicum. showed great efficiency in zinc solubilizing. Similar results were recorded in an entomopathogenic fungus, Metarhiziumpingshaense[37]. The highest zinc solubilization efficiency was
detected by the width of the clearing zone diameters around the colony as observed in A. fumigatiaffinis MKSA3 and A. flavus.

Phosphate solubilization makes it accessible to plants, improving the growth and productivity of wide types of crops [38,39]. This study revealedthat the highestphosphate solubilization produced by A. fumigatiaffinis MKSA3 reached 3.4 SI after 7 days of incubation followed by A. ustus and A. niger, while Emericella nidulans was weak phosphate solubilizers. Some investigators found similar results [40]. The activity of A.fumigatiaffinis MKSA3 as a phosphate solubilizer could be attributed to high acid production. The acidity increased and wasdetected by a decreaseof broth mediumpH to 3.05 after 7 days of incubation, results matching the other investigator's findings[41].

CONCLUSION

According to the results obtainedin the present study, it was a promising new recorded fungal species identified as A. fumigatiaffinis strain MKSA3, that showed great potential to solubilize minerals such as urea, zinc and phosphate in addition to siderophore production. This species can be used as biofertilizers after completing other studies such as plant pots experiments and safety assay.

REFERENCES

1- Jacoby R, Peukert M, Succurro A, Koprivova A, Kopriva S. The Roleof Soil Microorganisms in Plant Mineral Nutrition-Current Knowledge and Future Directions. Front. Plant Sci.2017; 8:1617.
doi.org/10.3389/fpls.2017.01617

2- Syamsia S, Idhan,A, Firmansyah AP, Noerfitryani, N, Rahim I, Kesaulya H, Armus R. Combination on endophytic fungal as the Plant Growth-Promoting Fungi (PGPF) on cucumber (Cucumis sativus). Biodiversitas.2021;22(3), 1194–1202.

3- Malgioglio, G, Rizzo,GF, Nigro, S, Lefebvre Du Prey, V, Herforth-Rahmé, J,

Catara, V, Branca, F. Plant-Microbe Interaction in Sustainable Agriculture: The Factors That May Influence the Efficacy of PGPM Application. Sustainability 2022; 14; 2253.doi.org/10.3390/su14042253

4- El-Maraghy SS, Tohamy AT,Hussein KA.Plant protection properties of the Plant GrowthPromoting Fungi (PGPF):Mechanisms and potentiality. Current Research in Environmental &Applied Mycology (Journal of Fungal Biology) 2021; 11(1), 391–415, doi 10.5943/cream/11/1/29

5- Runnel K, Tedersoo L, Krah FS,Piepenbring M, Scheepens JF, Hollert H, Johann S, Meyer N, Bässler C. Toward harnessing biodiversity–ecosystem function relationships in fungi. Trends in Ecology & Evolution.2025; 40 (2), 180-190. doi.org/10.1016/j.tree.2024.10.004

6- AjijahN, Fiodor A, Pandey AK, Rana A, Pranaw K. Plant growth-promoting bacteria (PGPB) with biofilm-forming ability: a multifaceted agentfor sustainable agriculture. Diversity.2023; 15(1),112. doi 10.3390/d:15010112

7- Abdelaziz AM, HashemAH, El-Sayyad, GS, El-Wakil, D A, SelimS, Alkhalifah, D H, Attia,MS. Biocontrol of soil-borne diseases by plantgrowth promoting rhizobacteria. Tropical Plant Pathology. 2023; 48(2), 105-127. doi 10.1007/s40858-022-00544-7

8- Ahirwar, NK, SinghR, Chaurasia S, Chandra R, Ramana S. Effective role of beneficial microbes in achieving the sustainable agriculture and eco-friendly environment development goals: A review. Frontiers in Environmental Microbiology.2019; 5(6), 111-123.doi:10.3389/fmicb.2020.01551

9- Al-Falih AM. Phosphate Solubilization in vitroby some soil yeasts. QatarUniv. Sci. J. 2005; 25:ll9-12

10- Ahmed E, HOLMSTRÖM SJM. Siderophores in environmental research: roles and applications. Microbial biotechnology, 2014, 7(3)196-208.doi.org/10.1111/1751-7915.12117

11- Ashok A, Doriya K, Rao JV, Qureshi A, Tiwari AK, Kumar DS. Microbes Producing L-Asparaginase free of Glutaminase and Urease isolated from Extreme Locations of Antarctic Soiland Moss. Sci Rep.2019;9(1):1423. doi: 10.1038/s41598-018-38094-1.

12- Jain P, SinghD. Study on the roleof phosphate solubilizing fungi in phosphorus bioavailability and growth enhancement of potato.Chemical Science Review and Letters.2015; 4 (13): 101-108.

13-Jamal A, Ayub N, Usman M, Khan, AG. Arbuscular mycorrhizal fungi enhance zinc and nickeluptake from contaminated soil by soybean and lentil. International Journal of Phytoremediation. 2002; 4(3),205 - 221. doi:10.1080/15226510208500083

14- Van EerdL, Congreves KA, Hayes A, Verhallen A, Hooker DC. Long-term tillageand crop rotation effects on soil quality, organic carbon, and total nitrogen. Canadian Journal of Soil Science. 2014; 94(3): 303-315. as Pseudomonas, Burkholderia, and Rhodococcus exhibit enhanced expression of catabolic genes, leading to 5–10-fold higher degradation rates of polycyclic aromatic hydrocarbons (PAHs) and polychlorinated biphenyls (PCBs) compared with bulk soil [28].

Agronomic plants including maize and ryegrass have demonstrated substantial enhancement of pesticide degradation; atrazine removal efficiencies of up to 85% within 30 days have been reported in rhizosphere-enriched soils. Advances in engineered microbial consortia, including genetically modified rhizobia and synthetic microbial communities, further enhance rhizoremediation specificity and resilience

under climate stress conditions such as drought and temperature fluctuations [20].
15- Samson,RA, Pitt, JI. (eds.). Advances in Penicillium andAspergillus systematics. NewYork and London.1985
16- Johnson, LF, Curl EA, Bond JH, Fri, BourgHA. Method for studying soilmicroflora – plant disease relationship. BurgessPublishing Co., Minneapolis, USA.1960
17- RaperKB, Fennell DI.The genus Aspergillus. Williams and Wilkins, company Baltimore, Maryland. 1965; 686p.
18- Domsch, KH, Gams W, Anderson TH. Compendium of Soil Fungi.Vol. 1-2, Academic Press, London.1980.
19- Christensen M, Raper KB. Synoptic keyto Aspergillus nidulans group species and related Emericella species. Transactions of the BritishMycological Society.1978; 71(2). 177-191.doi.org/10.1016/S0007-1536(78)80097-7
20- PittJI. The genusPenicillium and its teleomorphic statesEupenicillium and Talaromyces. London New York: Academic Press.1979; 634P
21- MartinKJ, Rygiewicz PT.Fungal-specific PCR primers developed for analysis of the ITS region of environmental DNA extracts. BMC Microbiol. 2005; 18(5):28. doi: 10.1186/1471-2180-5-28
22- Phang IRK, San Chan Y, Wong KS, Lau SY. Isolation and characterization of urease-producing

bacteria from tropical peat. Biocatalysis and agricultural biotechnology. 2018; 13: 168 175.as Pseudomonas, Burkholderia, and Rhodococcus exhibit enhanced expression of catabolic genes, leading to 5–10-fold higher degradation rates of polycyclic aromatic hydrocarbons (PAHs) and polychlorinated biphenyls (PCBs) compared with bulk soil [28].
Agronomic plants including maize and ryegrass have demonstrated substantial enhancement of pesticide degradation; atrazine removal efficiencies of up to 85% within 30 days have been reported in rhizosphere-enriched soils. Advances in engineered microbial consortia, including genetically modified rhizobia and synthetic microbial communities, further enhance rhizoremediation specificity and resilience under climate stress conditions such as drought and temperature fluctuations [20].
23- LoudenBC, Haarmann D, Lynne AM. Use of blue agar CAS assayfor siderophore detection. Journal of Microbiology & Biology Education.2011; 12(1): 51-53.doi: 10.1128/jmbe.v12i1.249
24- Devi D, GuptaSB, Mishra BK, Verma NP. Isolation and identification of zinc solubilizing fungal isolates fromcumin of semi-arid region of Rajasthan. Pharma Innov J.2022; 11(2),1036-1040.
25- RameshA, Sharma SK, Sharma MP,Yadav N, JoshiOP. Inoculation of zinc solubilizing Bacillus aryabhattai strains for improved growth, mobilization, and biofortification of zinc in soybean and wheat cultivated in Vertisols of central India. Applied Soci. Ecology.2014; 73:87-96.
as Pseudomonas, Burkholderia, and Rhodococcus exhibit enhanced expression of catabolic genes, leading to 5–10-fold higher degradation rates of polycyclic aromatic hydrocarbons (PAHs) and polychlorinated biphenyls (PCBs) compared with bulk soil [28].
Agronomic plants including maize and ryegrass have demonstrated substantial enhancement of pesticide degradation; atrazine removal efficiencies of up to 85% within 30 days have been reported in rhizosphere-enriched soils. Advances in engineered microbial consortia, including

genetically modified rhizobia and synthetic microbial communities, further enhance rhizoremediation specificity and resilience under climate stress conditions such as drought and temperature fluctuations [20].
26- Nautiyal, C. S. An efficient microbiological growth medium for screening phosphate solubilizing microorganisms. FEMS Microbiology Letters. 1999; 170(1), 265-270.doi.org/10.1111/j.1574-6968.1999.tb13383.x
27- Edi-Premono M, Moawad AM, Vleck, PLG.Effect of phosphate solubilizing Pseudomonas
putida on thegrowth of maizeand its survival in the rhizosphere. Indonesian Journal of Crop Science. 1996; 11(1),13-23
28- AmeenF, AlNAdhari S, Yassin MA, Al-Sabri A, Almansob A, Alqahtani N, Stephenson SL. Desert
soil fungiisolated from SaudiArabia: Cultivable fungalcommunity and biochemical production. Saudi Journal of Biological Sciences.2022; 29(4), 2409-2420.doi.org/10.1016/j.sjbs.2021.12.011
29- Johnson L. Iron and siderophores in fungal–host interactions. Mycological research.2008;112 (2),
170-183.doi: 10.1016/j.mycres.2007.11.012
30- JyothiV, Sowmya HV, Thippeswamy B. Siderophore production by phosphate solubilizing fungi
from rhizospheric soil of medicinal plants. Int. J. Biol.Biotechnol. 2020; 17(3).599-606.
31- Alwadai, AS,Al Wahibi, M.S,Alsayed, MF, Alshaikh, NA, Perveen K, Elsayim, R.

Authors

Dr. Metwally R. Kottb is an Assistant Professor in the Department of Biology at Taibah University, Medina, Saudi Arabia. He holds a PhD and a Master's degree in Microbiology from Suez Canal University. His research focuses on: Taxonomic classification of fungi and their biological resistance capabilities, Investigating fungi as biological control agents against plant diseases.

Shaher Aljohny is a Biology student with professional experience in the healthcare sector. His academic interests focus on the integration of biological sciences with clinical applications, particularly in genetics, public health, biotechnology, and laboratory-based research.

Sultan K. Bakhsh is a licensed Biology graduate from Taibah University in Saudi Arabia. He is currently pursuing a master's degree in Environmental Science at King Abdulaziz University in Saudi Arabia. His expertise includes serving as a research assistant in microbiology. Additionally, Sultan has experience in laboratory management and data analysis, contributing significantly to various research initiatives.

Solvent-Assisted Quantitative X-Ray Diffraction Analysis of Crystalline Phases in Oil-Based Refinery and Gas Plants Sludge Deposits*

Mona S. Al-Dossary*, Husin Sitepu**
Research and Analytical ServicesDepartment, Saudi Aramco, Saudi Arabia.
*Correspondence: mona.dossary.2@aramco.com
**Retired from SaudiAramco after more than 16 years of service in cutting-edge research.

Abstract

Oil-based sludge deposits formed within refinery and gas-processing systems present persistent challenges to asset integrity and operational reliability due to their heterogeneous composition and complex multiphase nature. Accurate identification and quantification of the crystalline inorganic constituents are critical for understanding corrosion, scaling, and fouling mechanisms. However, conventional X-ray diffraction (XRD) analysis is frequently compromised by residual hydrocarbons, elevated amorphous background signals, and limited availability of crystalline material.

In this study, a solvent-assisted sample preparation protocol is developed and validated to enable reliable quantitative crystallographic analysis of oil-based sludge deposits using high-resolution XRD coupled with full-pattern Rietveld refinement. The methodology selectively concentrates the crystalline fraction, significantly reducing hydrocarbon-related background interference and minimizing preferred orientation effects. The approach is applied to sludge samples collected from a refinery natural gas line and demonstrates robust phase identification and quantification using as little as ~0.5 g of crystalline material.

The identified phase assemblage comprises iron oxides, iron oxyhydroxides, iron sulfides, carbonates, and minor silicate phases, reflecting the combined influence of oxidative corrosion, sulfide-induced degradation, water chemistry– controlled scaling, and external particulate ingress. These results demonstrate that effective sample preparation, rather than sample mass, is the primary factor governing XRD data quality and quantitative reliability.

The proposed solvent-assisted methodology offers a reproducible, industry-relevant framework for deposit characterization and provides actionable insights to support mitigation strategies and asset integrity management in refinery and gas-processing operations.

Keywords: Oil-based sludge; quantitative XRD; Rietveld refinement; refinery deposits; corrosion diagnostics; phase analysis.

Acknowledgment

The accumulation of oil-based sludge remains a significant operational challenge in refinery and gas-processing facilities, where deposits adversely affect process efficiency, restrict fluid flow, and promote localized corrosion that may ultimately

result in unplanned shutdowns. These deposits are inherently heterogeneous, comprising viscous hydrocarbon matrices that encapsulate fine inorganic constituents such as corrosion products, scale-forming minerals, catalyst residues, and externally introduced particulates. The stability, adhesion, and removability of such deposits are strongly influenced by the identity, abundance, and distribution of their crystalline phases. Conventional bulk chemical and elemental analyses provide useful averaged compositional information but offer limited insight into crystalline phase assemblages and phase-specific abundances, which are essential for understanding deposit formation mechanisms and predicting mitigation behavior. X-ray powder diffraction (XRD), combined with quantitative phase analysis using Rietveld refinement, provides direct crystallographic information that is critical for mechanistic interpretation of industrial deposits. In oil-based sludge systems, however, XRD analysis is often compromised by dominant amorphous backgrounds arising from residual hydrocarbons, limited crystalline material, and preferred orientation effects, all of which reduce phase detectability and quantitative reliability.

Recent studies have demonstrated that, for hydrocarbon-rich industrial deposits, the reliability of crystallographic characterization is governed primarily by the effectiveness of sample preparation rather than by instrumental resolution alone [1–5].

Selective removal of the organic matrix is therefore essential to isolate the crystalline inorganic fraction and enable meaningful diffraction analysis. Building on advances in quantitative crystallography applied to refinery and gas-processing deposits [1–10], the present work introduces a solvent-assisted sample preparation methodology specifically designed to enhance crystalline phase recovery while minimizing analytical artifacts.

The proposed methodology is evaluated using sludge deposits collected from a refinery natural gas line, with particular emphasis on analytical performance under material-limited conditions commonly encountered during field investigations [1]. By enabling reliable phase identification and quantitative analysis from small quantities of crystalline material, this study extends the practical applicability of quantitative XRD for diagnosing fouling, scaling, and corrosion phenomena in hydrocarbon-processing environments.

Objectives

The objectives of this study are to:

1. Develop and establish a reproducible solvent-assisted protocol for isolating crystalline inorganic phases from oil-based sludge deposits.
2. Generate high-quality XRD data characterized by low background intensity and controlled preferred orientation effects.
3. Perform robust phase identification and quantitative phase analysis using full-pattern Rietveld refinement.
4. Demonstrate analytical reliability when applied to limited quantities of crystalline material (approximately 0.5 g).
    a. Translate crystallographic findings into actionable insights relevant to corrosion, scaling, and fouling control in refinery and gas-processing systems.

Experimental Work

A.Deposit Sampling

Oil-based sludge deposits were collected

from affected sections of a refinery natural gas line during scheduled maintenance activities **(Figure 1).** The recovered materials exhibited pronounced heterogeneity, consisting of a semi-solid hydrocarbon matrix containing finely dispersed inorganic particulates derived from corrosion reactions, interactions with aqueous phases, and upstream solids ingress.

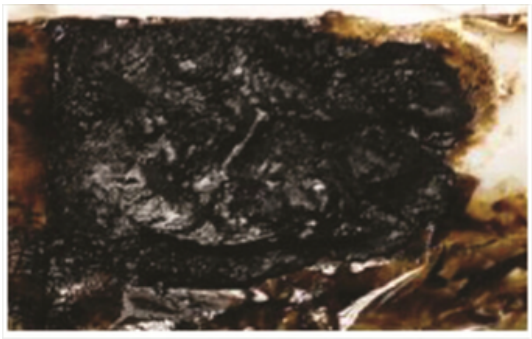

Figure 1. Schematic representation of oil-based sludge deposits collected from refinery natural gas line equipment, illustrating the heterogeneous association between hydrocarbons and entrapped inorganic particulates

B. Solvent-Assisted Sample Preparation

To isolate the crystalline inorganic fraction, sludge samples were treated with dichloromethane to selectively dissolve the hydrocarbon matrix. The mixtures were mechanically agitated to promote efficient extraction, followed by filtration to separate solvent-soluble organic components from the insoluble residue **(Figure 2).** Detailed procedural considerations are described by Sitepu et al. [1] and the references therein.

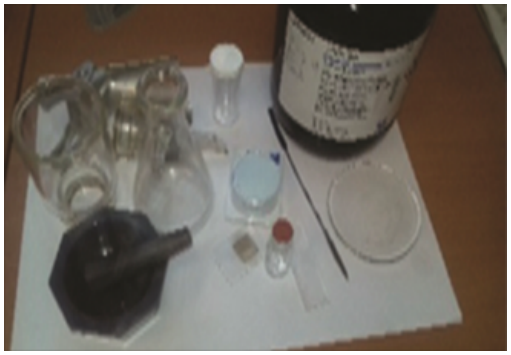

Figure 2. Schematic workflow of the solvent-assisted sample preparation procedure, highlighting selective hydrocarbon dissolution by dichloromethane and recovery of the crystalline inorganic residue for XRD analysis.

The recovered solid fraction (Figure 3) was dried under controlled conditions and gently ground using an agate mortar and pestle to produce a fine, homogeneous powder suitable for diffraction analysis.

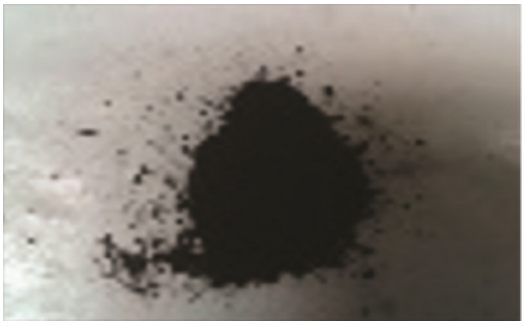

Figure 3. Dichloromethane-insoluble crystalline fraction isolated from oil-based sludge deposits, representing the target material for qualitative and quantitative XRD investigation.

Powder mounting was performed using side-drifting and back-loading techniques to minimize preferred orientation effects and to ensure representative sampling of crystallite orientations [10–12].

C. X-Ray Diffraction Data Collection and Analysis

XRD measurements were conducted using a Rigaku ULTIMA-IV diffractometer equipped with Cu Kα radiation. Diffraction data were collected over a 2θ range of 4–75° using step-scan acquisition parameters optimized for multiphase materials. Phase identification was carried out using HighScore Plus software in conjunction with the ICDD PDF-4+ database.

Quantitative phase analysis was performed using full-pattern Rietveld refinement [1,10–15]. The refinement strategy incorporated background modeling, appropriate peak-shape functions, and corrections for preferred orientation based on established crystallographic methodologies [1–3,10–15].

Results and Discussion

A. Analysis of Crystalline Fractions from Bulk Samples (>1.0 g)

X-ray diffraction patterns obtained from bulk crystalline residues exceeding 1.0 g exhibited sharp, well-resolved reflections accompanied by a consistently low background signal. This confirms the effective removal of residual hydrocarbons during solvent-assisted sample preparation and indicates that the recovered material was well suited for crystallographic analysis. The identified crystalline phases include siderite ($FeCO_3$), magnetite (Fe_3O_4), goethite [FeO(OH)], calcite ($CaCO_3$), dolomite [$CaMg(CO_3)_2$], quartz (SiO_2), and calcium chloride hydroxide hydrate [$CaCl_2{\cdot}Ca(OH)_2{\cdot}H_2O$], as shown in **Figure 4.** The high quality of the diffraction data enabled unambiguous phase identification and reliable quantitative refinement.

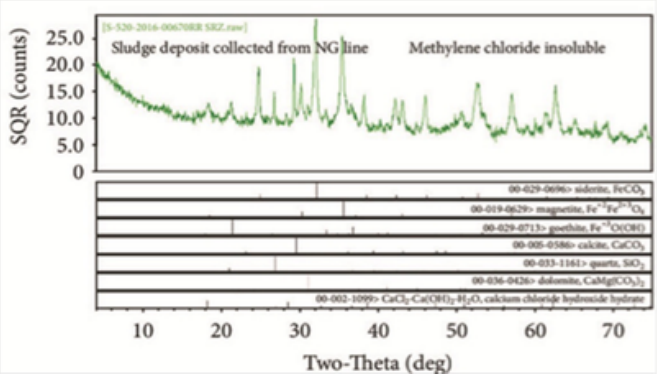

Figure 4. X-ray diffraction pattern of bulk crystalline deposits (>1.0 g), showing iron corrosion products, carbonate scale phases, silicates, and chloride-bearing compounds identified through phase matching with the ICDD PDF-4+ database.

The coexistence of iron carbonates, oxides, and oxyhydroxides reflects the operation of multiple, overlapping deposit formation mechanisms within the refinery natural gas system. The presence of siderite is indicative of CO_2-related corrosion under reducing conditions, whereas magnetite and goethite suggest subsequent oxidation processes driven by oxygen ingress or fluctuations in redox potential. Carbonate phases such as calcite and dolomite point to water chemistry–controlled scaling processes, while chloride-bearing hydrated phases indicate localized chloride enrichment that can enhance corrosivity. The detection of quartz further suggests contributions from externally introduced particulates or upstream process contamination.

Such complex multiphase assemblages are consistent with observations reported in recent quantitative crystallographic studies of refinery and gas-processing deposits [3–5,7–9]. Importantly, these results demonstrate that the refined solvent-assisted preparation protocol enables effective phase discrimination in chemically and structurally complex industrial materials, directly supporting Objectives 1–3 of this study.

B. Analysis of Crystalline Fractions from Limited Samples (~0.5 g)

A key objective of this work was to assess the robustness of the proposed methodology under material-limited conditions typical of field investigations. Despite a reduced crystalline sample mass of approximately 0.5 g, the prepared residues produced diffraction patterns of sufficient quality for confident phase identification and quantitative analysis. As shown in Figure 5 and summarized in Table 1, the deposits were dominated by iron oxides and oxyhydroxides, accounting for approximately 82 wt%, followed by iron sulfide phases (~17 wt%) and minor quantities of quartz.

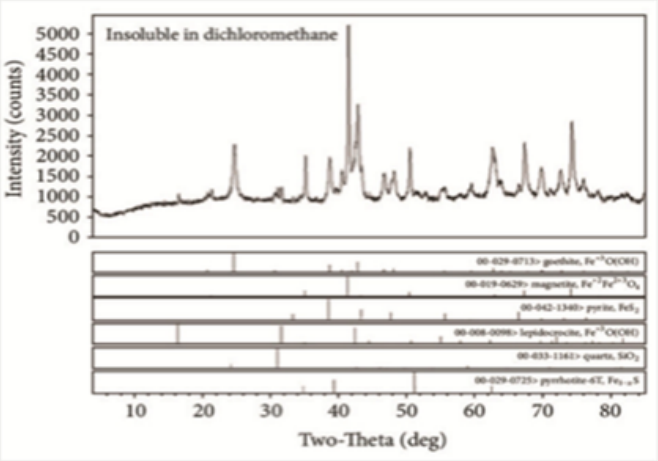

Figure 5. XRD pattern and corresponding Rietveld refinement of approximately 0.5 g of crystalline residue, demonstrating reliable phase identification and quantitative analysis under limited sample mass conditions.

Table 1. Quantitative phase analysis results (wt%) obtained from Rietveld refinement.

Detected Compound	wt%
Iron oxides and oxyhydroxides (total)	**81.84**
— Goethite	56.45
— Magnetite	14.64
— Lepidocrocite	10.75
Iron sulfides (total)	**16.53**
— Pyrite	15.28
— Pyrrhotite	1.25
Quartz	**1.63**
Total	**100.00**

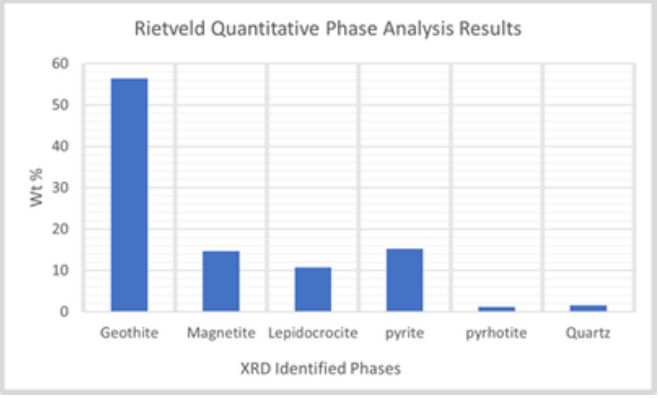

Figure 6. Relationship between phases identified by XRD (horizontal axis) and their corresponding quantitative phase abundances (wt%; see Table 1), shown on the left vertical axis.

The predominance of iron oxide and oxyhydroxide phases indicates sustained oxidative corrosion processes within the system. In contrast, the presence of iron sulfides—specifically pyrite and pyrrhotite—points to sulfide-driven corrosion pathways associated with reduced sulfur species. These phases may also reflect the influence of microbiologically influenced corrosion (MIC), particularly under stagnant or low-flow conditions. The observed phase assemblage is consistent with integrated corrosion studies that combine crystallographic, chemical, and microbiological evidence in refinery environments [5,6].

Critically, these findings confirm that the quality of sample preparation, rather than absolute sample mass, is the primary factor controlling the success of XRD-based phase characterization in oil-based sludge systems. This directly fulfills Objective 4 and demonstrates that reliable quantitative crystallography can be achieved even under the practical constraints of outage-related or field-limited sampling.

C. Engineering and Operational Implications

The ability to quantitatively distinguish between oxide-, carbonate-, and sulfide-dominated deposits has direct and practical implications for refinery and gas-plant operations. Oxide-rich deposits may require oxidative or chelation-based cleaning strategies, whereas carbonate scaling is more effectively mitigated through water chemistry control or scale inhibition programs. In contrast, sulfide-bearing deposits often necessitate targeted biocide application and enhanced monitoring for MIC.

By enabling rapid, evidence-based identification of deposit composition, the proposed methodology supports informed decision-making during maintenance planning, failure investigations, and

corrosion mitigation initiatives. This directly aligns with Objective 5 and reinforces the value of quantitative crystallography as a diagnostic tool for improving asset integrity, operational reliability, and lifecycle management in hydrocarbon-processing facilities.

Limitations and Future Work

The present methodology is limited to characterization of the crystalline inorganic fraction; amorphous phases and organic components are not directly quantified. Future studies should integrate XRD with complementary analytical techniques such as XRF, SEM–EDS, and thermal analysis to achieve a more comprehensive characterization of sludge deposits. Additionally, extension of this approach to time-resolved or condition-dependent studies may provide further insight into deposit formation and evolution under varying operational environments.

Conclusions

A solvent-assisted XRD methodology combined with full-pattern Rietveld refinement has been successfully established for the reliable characterization of crystalline phases in oil-based refinery and gas plant sludge deposits. The approach effectively overcomes analytical challenges associated with hydrocarbon-rich matrices and enables accurate phase identification and quantification even when only limited crystalline material is available. This methodology represents a practical and reproducible diagnostic tool for elucidating deposit formation mechanisms and supports informed decision-making for mitigation strategies and asset integrity management in refinery and gas-processing systems.

Acknowledgments

The authors gratefully acknowledge the management of Saudi Aramco for granting permission to publish this work. Sincere appreciation is extended to the professionals and technicians of the Research and Analytical Services Department (RASD) and R&DC for their technical support throughout this study. The authors are indebted to the anonymous reviewers and to Dr. Shakeel Ahmad, Editor-in-Chief of the Journal of CRIS, for their constructive comments, which greatly improved the qualityof the manuscript. *An earlierversion of this work was presented at the First Gulf Chemistry Association International Conference and Exhibition (GCA-2022), Gulf International Hotel, Kingdom of Bahrain, 15–17 November 2022.

References

1-H. Sitepu, N.M. Al-Yami, I.M. Al-Zahrani, Texture effects and quantitative Rietveld analysis of crystalline deposits for failure investigation applications Powder Diffraction 40(1) (2025) 7–20.

2-H. Sitepu, B.H. O'Connor, Obituary: Brian H. O'Connor (1940–2024). J. Appl. Crystallogr. 58 (2025) 1511–1512.

3- H. Sitepu, R.A. Al-Ghamdi, M.S. Al-Dossary, H.S. Khanfar, Quantitative phase analysis of crystalline deposits from refinery and gas-processing equipment using XRD. J. Chem. Res. Innov. Soc. 2(3) (2025) 11–20.

4-M. Nagu, H. Sitepu, W.A. Algozeeb, N.M. Alanazi, Quantitative XRD-based root cause analysis of filter sludge deposits in refinery systems. J. Chem. Res. Innov. Soc. 2(1) (2025) 33–46.

5-H.S. Khanfar, H. Sitepu, N.S. Alshihri, M.S. Al-Dossary, X. Zhu, I.M. Al-Zahrani, Integrated assessment of microbiologically influenced corrosion in sulfur recovery unit

equipment. J. Chem. Res. Innov. Soc. 2(3) (2025) 21–32.
6-A.S. Al-Wuhaib, H. Sitepu, H.S. Khanfar, W.A. Algozeeb, A.M. Wade, Microbial and compositional characterization of oil and sludge deposits from crude pipelines. In: Microbiological Challenges in the Energy Industries; CRC Press, Boca Raton, FL, 2025.
7-A.S. AlEnezi, H. Sitepu, A. Owais, Characterization of sludge deposits in nitrogen generation systems using quantitative crystallography. J. Chem. Res. Innov. Soc. 2(4) (2025) 4–12.
8-M.S. Al-Dossary, H. Sitepu, Advanced quantitative phase analysis of sludge deposits in air-compression facilities. J. Chem. Res. Innov. Soc. 2(4) (2025) 22–31.
9- H. Sitepu, T.M. Okasha, Quantitative crystallographic characterization of industrial deposits for integrity assessment. J. Chem. Res. Innov. Soc. 2(4) (2025) 32–39.
10-B.H. O'Connor, D.Y. Li, H. Sitepu, Strategies for correcting preferred orientation in X-ray powder diffraction using intensity ratio methods. Adv.X-Ray Anal. 34 (1990) 409–415.
11- B.H. O'Connor, D.Y. Li, H. Sitepu, Texture analysis in X-ray powder diffraction using the March function. Adv. X-Ray Anal. 35 (1991) 277–283.
12- H. Sitepu, B.H. O'Connor, D.Y. Li, Comparative evaluation of preferred orientation models using X-ray diffraction data. J. Appl. Crystallogr. 38 (2005) 158–167.
13- H. Sitepu, Assessment of preferred orientation using neutron powder diffraction data. J. Appl.
Crystallogr. 35(2002) 274–277.
14-R.J. Hill, Data collection strategies: fitting the experiment to the analytical objective. In: R.A. Young (Ed.), The Rietveld Method; Oxford University Press, Oxford, 1993; pp. 298–318.
15-E.J. Mittemeijer, U. Welzel, Modern Diffraction Methods; Wiley-VCH, Weinheim, 2013.

Authors

Dr. Mona Al-Dossary,is Lead Lab Scientist at Saudi Aramco'sRASD. She earnedher Ph.D. and M.Sc. in Chemistry from KAUST, focusing on advanced materials for selective carbon dioxide separation applications, and a B.Sc. from King Faisal University. With expertise in materials characterization, she has publishedover 10 papers and holds five patents in materials science and renewable energy.

Dr. Husin Sitepu, is a specialist in powder diffraction science, with expertise in quantitative phase analysis and crystal structure and texture refinement using the Rietveld method. His work supports catalyst development, QA/QC of drilling additives, and industrial failure analysis. He has authored over 70 peer-reviewed publications, holds a Ph.D. in Physics and remains actively engaged with ICDD, IUCr, and the NSSA.

كلـــدة
Kalada

About Kalada

Kalada was founded in 2016 and is a fully Saudi-owned business. Our specialty is offering cutting-edge chemical solutions that are specifically designed to meet the demands of top businesses in sectors including energy, petrochemicals, gas, and oil.

Our Vision

To be a leading provider of catalysts, adsorbents, and water treatment solutions in the Middle East and Europe.

Our Mission

We are committed to delivering top-tier chemical solutions to our clients, focusing on quality, innovation, and sustainability.

Our Core Values

Commitment: Upholding the highest ethical standards.

Customer Service: Providing dedicated and professional support to our clients

Innovation: Driving excellence through creativity

Our Locations

Dammam
A warehouse spanning 2,200 square meters.

Khobar
Our headquarter.

Jubail
A 12,000-square-meter, cutting-edge industrial complex.

Why Choose Kalada

- Over 8 years of experience in the field
- innovative solutions aligned with Saudi Vision 2030.
- A global supply network ensuring efficient service delivery to clients

+966 565595585 mohammad@kaladachem.com.sa www.kaladachem.com.sa

Comprehensive Services

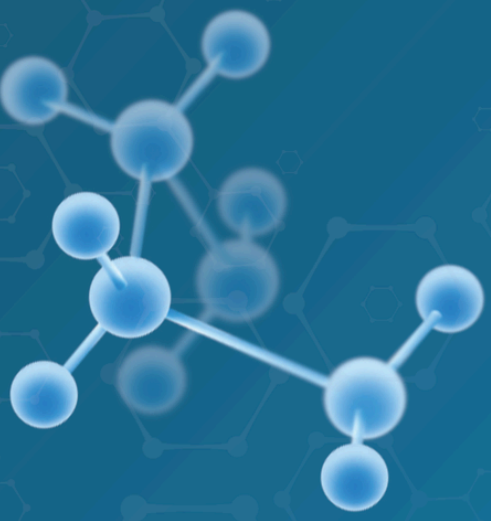

Specialized Chemicals:

- Refinery and Petrochemical Catalysts.
- Adsorbents: Activated Alumina, Molecular Sieves, Zinc Oxide, and Activated Carbon.
- Performance-enhancing additives for refined products.

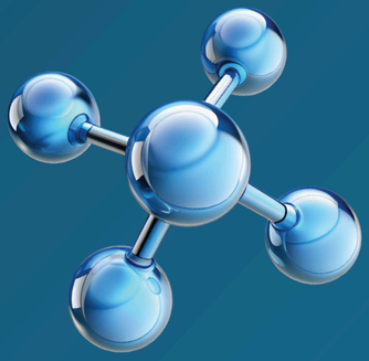

Water Treatment and Oil Field Service

- Oil and gas well chemical solutions, including demulsifiers, corrosion inhibitors, and scale inhibitors.
- Comprehensive oilfield and water management services.

Recovering valuable metals from industrial waste streams.

Supervision of catalyst loading and operational start-up.

Blending and repackaging of chemical materials.

Precious Metals Recovery Service:

Recovering valuable metals from industrial waste streams.

Stay connected by visiting our offices or contacting us via email or phone for further inquiries.

+966 565595585 mohammad@kaladachem.com.sa www.kaladachem.com.sa

Broadening the Scope of True Boiling Point (TBP) Distillation for Enhancing Crude Oil Assay Throughput

Dominic Kearney*, Abdulrahman Duailej and Saroj K. Panda
Saudi Aramco, Research & Analytical Services Department, Dhahran, 31311, Saudi Arabia
*Corresponding author Email: dominic.kearney@aramco.com

Abstract

Laboratory scale true boiling point (TBP) distillation is a technique which is central to the understanding of the compositions, properties and behavior of a crude oil. These characteristics are vital when determining the oil's market value, how to refine the crude in question in order to ascertain the value of the refined products and other derived products, such as in the case of crude to chemicals. The determination of a crude oil's TBP distribution is carried out according to the method ASTM D2892. This test method covers the procedure for the distillation of stabilized crude petroleum to a final cut temperature of 400 °C Atmospheric Equivalent Temperature (AET). It employs a fractionating column having an efficiency of 15 theoretical plates operated at a reflux ratio of 5:1. It also provides an estimate of the yields of fractions of various boiling ranges and is therefore valuable in technical discussions of a commercial nature. The conventional parameters recommended by ASTM D2892 may not be adequate in addressing any changes in business needs, for example optimization in yield of desired products derived from crude oil. The objective of this investigation is to reduce the time taken for a TBP distillation of a particular oil, while obtaining an understanding of how this will affect the overall separation quality and properties of the resultant distillation fractions. For this purpose, the study assesses the effect of variations in the reflux ratio, a key parameter in distillation, on factors such as the fraction yield, TBP distribution and degree of fraction overlap. Key findings show that, as expected, the decrease in reflux ratio results in lower quality fractions with increased overlap. However, reducing the reflux ratio significantly reduces the time taken to carry out a distillation, thereby increasing laboratory throughput. At the same time, it is shown that performing distillations with lower reflux ratio does not significantly affect the key properties (e.g. specific gravity, total sulfur viscosity etc.) of the resultant fractions. In short, the information gained from this study will help in increasing laboratory throughput with time sensitive crude oil assay studies.

KEYWORDS: Crude Economics, Reflux Ratio, Yield Optimization, True Boiling Point Distillation, Laboratory Throughput, Crude Oil Assay, Refinery Products

1. INTRODUCTION

Crude oil, as a source of affordable energy, is essential in maintaining the pace of modernization in both developing and developed economies in the decades to come.[1-7] Different fractions originating

from crude oil, separated according to boiling point, are used for a variety of fuels and chemicals. The detailed characterization of crude oil provides an opportunity to select the appropriate fraction(s) for the required products with specific qualities. However, as the composition of a crude oil mixture is so complex[3-16], for routine purposes, detailed characterization is discouraged. This is mainly due to the significant amount of time consuming and expensive techniques[17-25] (for example, chromatography and mass spectrometry) which must be employed. For practical purposes, crude oil assays are performed to gain an insight into the most efficient way for refiners to process and refine oils in a way that will maximize the profit margins.[26-29] Crude oil assays have been carried out historically as long as refining has been performed. Crude assays can provide valuable information regarding the oil's value on the world market and to ascertain the yields of the resultant refined products and ultimately, other derivative products, such as chemicals derived from crude. These crude oil assays are based primarily around laboratory scale true boiling point (TBP) distillation.[30-34] The determination of a crude oil's TBP distribution is generally carried out according to the standard method ASTM D2892. This test method covers the procedure for the distillation of stabilized crude oil, (crude that has had the associated light gases removed so as to be stable at atmospheric pressure) to a final temperature of 205 °C. It employs a fractionating column having an efficiency of 14 to 18 theoretical plates operated at a reflux ratio of 5:1. The method provides information regarding the yields of fractions of various boiling ranges obtained from the crude and is therefore valuable in technical discussions of a commercial nature.

Generally, crude oil assays are composed of three main areas. Firstly, as has already been described above, crude oil fractionation by distillation. Secondly, detailed analysis of each of the resultant fraction, and lastly, processing and interpretation of the data produced to yield a final report. Of these three areas, it is the quality of the distillation process which will have the most significant effect on the quality of the final assay report data produced. The standard test method ASTM D2892, which is generally used to fractionate crude oils during a crude oil assay, possesses certain constraints. These constraints exist mainly in terms of three important parameters, viz (1) distillation rate; the rate at which distillate is collected into the final product receiver, (2) reflux ratio; the ratio of the times of the open and closed positions of the reflux divider and (3) the preheating rate; the rate at which the feed sample is heated prior to distillation commencement. These three parameters represent a tradeoff between product fraction quality and distillation time. Indeed, the ASTM method states that "This test method offers a compromise between efficiency and time in order to facilitate the comparison of distillation data between laboratories." However, the parameters from ASTM D2892 may not be adequate in addressing ongoing changes in business needs; for example, oil appraisals for research purposes such as oil upgrading or crude to chemicals evaluations. As touched upon earlier, the main issue at hand is that of the quality of the distillation fraction obtained by the laboratory distillation procedure. That is, the extent to which the obtained fractions overlap with one another, causing some material which is

intended to be present in the lighter fraction to be present in the heavier fraction, and vice versa. The extent to which fraction overlap may be tolerated depends on the intended use of the desired fraction. In some instances, rapid distillations, yielding fractions of lower quality which overlap to a relatively large extent may be acceptable if time is a constraint. In short, the fractionation of crude oil by distillation on a shorter timescale, at the expense of fraction quality, will depend largely on the intended use of the collected fractions. If a full detailed assay is required, then this reduction in quality may not be appropriate. However, if fractions are required for, say, research investigations or pilot plant trials when developing new refinery processes, then this trade off of fraction quality for time may be acceptable.

With this in mind, the study presented here aims to extend the scope of the standard method by varying the reflux ratio of the distillation. In doing so, we will attempt to reduce the time taken for a TBP distillation of a particular oil. The extended scope will potentially provide an increase in laboratory throughput and help with time sensitive crude oil fractionation studies. The present work covers a series of distillations of a crude oil of API 33°. The study assesses the effect of variations in the distillation reflux ratio on the resultant fraction quality and extent to which the fractions overlap.

2. EXPERIMENTAL

2.1. Atmospheric Pressure Distillation of Crude Oil (ASTM D2892).

A weighed sample of 6 L of the stabilized crude was distilled to a maximum temperature of 205 °C. The sample was distilled into four discreet fractions, including the distillation residue, to predetermined cut points. These cut points correspond to 100 °C, 185 °C and 205 °C, in addition to the residue, consisting of all material with a boiling point > 205 °C. The distillation was repeated a number of times under varying distillation conditions. To calculate the distillation yields of the obtained cuts, the mass and density of the initial crude sample and subsequent straight run fractions and residue were measured and recorded. For the present study, the distillation rate, reflux ratio and sample preheating rate, as mandated by the standard method ASTM D2892 are 15 mL/min, 5:1 and 2.5 °C/min respectively. The setup of the distillation apparatus is illustrated in Figure 1. The parameter investigated in this study is reflux ratio, which has been varied as described in section 3 below.

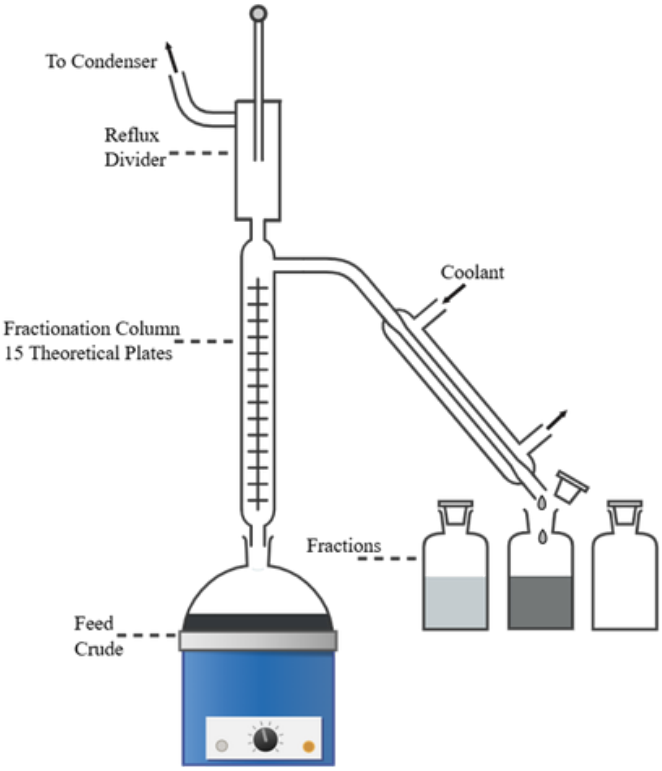

Figure 1. Schematic diagram of the distillation apparatus setup, based on method ASTM D2892. A more detailed view of the reflux divider setup can be seen below in Figure 2

The distillation fractions were evaluated for quality and extent of fraction overlap by measuring the density, specific gravity and API and comparing the results when the standard distillation parameters were varied. The density and API of each fraction was determined according to ASTM D4052. In this method, approximately 2 mL of sample is introduced into an oscillating sample tube and the change in the oscillation frequency as a result of the change in the mass of the tube is used along with calibration data to determine the density of the sample. From the density, the specific gravity is determined according to the following functions

$$SG = \frac{d}{0.999} \quad (1)$$

$$°API = \left(\frac{141.5}{SG}\right) - 131.5 \quad (2)$$

2.3. Distillation of Petroleum Products at Atmospheric Pressure (ASTM D86).

The distillation fractions were evaluated for quality and extent of fraction overlap by determining their boiling point distributions using atmospheric distillation. Specifically, the initial boiling point (IBP) and final boiling point (FBP) of each fraction generated were determined by ASTM D86. A 100 mL sample was distilled and observations of the vapor temperature and recovered volumes of condensate were made. A plot was constructed of the temperature vs. the recovered volume to yield a boiling point distribution curve of the sample under analysis. The volume of the residue and the losses were also considered.

2.4. Determination of Total Sulfur Content by Energy Dispersive X-Ray Fluorescence Spectrometry (ASTM D4294).

Distillation fractions were evaluated for total sulfur content. Briefly, a sample of distillate is placed in the beam emitted from an X-ray tube. The resultant excited characteristic X radiation is measured, and the accumulated count is compared with counts from previously prepared calibration samples to obtain the total sulfur concentration in weight percent.

2.5. Determination of Kinematic Viscosity by Stabinger Viscometer at 100 °F (ASTM D7042).

The test specimen was introduced into the measuring cells, which are held at 100 °F. The measuring cells consist of a pair of rotating concentric cylinders and an oscillating U-tube. The dynamic viscosity is determined from the equilibrium rotational speed of the inner cylinder under the influence of the shear stress of the test specimen and an eddy current brake in conjunction with adjustment data. The density is determined by the oscillation frequency of the U-tube in conjunction with adjustment data. The kinematic viscosity is calculated by dividing the dynamic viscosity by the density.

2.6. Determination of Refractive Index of Hydrocarbon Liquids (ASTM D1218)

The refractive index, that is, the ratio of the velocity of light (of specified wavelength) in air to its velocity in the test sample, is measured for each distillation fraction, using a high-resolution automatic digital type refractometer with the prism temperature maintained at 20°C.

2.7. Determination of Individual Components by High-Resolution Gas Chromatography (ASTM D6730).

The individual components of the samples under characterization are separated by gas chromatography. These components are then identified, quantified and grouped

into hydrocarbon types to yield the total percentage of paraffins, i-paraffins, olefins, naphthens and aromatics within each distillation fraction under review.

3. RESULTS AND DISCUSSION

The reflux ratio is defined as the ratio between the amount of material that is returned back to the distillation column and the amount of material that is transferred to the receiver (distillate). However, in this study, we will instead refer to the reflux ratio in term of time. That is, the time duration in which the reflux valve is closed, allowing the material to return back to the distillation column, compared with the amount of time in which the reflux valve is open, allowing the material to be removed and collected to the receiver. This is the notation used in the method ASTM D2892, where it assumed that when the reflux valve is open, there is total takeoff. However, in practice, when the reflux valve is open, a small portion of the distillate is returned back to the column. For this reason, the valve timing is evaluated and adjusted accordingly to give the required reflux ratio. Here, for simplicity, valve open and closed times are nominal. A schematic of the reflux setup is given in Figure 2.

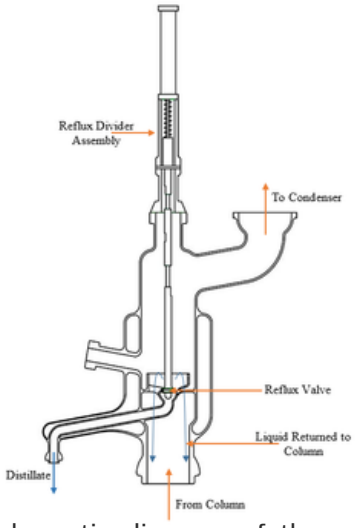

Figure 2. Schematic diagram of the reflux divider valve setup (while opening the valve allows the collection of distillate fractions and closing the valve allows the distillation of crude oil in the column).

An efficient distillation process allows the collection of clear-cut fractionations that are essential for either crude oil assay activities or for petrochemical related processes. The fraction quality is greatly influenced by the number of theoretical plates of the system, which is in turn affected by a number of distillation parameters, such as sample preheating rate, distillation rate (the rate, in mL/min at which distillate is removed from the head of the distillation column) and distillation reflux ratio, outlined earlier. Of these contributing parameters, reflux ratio was found to be the one parameter which contributed to the resultant fraction quality more predominantly, as well as a major determining factor in the time taken to complete a full distillation. Moreover, following fractionation, the quality of the separation is evaluated by determining the boiling point distribution (using method ASTM D86) and the density of each produced fraction. These analyses allow the fraction quality to be determined and evaluated against the varying distillation parameters in general and specifically in this investigation, against reflux ratio.

The quality of a distillation fraction (or cut), that is the degree of overlap, is defined by the amount of the heavier fraction which is present in the lighter fraction and the amount of the lighter fraction which is present in the heavier fraction. This degree of overlap may be determined by considering the boiling point distribution, determined by atmospheric distillation (method ASTM D86), of each of the two fractions in question. If comparison is made between the temperatures at which 95 $\%_{vol}$ and 5 $\%_{vol}$ are recovered, for the two adjacent fractions respectively, the overlap may be quantified as follows:

$$\Delta T = 5\ \%_{vol}T\ (heavy\ fraction) - 95\ \%_{vol}T\ (light\ fraction) \quad (3)$$

Where DT is the degree of overlap, 5 $\%_{vol}$T is the temperature at which 5 % of the total volume is recovered by D86 and 95 $\%_{vol}$T is the temperature at which 95 % of the total volume is recovered by D86. If DT>0, the separation is considered a gap. Conversely, if DT<0, the separation is considered to be an overlap. In this work, we will consider the magnitude of the degree of overlap. That is, irrespective of the sign.

In this work, fraction 1 has a boiling range of the initial boiling point (IBP) of the whole crude to 100 °C. Fraction 2 has a boiling range of 100 °C to 205 °C and fraction 3 has a boiling range of 205 °C to the final boiling point of the whole crude (FBP). The below table (Table 1) and plot (Figure 3) show the overlap (as an absolute magnitude) between fractions 1 and 2 for each of the distillation conditions. These overlaps were determined using the methodology outlined above.

Table 1. Degree of overlap (determined by ASTM D86) between distillation fractions 1 and 2. In this table, the magnitude of the overlap is expressed, irrespective of sign

Reflux Ratio (Closed:Open)	1:200	1:10	5:1	10:1
|Overlap| (°C)	17.7	14.7	5.9	11.2
Distillation Time (mins)	35	45	68	154

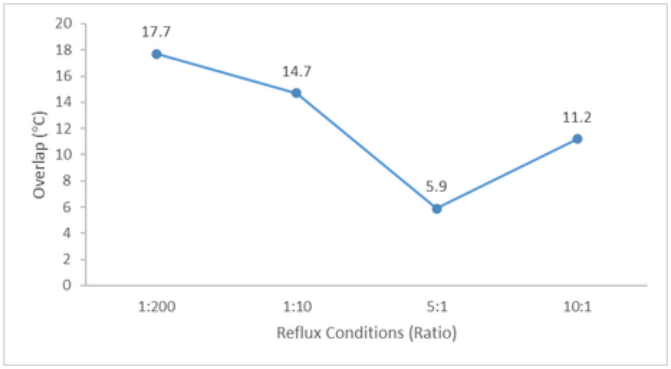

Figure 3. Reflux Condition (Ratio) vs. Degree of overlap (magnitude)

It is clear from Table 1 and Figure 3 that the degree of overlap decreases as the reflux ratio increases, or as the proportion of time for which the reflux valve is closed increases. This is to be expected as, when the reflux valve is closed, material is returned back to the column and there is more opportunity for gas liquid interaction within the column, thereby increasing the number of theoretical plates within the separation system and consequently increasing the prospect of component separation.

However, as the reflux ratio is decreased to 10:1, the degree of overlap is seen to increase. This is contrary to what would be expected when closing the reflux valve for extended periods of time. In such scenarios, it would be reasonable to expect that, as increased proportions of material are being returned back to the column, resulting in increased vapor-liquid interaction within the column, the number of theoretical plates of the system would increase, thereby giving more efficient component separation and consequently reducing the overlap further. However, this is not observed here. This observed phenomenon may potentially be explained by considering the setup of the instrument controls as explained below.

When the reflux valve is closed for extended periods of time, the sample in the distillation flask continues to be heated by the flask heater. This continued input of energy causes material to continue to be transferred to the packed column. Without removal of the distillate product from the head of the column, the column is likely to become overloaded. This overloading may result in column flooding, which in turn results in a reduction in column separation efficiency and subsequently increased fraction overlap. This phenomenon is further intensified by the fact that the distillation system is attempting to maintain a constant distillation rate. That is, the rate at which distillate product is collected in the product receiver. With the reflux valve being closed for extended periods of time, the distillation

rate drops and the instrument system compensates for this drop by increasing the flask temperature, thereby further enhancing the phenomenon described above.

3.1. Distillation Time.

When we consider the time taken to distill the oil to 205 °C for each of the reflux ratio conditions studies, we can observe that indeed, the distillation time increases with increasing reflux ratio (closed:open). As the proportion of time that the reflux valve is closed increases, the distillation time is increased. This is illustrated in Figure 4 below. With the decrease in reflux ratio (closed:open) distillation time decreases due to the rapid removal of distillate from the column head.

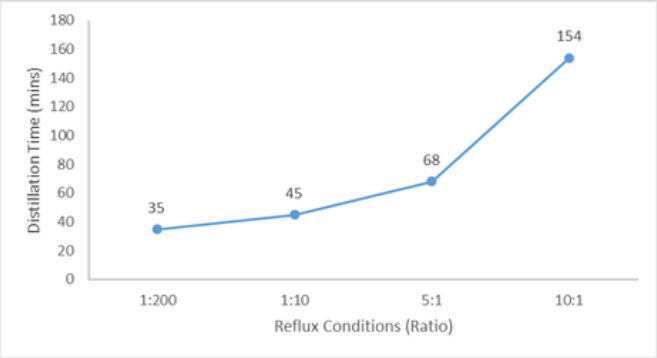

Figure 4. Reflux Ratio (closed:open) vs. Distillation Time

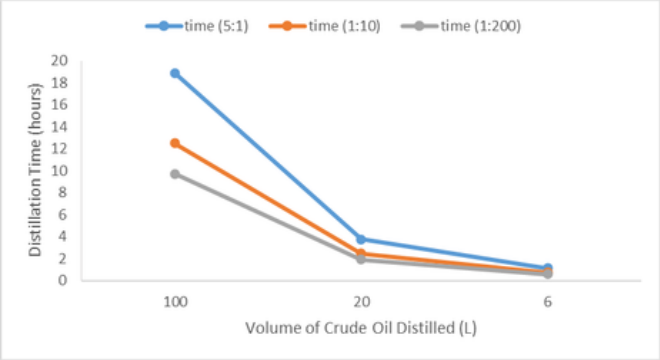

Figure 5. Predicted time for the distillation of larger volumes of crude oil at different reflux ratios

As mentioned above, this study assumes multiple distillations of 6 litre batches of crude oil at various system conditions. In many cases, larger quantities of distillate, at predefined cut temperatures are required. For example, 100 litres of a fraction with a boiling range from 185 °C to 565 °C. In this case, considering the volume constraints of the apparatus (6 litres) many batch runs will be required. These larger quantities may be needed for research purposes such as pilot plant trials to evaluate a new refinery catalyst. In such cases, where time might be a constraint, it may be expedient to decrease the reflux ratio, thereby expediting the overall distillation, even at the expense of the fraction quality. Figure 5 above illustrates how the reflux ratio affects the time taken to distill larger volumes of crude oil by 6 litre batches. This may be attractive to researchers and refinery process developers.

3.2. Assessment of Fraction Properties.

The degree of fraction overlap and the time taken to complete a distillation are clearly related to the reflux ratio of the system. However, we aim to assess whether the general quality of the resultant fractions may be maintained, in terms of key parameters such as sulfur content and API/density, even when collected at increased reflux ratios. The following series of tables and figures show the key properties (specific gravity, kinematic viscosity, total sulfur content and refractive index).

3.2.1. Effect on Specific Gravity

From Table 2 and Figure 6, we can observe that the total variation (that is the difference between the maximum and the minimum values) recorded for the specific gravity of fractions collected at the various reflux ratio conditions, is approximately 2.6% and 0.3% relative to the average value, for the fractions IBP - 100°C and 100°C - 185°C respectively. However, the difference between the measured values

for a reflux ratio of 5:1, that is the ratio recommended in method ASTM 2892, and the reflux ratio optimized for rapid distillation (1:200) is lower in comparison to the total variation.

Table 2. Specific gravities of the considered fractions collected at the specified reflux ratio conditions

Reflux Condition	Degree of overlap (Magnitude)	Fraction Parameter	IBP - 100°C	100°C - 185°C
1:200	17.7	Specific Gravity	0.6787	0.7521
1:10	14.7	Specific Gravity	0.6872	0.7518
5:1	5.9	Specific Gravity	0.6729	0.7544
10:1	11.2	Specific Gravity	0.6697	0.7538

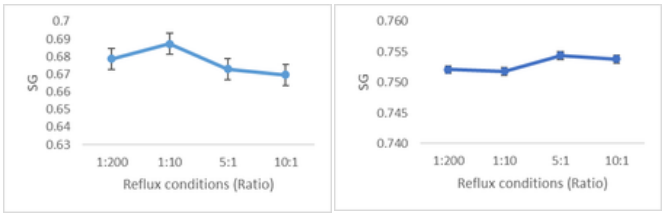

Figure 6. Plots of specific gravities of the fractions IBP to 100°C (left) and 100°C to 185 °C (right), collected at the specified reflux ratio conditions

3.2.2. Effect on Viscosity.

Similar phenomena observed for the effect of reflux ratio on specific gravity are observed when considering viscosity (Table 3 and Figure 7). In this case, the total variation is 10.6% and 1.4% relative to the average value, for the fractions IBP - 100°C and 100°C - 185°C respectively. As observed for specific gravity above, the difference between the measured values for a reflux ratio of 5:1, that is the ratio recommended in method ASTM 2892, and the reflux ratio optimized for rapid distillation (1:200) is again lower in comparison to the total variation.

Table 3. Viscosities of the considered fractions collected at the specified reflux ratio conditions

Reflux Condition	Degree of overlap (Magnitude)	Fraction Parameter	IBP - 100°C	100°C - 185°C
1:200	17.7	Viscosity (cSt @ 100°F)	0.4166	0.6505
1:10	14.7	Viscosity (cSt @ 100°F)	0.4842	0.6411
5:1	5.9	Viscosity (cSt @ 100°F)	0.4012	0.6322
10:1	11.2	Viscosity (cSt @ 100°F)	0.4974	0.6509

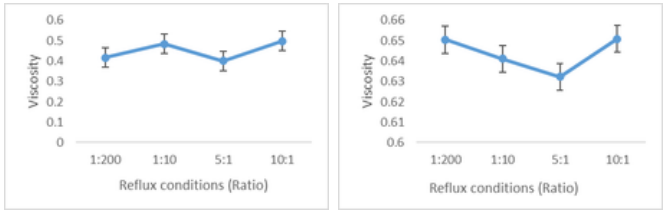

Figure 7. Plot of viscosities of the fractions IBP to 100°C (left) and 100°C to 185 °C (right), collected at the specified reflux ratio conditions

3.2.3. Effect on Total Sulfur Content.

Results observed for total sulfur content mirror the results obtained for specific gravity and viscosity above. These results are illustrated in Table 4 and Figure 8 below. The total variation is 29.5% and 4.5% standard deviation relative to the average value, for the fractions IBP - 100°C and 100°C - 185°C respectively. As observed for the other parameters above, the difference between the measured values for a reflux ratio of 5:1, that is the ratio recommended in method ASTM 2892, and the reflux ratio optimized for rapid distillation (1:200) is again lower in comparison to the total variation.

Table 4. Total sulfur content of the considered fractions collected at various reflux ratio conditions

Reflux Condition	Degree of overlap (Magnitude)	Fraction Parameter	IBP - 100°C	100°C - 185°C
1:200	17.7	Total Sulfur (wt%)	0.0283	0.0783
1:10	14.7	Total Sulfur (wt%)	0.013	0.1046
5:1	5.9	Total Sulfur (wt%)	0.0247	0.0769
10:1	11.2	Total Sulfur (wt%)	0.0225	0.082

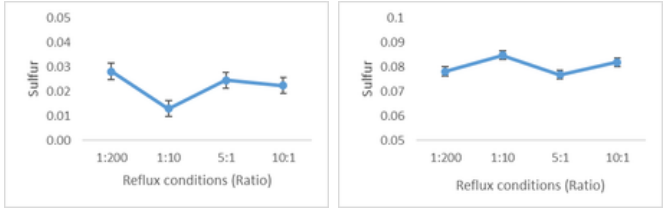

Figure 8. Plot of total sulfur of the fractions IBP to 100°C (left) and 100°C to 185 °C (right), collected at the specified reflux ratio conditions

Until now, it is not well understood the reasoning behind this observed phenomenon. Further study may reveal its cause. Due to constraints in time and resources, it is not reasonable to repeat the distillation process many times and our

study did not cover many repetitions of the distillations

3.2.4. Effect on Refractive Index.

In addition to specific gravity, viscosity and sulfur, the refractive index of the fractions with boiling ranges IBP - 100°C and 100°C - 185°C were measured at the various reflux ratios. These results are illustrated in Table 5 and Figure 9.

Table 5. Refractive Index of the considered fractions collected at various reflux ratio conditions

Reflux Condition	Degree of overlap (Magnitude)	Fraction Parameter	IBP - 100°C	100°C - 185°C
1:200	17.7	Refractive Index	1.38220	0.0783
1:10	14.7	Refractive Index	1.39279	0.1046
5:1	5.9	Refractive Index	1.38117	0.0769
10:1	11.2	Refractive Index	1.38625	0.0820

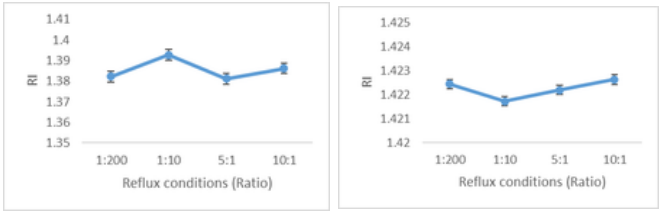

Figure 9. Plot of Refractive Indices of the fractions IBP to 100°C (left) and 100°C to 185 °C (right), collected at the specified reflux ratio conditions

Here, the total variation in refractive index is 0.8% and 0.06% relative to the average value, for the fractions IBP - 100°C and 100°C - 185°C respectively. Comparable to the phenomena observed for the other parameters, in the case of refractive index, the difference between the measured values for a reflux ratio of 5:1, that is the ratio recommended in method ASTM 2892, and the reflux ratio optimized for rapid distillation (1:200) is again observed to be lower in comparison to the total variation.

3.2.5. Effect on Hydrocarbon Types.

As well as the evaluation of the fundamental properties of the fractions at various distillation conditions, the hydrocarbon types were also considered. That is the percentage of paraffins, i-paraffins, olefins, naphthenes and aromatics (PIONA). As the distillation products are straight run cuts, no olefins were present. Figures 10 and 11 illustrate the percentage of each of these hydrocarbon types present in fractions corresponding to IBP-100°C and 100°C-185°C respectively, at the various distillation conditions studies. It is evident from these plots that, in the case of the light fraction (IBP-100°C), as the reflux ratio is varied from 5:1 to 1:10, the proportion of paraffins increases, with a corresponding decrease in i-paraffins, aromatics and naphthenes. A similar phenomenon is observed when considering the hydrocarbon types present in fractions corresponding to 100°C-185°C at the various distillation conditions. In both cases, this increase in the proportion of paraffins, (with a corresponding decrease in i-paraffins, aromatics and naphthenes) as the reflux ratio changes from 5:1 to 1:10, with the variation in distillation conditions may be attributed to heavier paraffins, which would normally be present in the heavier fraction (100°C-185°C) breaking through into the lighter fraction (IBP-100°C) due to increased fraction overlap caused by reduced selectivity of the fractionation process at lower reflux ratios.

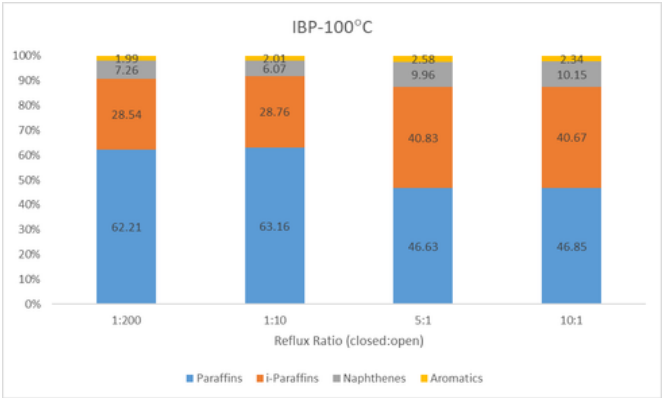

Figure 10. Graph of the proportion (%) of each hydrocarbon type in the IBP to 100°C fraction at different distillation conditions.

As mentioned, the case of the heavier fraction (100°C-185°C) is similar to the lighter fraction (IBP-100°C), where the

proportion of aromatics and napthenes reduces with the change from a reflux ratio of 5:1 to 1:10. However, in this case, rather than the proportion of i-paraffins reducing and the proportion of paraffins increasing accordingly, the proportion of i-paraffins remains relatively constant across the various distillation conditions, with the proportion of aromatics and naphthenes reducing accordingly. This phenomenon may be attributed to the fact that, at higher temperatures, fractions tend to be more paraffinic. This would suggest that, at a reflux ratio of 1:10, there is more propensity for paraffinic hydrocarbon types to break through from the 185°C+ (residue) to the 100°C-185°C fraction.

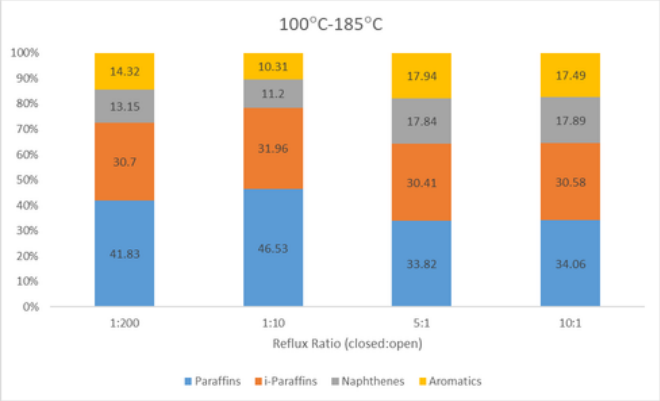

Figure 11. Graph of the proportion (%) of each hydrocarbon type in the 100°C to 185°C fraction at different distillation conditions.

4. CONCLUSIONS

Distillation of crude oil is often a compromise between time and fraction quality. That is, the degree of overlap between adjacent distillation fractions. There may be scenarios where it may be more desirable to sacrifice fraction quality in favor of time. For example, where large volumes of a particular fraction are required for further work, perhaps for pilot plant trials, where multiple batch distillations must be performed in order to acquire the necessary volumes. In such cases the reflux ratio may be increased to reduce the time taken to collect the fraction volumes required. Additionally, in some cases, it may be desirable to expedite the distillation process when carrying out a crude oil assay. Especially when data is required in a short timescale such as when urgent operational decisions need to be made. For example, refinery feed cargo offloading and assessment, scenarios where process and control systems are involved or when critical decisions need to be made with regards to crude blending. It is clear that reducing the distillation time by reducing the reflux ratio yields lower quality distillation products. However, in these cases it will certainly be expedient to perform a rapid assay distillation and, if necessary, correct or smooth any produced distillation curve and assay data using commercially available crude assay management tools. Indeed, comparison and evaluation studies to assess the correlation, precision and bias between assays involving rapid distillations described here, coupled with data modeling and smoothing and assays involving traditional 15/5 distillation (detailed in ASTM D2892) is proposed as our next phase in this line of study.

The relationship between fraction properties such as specific gravity, viscosity & total sulfur content and reflux ratio is small, practically constant when we account for the error across the entire procedure. This small variation may well be attributed simply to statistical variation inherent in the overall process, from distillation to analytical measurements. This observation indicates that reflux ratio may be altered without significantly influence on the physical and chemical properties of the distillation fractions.

The observed variation in the relative proportions of hydrocarbon types with

different reflux ratios is rationalized by considering the variation in hydrocarbon types with crude oil boiling point distribution and the difference in overlap for different reflux ratios.

5. ACKNOWLEDGMENT

The authors would like to thank Saudi Aramco for allowing the publication of this work.

Author Contributions: Conceptualization, Dominic Kearney; methodology, Dominic Kearney, Abdulrahman Duailej and Saroj K Panda; validation, Dominic Kearney, Abdulrahman Duailej and Saroj K Panda; data curation, Abdulrahman Duailej.; writing-original draft preparation, Dominic Kearney; writing—review and editing, Dominic Kearney and Saroj K Panda; supervision, Saroj K Panda. All authors have read and agreed to the published version of the manuscript.

Funding: This research received no external funding

Conflicts of Interest: The authors declare no conflict of interest.

6. REFERENCES

1. Maugeri, L., Science and industry: Oil: Never cry wolf-why the petroleum age is far from over. Science (Washington, DC, U. S.) 2004, 304 (5674), 1114-1115.
2. Panda, S. K.; Andersson, J. T.; Schrader, W., Mass-spectrometric analysis of complex volatile and nonvolatile crude oil components: A challenge. Anal. Bioanal. Chem. 2007, 389 (5), 1329-1339.
3. Farmani, Z.; Vetere, A.;Poidevin, C.; Auer, A. A.; Schrader, W., Studying Natural Buckyballs and Buckybowls in Fossil Materials. Angew. Chem., Int. Ed. 2020, 59 (35), 15008-15013.
4. Santos, J. M.; Wisniewski, A.; Eberlin, M. N.; Schrader, W., Comparing crude oils with different API gravities on a molecular level using mass spectrometric analysis. part 1: whole crude oil. Energies (Basel, Switz.) 2018, 11 (10), 2766/1.
5. Ruiz, W.; Moulian, R.;Rodgers, R. P.; Giusti, P.; Bouyssiere, B.; Marshall, A. G.; Barrere-Mangote, C.; Guillemant, J., Past to Future: Application of Gel Permeation Chromatography from Petroleomics and Metallopetroleomics to New Energies Applications: A Minireview. Energy Fuels 2023, 37 (13), 8867-8882.
6. Rodgers, R. P.; Chacon Patino, M. L.; Bouyssiere, B.; Giusti, P.;Mangote, C.; Afonso, C.; Marshall, A. G.; Hendrickson, C. L. In An illuminating 20 years of Petroleomic research by high-field fourier transform ion cyclotron resonance mass spectrometry, American Chemical Society: 2022.
7. Glattke, T. J.; Chacon-Patino, M. L.; Hoque, S. S.;Ennis, T. E.; Greason, S.; Marshall, A. G.; Rodgers, R. P., Complex Mixture Analysis of Emerging Contaminants Generated from Coal Tar- and Petroleum-Derived Pavement Sealants: Molecular Compositions and Correlations with Toxicity Revealed by Fourier Transform Ion Cyclotron Resonance Mass Spectrometry. Environ. Sci. Technol. 2022, 56 (18), 12988-12998.
8. Marshall, A. G.; Rodgers, R. P., Petroleomics: the next grand challenge for chemical analysis. Acc Chem Res 2004, 37 (1), 53-59.
9. Panda, S. K.; Andersson, J. T.; Schrader, W., Characterization of supercomplex crude oil mixtures: what is really in there? Angew. Chem., Int. Ed. 2009, 48 (10), 1788-1791.
10. Palacio Lozano, D. C.; Thomas, M. J.; Jones, H. E.; Barrow, M. P., Petroleomics: Tools, Challenges, and Developments. Annu Rev Anal Chem (Palo Alto Calif) 2020,13 (1), 405-430.
11. Palacio Lozano, D. C.; Gavard, R.;Arenas-

Diaz, J. P.; Thomas, M. J.; Stranz, D. D.; Mejia-Ospino, E.; Guzman, A.;Spencer, S. E. F.; Rossell, D.; Barrow, M. P., Pushing the analytical limits: new insights into complex mixtures using mass spectra segments of constant ultrahigh resolving power. Chem. Sci. 2019, 10 (29), 6966-6978.
12. Molnarne Guricza, L.; Schrader, W., Optimized asphaltene separation by online coupling of size exclusion chromatography and ultrahigh resolution mass spectrometry. Fuel 2018, 215, 631-637.
13. Molnarne Guricza, L.; Schrader, W., Argentation chromatography coupled to ultrahigh-resolution mass spectrometry for the separation of a heavy crude oil. J. Chromatogr. A 2017, 1484, 41-48.
14. Hegazi, A. H.; Fathalla, E. M.; Panda, S. K.;Schrader, W.; Andersson, J. T., High-molecular weight sulfur-containing aromatics refractory to weathering as determined by Fourier transform ion cyclotron resonance mass spectrometry. Chemosphere 2012, 89 (3), 205-212.
15. Rodgers, R. P.; Hendrickson, C. L.; Holder Montenegro, C. A.; Tello-Rodriguez, A. J.; Potu, T.;Shung, B.; Hagan, M.; Weisbrod, C. R.; Giusti, P.;Ruger, C. P.; Aguilera, M. L.; Vallverdu, G. S., Internal Calibration without Internal Calibrants by Mass Difference Analysis in FT-ICR Mass Spectrometry. Anal. Chem. (Washington, DC, U. S.) 2025, 97 (34), 18543-18552.
16. Rueger, C. P.; Neumann, A.;Koesling, P.; Vesga Martinez, S. J.; Chacon-Patino, M. L.; Rodgers, R. P.; Zimmermann, R., Addressing Thermal Behavior and Molecular Architecture of Asphaltenes by a Thermal-Optical Carbon Analyzer Coupled to High-Resolution Mass Spectrometry. Energy Fuels 2022, 36 (17), 10177-10190.
17. Cho, E.; Witt, M.;Hur, M.; Jung, M.-J.; Kim, S., Application of FT-ICR MS Equipped with Quadrupole Detection for Analysis of Crude Oil. Anal. Chem. (Washington, DC, U. S.) 2017, 89 (22), 12101-12107.
18. Corilo, Y. E.; Vaz, B. G.;Simas, R. C.; Lopes Nascimento, H. D.; Klitzke, C. F.; Pereira, R. C. L.; Bastos, W. L.; Santos Neto, E. V.; Rodgers, R. P.; Eberlin, M. N., Petroleomics by EASI(±) FT-ICR MS. Anal. Chem. (Washington, DC, U. S.) 2010, 82 (10), 3990-3996.
19. Nocun, M.; Andersson, J. T., Argentation chromatography for the separation of polycyclic aromatic compounds according to ring number. J. Chromatogr. A 2012, 1219, 47-53.
20. Panda, S. K.; Schrader, W.; Andersson, J. T., β-Cyclodextrin as a stationary phase for the group separation of polycyclic aromatic compounds in normal-phase liquid chromatography. J. Chromatogr. A 2006, 1122 (1-2), 88-96.
21. Nolte, T.; Andersson, J. T., Capillary electrophoretic methods for the separation of polycyclic aromatic compounds. Polycyclic Aromat. Compd. 2011, 31 (5), 287-338.
22. Sripada, K.; Andersson, J. T., Liquid chromatographic properties of aromatic sulfur heterocycles on a Pd(II)-containing stationary phase for petroleum analysis. Anal. Bioanal. Chem. 2005,382 (3), 735-741.
23. Muller, H.; Adam, F. M.;Panda, S. K.; Al-Jawad, H. H.; Al-Hajji, A. A., Evaluation of Quantitative Sulfur Speciation in Gas Oils by Fourier Transform Ion Cyclotron Resonance Mass Spectrometry: Validation by Comprehensive Two-Dimensional Gas Chromatography. J. Am. Soc. Mass Spectrom. 2012,23 (5), 806-815.
24. Vetere, A.; Alachraf, M. W.; Panda, S. K.;Andersson, J. T.; Schrader, W., Studying the fragmentation mechanism of selected components present in crude oil by collision-induced dissociation mass spectrometry. Rapid Commun. Mass

Spectrom. 2018, 32 (24), 2141-2151.
25. Panda, S. K.; Al-Hajji, A. A.; Muller, H.; Koseoglu, O. R., Ligand exchange chromatography: a vital dimension for the reliable characterization of heterocycles in crude oils and refined products. Anal. Bioanal. Chem. 2011,400 (5), 1231-1239.
26. Shishkova, I.; Stratiev, D.;Kolev, I. V.; Nenov, S.; Nedanovski, D.; Atanassov, K.; Ivanov, V.; Ribagin, S., Challenges in Petroleum Characterization-A Review. Energies (Basel, Switz.) 2022, 15 (20), 7765.
27. Watt, M. R.; Roussis, S. G. In Crude assay, Springer: 2006; p 103.
28. Peterson, J. L.; Cannon, H. G., Crude-oil assays. Pet. Process. 1946, 1, 113.
29. Turner, S. D.; Conant, F. C., Correlating and showing crude oil assay data. Oil Gas J. 1937, 35 (No. 45).
30. Stratiev, D.; Shishkova, I.; Dinkov, R.;Sotirov, S.; Sotirova, E.; Atanassov, K.; Ribagin, S.;Nikolova, R.; Veli, A.; Palichev, G.; Stratiev, D. D., Do the True Boiling-Point Distillation Yields of Crude Oil Blends Obey the Additive Blending Rule? Processes 2023, 11 (7), 1879.
31. Lopes, M. S.; da Rocha Watanabe, E. R. L.; Savioli Lopes, E.; Gomes, V. M.;Savioli Lopes, M.; Medina, L. C.; Maciel Filho, R.; Wolf Maciel, M. R., Extending the true boiling point curve of a heavy crude oil by means of molecular distillation and characterization of the products obtained. Pet. Sci. Technol. 2017, 35 (14), 1523-1529.

Authors

Dr. Saroj Panda is a Research Science Consultant at Saudi Aramco, bringing over two decades of specialized expertise in the characterization of petroleum hydrocarbons, refinery additives, oilfield chemicals, and polymers using state-of-the-art analytical techniques. Dr. Panda has co-authored more than 45 scientific publications, co-invented 6 patents, and has shared his insights at over 50 international conferences. His work has consistently driven innovation and technical progress within the energy sector

Dominic Kearney is a Lead Laboratory Scientist at Saudi Aramco. He earned his PhD from University College London. After completing his studies, he gained valuable experience in several hydrocarbon characterization laboratories, including roles at Expro and Intertek. In 2013, he joined Saudi Aramco in Riyadh, and later became part of the Research and Development Center (R&DC), now known asRASD. Within the company, he has focused on crude oil characterization, with a particular emphasis on crude fractionation. Dominic has played a key role in advancing the company's crude assay program and has contributed to the development of enhanced crude compatibility capabilities.

Abdulrahman Duailej is a Lab Tech Specialist at Saudi Aramco, where he has been working in the field of crude oil and petroleum product characterization since joining the company in 2007. His area of specialization is laboratory-scale crude oil and product distillation, and he currently oversees operations in the distillation laboratory, ensuring accurate and reliable data for product analysis and process optimization.

Mineralogical Resolution of Limestone Composition by Combined XRF and XRD–Rietveld Analysis *

Mona S. Al-Dossary* and Husin Sitepu**
Research and Analytical Services Department, Saudi Aramco, P.O. Box 62, Dhahran 31311, Kingdom of Saudi Arabia
*Correspondence: mona.dossary.2@aramco.com
**Retired from Saudi Aramcoafter more than 16 yearsof service in cutting-edge research

Abstract

Accurate characterization of limestone requires clear differentiation between bulk chemical composition and true mineralogical constitution. In this study, a representative limestone sample was investigated using X-ray fluorescence (XRF) spectroscopy and powder X-ray diffraction (XRD) coupled with Rietveld refinement. XRF analysis provided rapid multi-element quantification, confirming a calcium-rich carbonate composition with subordinate magnesium and silica. However, elemental data alone cannot unambiguously determine phase identity, cation distribution, or silica polymorphism, as stoichiometric oxide or carbonate assignments rely on implicit and potentially non-unique assumptions regarding mineral hosts.

Quantitative phase analysis by XRD–Rietveld refinement resolved these limitations through direct identification and structural modeling of crystalline phases. The limestone was found to consist predominantly of calcite (86.3 wt%), accompanied by dolomite (12.6 wt%) and minor quartz (1.1 wt%). No evidence of crystalline magnesite or alternative silica polymorphs was detected within instrumental detection limits. Refinement reliability indicators (R_P, R_{WP}, c^2) demonstrated excellent model agreement and reproducibility.

The findings highlight the complementary yet fundamentally distinct roles of XRF and XRD in carbonate characterization. While XRF provides robust bulk chemical information, quantitative mineralogical resolution in carbonate systems can only be reliably achieved through XRD coupled with Rietveld refinement. This integrated analytical approach is therefore essential for accurate phase discrimination in limestone materials relevant to industrial and geochemical applications.

1. Introduction

Limestone is a fundamental geological and industrial material widely utilized in cement production, construction, metallurgy, environmental remediation, and as a principal component of carbonate hydrocarbon reservoirs. Its engineering performance, reactivity, mechanical strength, and reservoir properties are governed not solely by bulk chemical composition, but more critically by mineralogical constitution, phase proportions, and crystal chemistry. Accurate discrimination among calcite, dolomite, and accessory silicate phases is therefore essential for reliable scientific interpretation and industrial decision-

making.

X-ray fluorescence (XRF) spectroscopy is extensively employed for limestone characterization due to its rapid analysis, high precision, and excellent reproducibility in quantifying major and trace elements [1,2]. XRF measures characteristic fluorescence energies and intensities, enabling robust determination of elemental abundances. However, the technique is intrinsically insensitive to crystallographic structure. Consequently, elemental data are commonly converted into stoichiometric oxides or carbonates (e.g., $CaCO_3$, $MgCO_3$, SiO_2) based on idealized chemical assumptions. While analytically convenient, such conversions are mineralogically non-unique and may obscure the true distribution of elements among crystalline phases.

Powder X-ray diffraction (XRD), in contrast, directly probes long-range atomic order by measuring the positions and intensities of Bragg reflections. When coupled with Rietveld refinement, full-pattern quantitative phase analysis becomes possible through simultaneous refinement of structural and microstructural parameters [3,4]. This methodology is widely recognized as the benchmark approach for quantitative mineralogical analysis of multiphase materials, including carbonate systems [5,6]. Unlike XRF, XRD–Rietveld refinement resolves phase identity, distinguishes polymorphs, and quantifies mineral abundances without reliance on implicit stoichiometric assumptions.

The complementary roles of XRF and XRD in modern analytical workflows are illustrated schematically in Figure 1. Conceptually, XRF addresses the question: Which elements are present, and in what concentrations? In contrast, XRD answers: Which crystalline phases are present, and in what proportions? These techniques therefore provide distinct but synergistic information and cannot be used interchangeably.

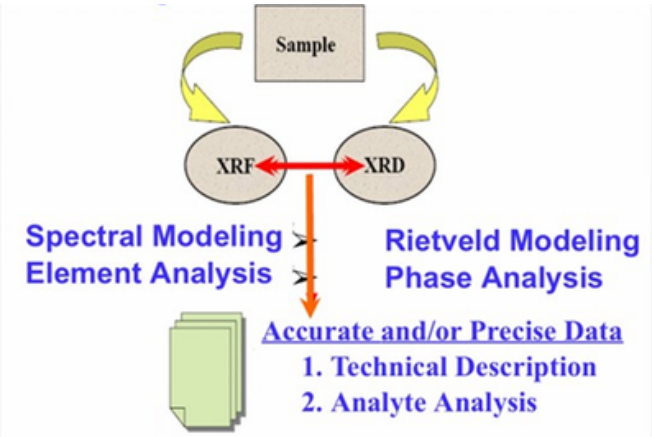

Figure 1. Conceptual integration of XRF and XRD in the modern X-ray laboratory [14], illustrating the complementary relationship between elemental analysis (XRF) and crystallographic phase quantification (XRD–Rietveld).

This distinction is particularly critical in carbonate systems relevant to petroleum geology and reservoir engineering, where porosity evolution, mechanical behavior, diagenetic pathways, and geochemical reactivity depend sensitively on mineral assemblages. Elemental data alone cannot establish whether calcium is hosted exclusively in calcite or partitioned into dolomite, whether magnesium forms an independent magnesite phase or is structurally incorporated within dolomite, or whether silica occurs as quartz, another polymorph, or an amorphous component. Resolution of such questions requires crystallographic phase identification and quantitative refinement [7–22].

Figure 2. Photograph of the representative limestone sample analyzed in this study, illustrating

a polymineralic carbonate material requiring integrated chemical and structural characterization.

2. OBJECTIVE

The objective of this study is to demonstrate, using a representative limestone sample (Figure 2), that definitive mineralogical characterization of carbonate systems requires XRD coupled with Rietveld refinement (Figure 1) [7–22], while XRF provides essential but non-diagnostic bulk chemical context [1-2,14-22]. By directly comparing elemental composition with quantitative phase analysis results, the study aims to clarify the fundamentally different analytical questions addressed by each technique and to establish the necessity of integrated chemical and crystallographic methodologies for accurate limestone characterization in geological, industrial, and petroleum-related applications.

3. Experimental Work

3.1 X-ray Fluorescence (XRF) Analysis

The bulk chemical composition of the limestone sample was determined by X-ray fluorescence (XRF) spectroscopy following standard preparation procedures appropriate for carbonate materials [1-2,14-22]. The sample was oven-dried to remove moisture, finely ground to a homogeneous powder, and thoroughly mixed to minimize particle-size and matrix effects prior to analysis [1-2,14-22]. Such preparation is essential to ensure analytical precision and reproducibility in multi-element quantification.

The XRF instrument measured characteristic fluorescence emissions over a broad energy range, enabling simultaneous determination of major and minor elemental constituents [1-2,14-22]. Quantification was performed using a fundamental-parameters-based calibration approach to correct for matrix absorption and enhancement effects. Elemental concentrations were reported in conventional stoichiometric form as oxides or carbonates (e.g., $CaCO_3$, $MgCO_3$, SiO_2), consistent with standard limestone reporting practices [1-2].

However, this reporting format inherently assumes unique mineral hosts for each element. For instance, magnesium expressed as $MgCO_3$ implicitly suggests the presence of magnesite, while silicon reported as SiO_2 does not differentiate among quartz, alternative silica polymorphs, or amorphous silica phases [14]. As discussed in the Introduction, such conversions are chemically convenient but mineralogically non-unique [1,2,5,7].

Accordingly, the XRF results were interpreted strictly as accurate representations of bulk elemental composition. They were used to provide compositional context and internal consistency checks for subsequent diffraction-based phase analysis, rather than as definitive indicators of crystalline phase identity.

3.2 X-ray Diffraction (XRD) and Rietveld Refinement

Powder X-ray diffraction (XRD) data were collected using a laboratory diffractometer equipped with Cu Kα radiation [14-22]. The limestone sample was finely ground to reduce preferred orientation effects and scanned over a 2θ range sufficient to capture all diagnostically significant Bragg reflections associated with carbonate and silicate phases. Instrumental parameters were selected to ensure adequate angular resolution and counting statistics for reliable quantitative analysis [14].

Quantitative phase analysis was performed using the Rietveld refinement method, in

which a calculated diffraction pattern derived from crystallographic structure models is iteratively fitted to the observed pattern by least-squares minimization [3,4,14]. Structural models for calcite, dolomite, and quartz were obtained from established crystallographic databases and refined simultaneously to account for multiphase contributions.

Refinable parameters included scale factors (for phase quantification), background coefficients, unit-cell parameters, and peak-shape/profile parameters. The refinement procedure allows direct assignment of elements to specific crystal structures, thereby resolving ambiguities inherent in stoichiometric interpretations derived from bulk chemical data [3,4,14]. Unlike XRF-based compound estimation, XRD–Rietveld analysis determines mineral identity and relative abundance based on crystallographic evidence [3-13].

Refinement quality and model reliability were evaluated using standard agreement indices, including the profile residual (R_P), weighted profile residual (R_{WP}), and goodness-of-fit indicator (c^2), in accordance with established refinement protocols [3–15]. These statistical parameters provide objective measures of agreement between observed and calculated diffraction patterns and ensure robustness, internal consistency, and reproducibility of the quantitative phase model.

4. Results and Discussion

4.1 Elemental Composition by XRF Analysis

X-ray fluorescence (XRF) analysis provided quantitative bulk elemental composition of the investigated limestone. As established in Sections 1–3, XRF delivers precise multi-element data but does not provide crystallographic information. The instrument software converted elemental concentrations into conventional stoichiometric oxides or carbonates based on fundamental-parameters calibration. The results are summarized in Table 1.

The data clearly indicate a calcium-dominant carbonate material with subordinate magnesium and minor siliceous and aluminosilicate components. However, these compound assignments are strictly stoichiometric representations derived from elemental abundances and do not constitute mineral phase identification. Consequently, XRF alone cannot determine the crystallographic distribution of calcium, the structural host of magnesium, or the polymorphic state of silica.

Figures 3(a) and 3(b) illustrate the elemental concentrations and their corresponding stoichiometric reporting formats, respectively, as generated by the WDXRF software. These results provide essential chemical context but remain mineralogically non-diagnostic.

Table 1. Elemental composition of the limestone determined by XRF with corresponding stoichiometric assignments.

Element	Assigned Compound	Concentration (wt%)
Mg	**$MgCO_3$**	**2.91**
Al	Al_2O_3	0.39
Si	**SiO_2**	**1.16**
P	P_2O_5	0.01
S	SO_3	0.01
K	K_2O	0.06
Ca	**$CaCO_3$**	**95.16**
Ti	TiO_2	0.02
Mn	MnO	0.01
Fe	$FeCO_3$	0.20
Sr	SrO	0.06
Zr	ZrO_2	0.01
Cl	Cl	0.00

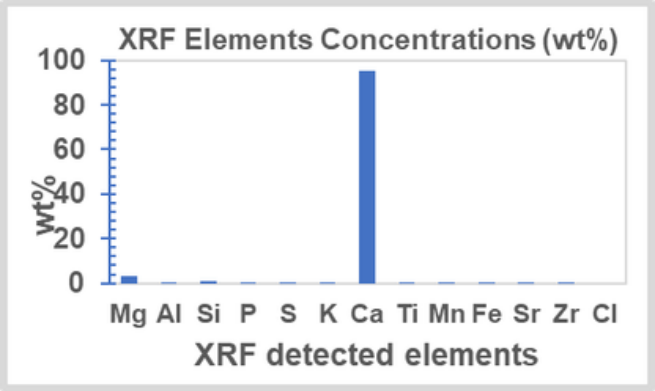

Figure 3(a). Relationship between XRF-detected elements and their concentration (wt%) obtained using the Malvern-PANalytical advanced high-resolution WDXRF instrument software.

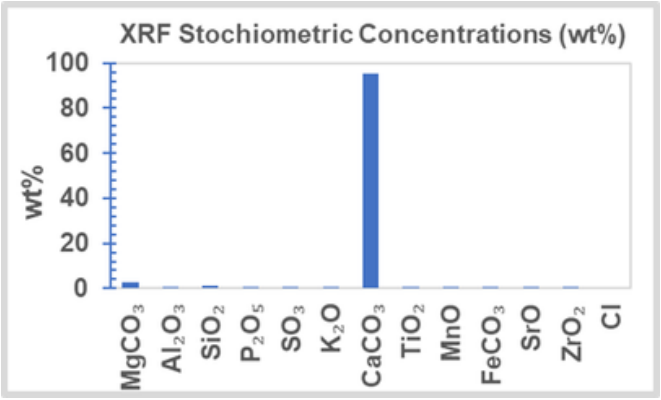

Figure 3(b). Relationship between XRF-stoichiometric chemical formulas and their concentration (wt%) obtained using the Malvern-PANalytical advanced high-resolution WDXRF instrument software.

4.2 Phase Identification and Quantification by XRD–Rietveld Refinement

To resolve the mineralogical ambiguities inherent in the XRF interpretation, powder X-ray diffraction coupled with full-pattern Rietveld refinement was employed. In contrast to elemental analysis, XRD directly probes long-range atomic order and enables unambiguous identification of crystalline phases.

The refinement produced excellent agreement between observed and calculated diffraction profiles (Figure 4), confirming the adequacy of the selected structural models. Three crystalline phases were identified without ambiguity: calcite ($CaCO_3$), dolomite [$CaMg(CO_3)_2$], and quartz (SiO_2). No additional carbonate phases, silica polymorphs, or accessory crystalline minerals were required to account for the observed diffraction intensities.

Refinement reliability indicators demonstrate the robustness of the model: R_P=6.8%, R_{WP}=8.9%, and c^2=1.42. These values fall within accepted limits for multiphase carbonate systems and confirm statistical validity and reproducibility of the quantitative phase model.

Table 2. Quantitative phase composition determined by XRD–Rietveld refinement.

Mineral Phase	Chemical Formula	Weight Fraction (wt%)
Calcite	$CaCO_3$	86.3
Dolomite	$CaMg(CO_3)_2$	12.6
Quartz	SiO_2	1.1
Total		**100**

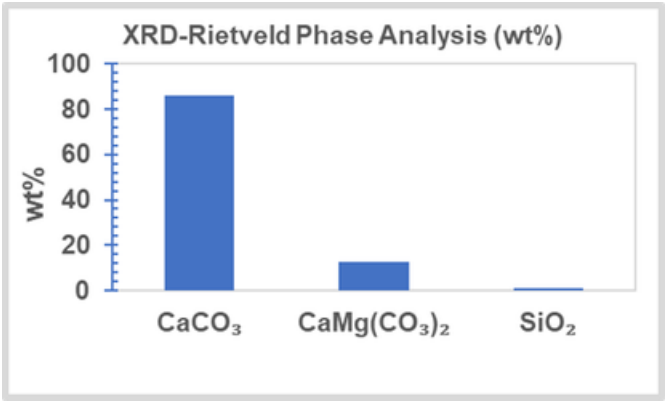

Figure 4. Relationship between XRD-identified phases and their phase compositions (wt%) obtained from Rietveld refinement.

4.3 Distribution of Calcium Between Carbonate Phases

XRF assigns calcium to $CaCO_3$ under the implicit assumption that calcite is the sole calcium-bearing phase. The XRD–Rietveld results clearly demonstrate that this assumption is not valid for the investigated sample.

Although calcite is dominant (86.3 wt%), a significant proportion of calcium is

structurally incorporated within dolomite (12.6 wt%). Thus, calcium is partitioned between two carbonate phases. This cation distribution cannot be resolved through elemental analysis alone and illustrates a fundamental limitation of stoichiometric interpretation based solely on XRF data.

4.4 Validation and Structural Nature of Silica

The XRF-derived SiO_2 content (1.16 wt%) closely corresponds to the quartz content quantified by XRD (1.1 wt%). This agreement confirms internal consistency between chemical and crystallographic data. However, the validity of the SiO_2 assignment is meaningful only because XRD establishes the mineralogical form of silicon.

The diffraction pattern exhibits reflections exclusively attributable to α-quartz, with no evidence of cristobalite or other silica polymorphs. Furthermore, the absence of a broad diffuse scattering background indicates that amorphous silica is negligible or below the instrumental detection limit.

These observations demonstrate that silica occurs solely as crystalline quartz. Such polymorphic discrimination is uniquely accessible through diffraction-based analysis and cannot be achieved using elemental techniques.

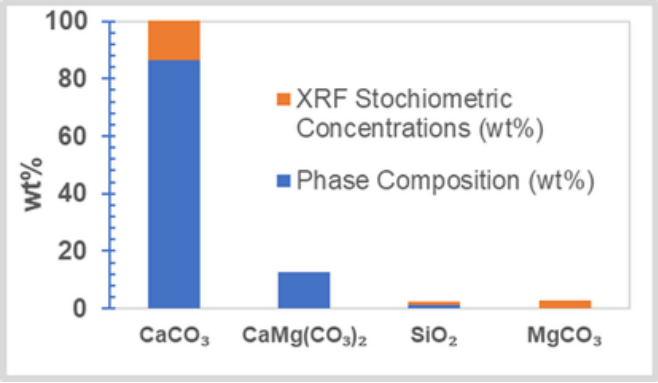

Figure 5. Correlation between XRD-identified phases and their phase compositions (wt%) obtained from Rietveld refinement with the stoichiometric chemical formulas and their concentration (wt%) obtained using the Malvern-PANalytical advanced high-resolution WDXRF instrument software.

4.5 Magnesium Host Phase and Absence of Magnesite

XRF reports magnesium as $MgCO_3$, implicitly suggesting the presence of magnesite. However, the XRD–Rietveld analysis detected no reflections corresponding to magnesite. Instead, magnesium is entirely incorporated within the dolomite structure, occupying ordered cation layers alternating with calcium.

The absence of a discrete magnesite phase confirms that the $MgCO_3$ assignment derived from XRF is mineralogically non-unique and potentially misleading. This finding reinforces the necessity of crystallographic verification when interpreting magnesium-bearing carbonate systems.

Conclusions

This study demonstrates that XRF and XRD address fundamentally different analytical questions in limestone characterization. XRF provides accurate and reproducible bulk elemental composition, whereas XRD coupled with Rietveld refinement delivers definitive mineral phase identification and quantification.

The principal conclusions are:

·Calcium is partitioned between calcite and dolomite and is not exclusively hosted by calcite, contrary to assumptions inherent in XRF-based stoichiometric reporting.

·Silicon occurs solely as crystalline α-quartz; no cristobalite or amorphous silica was detected within instrumental limits.

·Magnesium does not form a discrete magnesite phase but is structurally incorporated within dolomite.

·Stoichiometric oxide and carbonate assignments derived from XRF must be interpreted cautiously and validated by

crystallographic methods.

Overall, the results confirm that quantitative mineralogical resolution in carbonate systems can only be achieved through XRD–Rietveld refinement, with XRF serving as essential complementary chemical support. The integrated analytical framework presented here provides a robust, reproducible, and industry-relevant methodology for limestone characterization applicable to industrial processing, carbonate reservoir evaluation, and petroleum-related geochemical investigations.

Acknowledgments

The authors gratefully acknowledge the management of Saudi Aramco for granting permission to publish this work. Technical support provided by the Research and Analytical Services Department (RASD) and the Research and Development Center (R&DC) is sincerely appreciated.

The authors also thank the anonymous reviewers for their constructive comments, which significantly improved the clarity and rigor of the manuscript. An earlier version of this work was presented at the First Gulf Chemistry Association International Conference and Exhibition (GCA-2022), Kingdom of Bahrain, 15–17 November 2022.

REFERENCES

1.R. Jenkins, R.W.Gould, D. Gedcke, Quantitative X-ray Spectrometry, 2nd ed., Marcel Dekker,New York, 1995

2.P.J. Potts, A Handbook of Silicate Rock Analysis, Blackie Academic & Professional, Glasgow, 2008.

3.H.M. Rietveld,A profile refinement method for nuclearand magnetic structures. J. Appl. Crystallogr. 2 (1969) 65–71.

4.R.A.Young, (Ed.). The RietveldMethod, Oxford University Press, Oxford, 1993.

5.L.B.McCusker, R.B.VonDreele, D.E.Cox, D.Louër,P.Scardi, Rietveld refinement guidelines. J. Appl. Crystallogr. 32 (1999) 36–50.

6.D.L.Bish, J.E Post, Quantitative mineralogical analysis using the Rietveld full-pattern fitting method. Am. Mineral. 78 (1993) 932–940.

7.I.C.Madsen, N.V.Y. Scarlett, A.Kern, Description and survey of methodologies for the determination of amorphous contentvia X-ray powder diffraction. Z. Kristallogr. 216 (2001) 595– 604.

8.B.H.O'Connor, D.Y.Li, H.Sitepu, Strategies for correcting preferred orientation in X-ray powder diffraction using intensity ratio methods. Adv. X-Ray Anal. 34 (1991) 406–415.

9.B.H.O'Connor, D.Y.Li,H.Sitepu, Texture analysisin X-ray powderdiffraction using the March function. Adv. X-Ray Anal. 35(1992) 277–283.

10.H.Sitepu, B.H.O'Connor, D.Y. Li, Comparative evaluation of preferredorientation models using X-ray diffraction data. J. Appl. Crystallogr. 38(2005) 158–167.

11.H.Sitepu, Assessment of preferred orientation using neutron powder diffraction data. J. Appl. Crystallogr. 35 (2002) 274–277. H.Sitepu, Rietveldphase analysis of deposits formedin electric submersible pump components. Adv. X-Ray Anal. 63 (2020) 28–42.

12.R.J. Hill, Data collection strategies: fitting the experiment to the analytical objective. In: R.A.Young, (Ed.), The RietveldMethod; Oxford University Press: Oxford, 1993; pp. 298–318. R.A. Young, The Rietveld Method; Oxford University Press: Oxford, 1993.

13.E.J.Mittemeijer, U.Welzel, Modern Diffraction Methods; Wiley-VCH: Weinheim, 2013.

14.H.Sitepu, N.M.Al-Yami, I.M. Al-Zahrani, Textureeffects and quantitative Rietveld analysis of crystalline depositsfor failure investigation applications. Powder Diffraction 40(1) (2025) 7–20.

15.H.Sitepu, B.H. O'Connor, Obituary: Brian H. O'Connor (1940–2024). J. Appl. Crystallogr. 58 (2025) 1511–1512.

16.H.Sitepu, R.A.Al-Ghamdi, M.S.Al-Dossary, H.S. Khanfar, Quantitative phase analysis of crystalline deposits from refinery and gas-processing equipment using XRD. J. Chem. Res. Innov. Soc. 2(3) (2025) 11–20.

17.M. Nagu, H. Sitepu, W.A. Algozeeb, N.M. Alanazi, Quantitative XRD-based root cause analysis of filter sludge deposits in refinery systems. J. Chem. Res. Innov. Soc. 2(1) (2025) 33–46.

18.H.S. Khanfar, H. Sitepu, N.S. Alshihri, M.S. Al-Dossary, Zhu, X.; Al-Zahrani, I.M. Integrated assessmentof microbiologically influenced corrosion in sulfurrecovery unit equipment. J. Chem. Res. Innov. Soc. 2(3) (2025) 21–32

19.A.S. Al-Wuhaib, H. Sitepu, H.S. Khanfar, W.A. Algozeeb, A.M. Wade, Microbialand compositional characterization of oil and sludge depositsfrom crude pipelines. In: Microbiological Challenges in the Energy Industries; CRC Press: Boca Raton, FL,2025.
20.A.S. AlEnezi, H. Sitepu, A. Owais, Characterization of sludge depositsin nitrogen generation systems using quantitative crystallography. J. Chem. Res. Innov. Soc. 2(4) (2025) 4–12.
21.M.S. Al-Dossary, H. Sitepu, Advanced quantitative phase analysis of sludge deposits in air- compression facilities. J.Chem. Res. Innov.Soc. 2(4) (2025)22–31.
22.H. Sitepu, T.M. Okasha, Quantitative crystallographic characterization of industrial deposits for integrity assessment. J. Chem.Res. Innov. Soc.2(4) (2025) 32–39.

Author

Dr. Mona Al-Dossary, is Lead Lab Scientist at Saudi Aramco'sRASD. She earnedher Ph.D. and M.Sc. in Chemistry from KAUST, focusing on advanced materials for selective carbon dioxide separation applications, and a B.Sc. from King Faisal University. With expertise in materials characterization, she has publishedover 10 papers and holds five patents in materials science and renewable energy.

Dr. Husin Sitepu, is a specialist in powder diffraction science, with expertise in quantitative phase analysis and crystal structure and texture refinement using the Rietveld method. His work supports catalyst development, QA/QC of drilling additives, and industrial failure analysis. He has authored over 70 peer-reviewed publications, holds a Ph.D. in Physics and remains actively engaged with ICDD, IUCr, and the NSSA.

Developing Online Analyzer for Monitoring of THPS-Based Biocides in Large Seawater Injection Network

Xiangyang Zhu, Alexander Grigoryan, Mazen A. Saleh
Research and Analytical Services Department, Saudi Aramco, Saudi Arabia
Corresponding author: xiangyang.zhu@aramco.com

Abstract

Saudi Aramco operates the world's largest seawater treatment plant and transports millions of barrels of treated seawater every day for reservoir injection and pressure maintenance. Microbial activities in transportation pipelines are controlled through weekly injection of biocide products such as glutaraldehyde- or THPS-based biocides. To determine the treatment effectiveness and optimize the treatment program, samples are collected from various downstream locations for monitoring biocide residual concentrations, distribution, and microbial counts. However, sample collection, delivery, and analysis for biocide residual monitoring is a huge challenge for this large seawater injection system, especially for remote injection wells.

In this paper we will present the design, construction, and validation of an online analyzer for automatic detection and quantification of THPS-based biocides. The analyzer is based on the permanganate-THPS reaction and absorption measurement of permanganate solution at 525 nm for THPS detection and quantification. The analyzer was validated in the extensive laboratory acceptance tests with commercial biocide products. The dynamic detection range of the online THPS Analyzer is approximately 80-2000 ppmv of biocide formulation (or 20-800 ppmv of THPS) with measurement variation less than 10% and measurement accuracy within ±20% of the actual biocide concentration. The THPS Analyzer can automatically switch between non-slug mode and slug mode measurement depending on the measured biocide concentration and the pre-set comparator parameters.

Introduction

Saudi Aramco operates the world's largest seawater treatment plant and transportation pipeline network. Millions of barrels of the treated seawater are injected into oil reservoirs every day for pressure maintenance. The treatment plant sources the seawater from Arabian Gulf at Qurayyah with an average total dissolved solids (TDS) 57,700 mg/L and sulfate 4,280 mg/L, much higher than the typical seawater (TDS 35,000 mg/L and sulfate 2,650 mg/L) [1]. Introduction of large quantity of sulfate into oil reservoir promotes the proliferation of sulfate-reducing bacteria and archaea (SRB and SRA). Sulfate-reducing microorganisms are considered one of the most damaging microbes in oil and gas industry, causing microbiologically influenced corrosion (MIC) in the metal infrastructures, fouling and plugging of injection wells, formation damage, and reservoir souring [2-5]. To

minimize or control the negative impact of seawater injection, the seawater was treated in the treatment plant with various physical and chemical processes (e.g., disinfectant, nitrogen, oxygen scavenger, flocculant, coagulant, filtrations) to kill living organisms in the seawater, remove solids, small particles, and dissolved oxygen. Finally, the organic biocides are injected into the transportation pipelines for microbial control in the treated seawater [6-7]. Tetrakis(hydroxymethyl)phosphonium sulfate (THPS) and glutaraldehyde are the most common active ingredients in the formulations of the organic biocides widely used in oil and gas industry including Saudi Aramco [8-13].

The performance of biocides depends on concentration and contact time with microorganisms. Therefore, it is essential to monitor biocide residual concentration and distribution closely throughout the transportation network to ensure adequate microbial control. Saudi Aramco seawater transportation pipeline network consists of thousands of kilometers of pipelines with various diameters, pressures, and flow rates. To monitor the treatment effectiveness and optimize the treatment program of biocides, the samples are collected from various downstream locations of the pipeline network to monitor the biocide residual concentration and microbial counts. Traditionally, the biocide residual concentration was determined using commercial tests kits such as Solvay THPS Kit and HACH Glutaraldehyde Test Kit [14-15]. However, sample collection, delivery, and analysis for biocide residual monitoring is a huge challenge for this large seawater injection system, especially for remote injection wells. More than often, the samples collected at the estimated biocide arrival time at the downstream locations showed no biocide residuals, one of the reasons being the difficulty to accurately estimate the biocide travel time due to the complexity of the pipeline network (diameters, branches, etc.) and flow fluctuation. An online analyzer that detects THPS biocide automatically will provide a real time monitoring of residual concentration at downstream locations of a large pipeline network, eliminating the needs and challenges for manual sampling and analysis.

The permanganate-THPS reaction was validated to be feasible to be developed into an online analyzer for real-time monitoring of THPS-based biocides [8,16]. In this paper we will demonstrate the design, construction, and validation of an online analyzer for automatic detection and quantification of THPS-based biocides with appropriate detection range and measurement accuracy.

Materials and Methods

Bis[tetrakis(hydroxymethyl)phosphonium] sulfate (THPS) solution (70-75% in H_2O) (Cat. No. 15175), potassium permanganate (2 mM) (Cat. No. 160322), and hydrochloric acid solution (1.0 M) (Cat. No. H9892) were purchased from Sigma-Aldrich. The biocide products (BT4535 and RO-IM-B276) used in the experiments are supplied by Saudi Aramco vendors. BT4535 contains 30-60% THPS, and RO-IM-B276 contains 10-30% THPS and 10-30% glutaraldehyde (GLUT) according to the product's Material Safety Data Sheet (MSDS). Milli-Q water was from Milli-Q IQ 7005 Pure & Ultrapure Water Purification System (Merck Corporation).

Detection Principle

The detection method of THPS-based

biocides is based on absorption measurement of potassium permanganate ($KMnO_4$) solution (pH 5.0) at 525 nm [8]. THPS reacts with potassium permanganate, and decolorizes the purple permanganate solution as a function of the THPS concentration. The color change is measured by optical absorption at the maximum wavelength 525 nm. The correlation of absorption of permanganate solution and THPS concentrations fits into the following equation:

$$Y = \frac{1}{a + bX}$$

Where, Y is the peak height of absorption signal; X is the concentration of THPS biocide (ppm); The calibration factors a and b are determined using a 2-point calibration procedure (Figure 1).

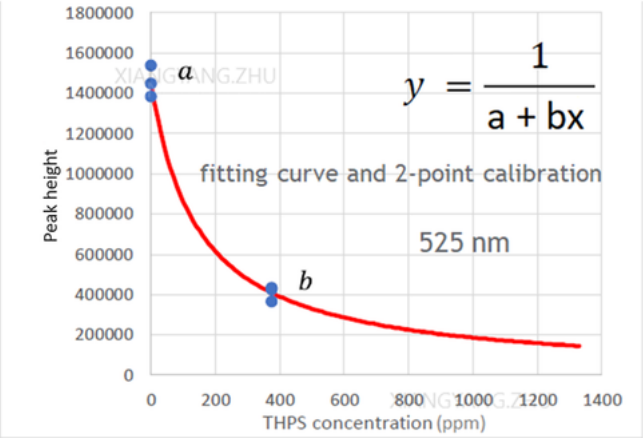

Figure 1: Correlation of permanganate absorption and THPS concentration based on 2-point calibration.

The method was validated for pure THPS and THPS-containing biocide product in fresh water and Arabian Gulf Seawater (AGS) using lab-based absorption measurement equipment, and further validated in a mock-up system equipped with dedicated flow-through system with reaction chamber and the absorption spectrometer [8].

Design of the THPS Analyzer

The validated detection principle (permanganate-THPS reaction) was used in the design of online analyzer for detection and measurement of THPS-based biocides. The analyzer design is based on the principle of a Flow Injection Analysis (FIA) system (Figure 2). A peristaltic pump draws either seawater (SW) sample or calibration fluid (known concentration of THPS-based biocide formulation) through a 3-way valve. The reagent (permanganate solution) is injected via a 6-way valve to the stream of SW or calibration fluid, and flow to the reaction coil for thorough mixing and reaction. The reaction mixture flows through a de-bubbler to remove any bubbles from the chemical reactions and/or de-pressurized SW sample, and then through the absorbance flow cell (Z-cell) for absorption measurement of permanganate at 525 nm. The optical configuration for the Z-cell is illustrated in Figure 3.

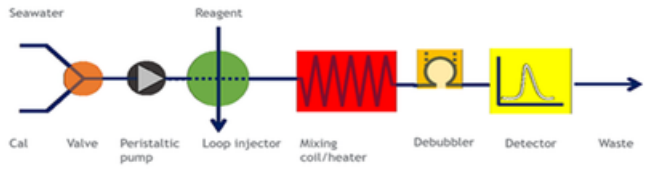

Figure 2: Schematic of the THPS Analyzer flow system.

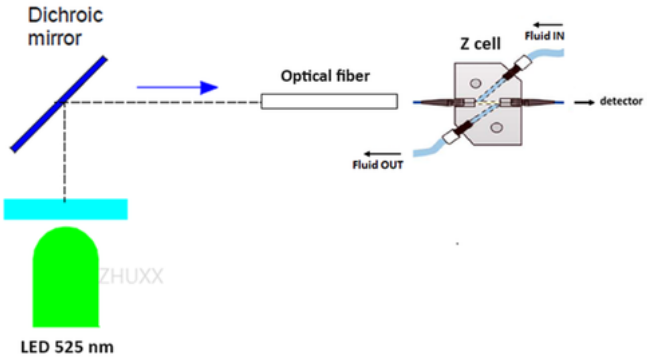

Figure 3. Optical detection of the THPS Analyzer, showing the Z-cell configuration for absorption measurement.

A quick experiment was conducted to confirm the relationship of absorption of

permanganate reagent and various THPS concentrations using the system described above. The research grade 70-75% THPS solution was prepared at 0 to 750 ppmv in the filtered Qurayyah AGS. 1.2 mM of acidified permanganate solution ($KMnO_4$·HCl, pH 5.0) was prepared in demineralized water. Using experiment conditions summarized in Table 1, the experiment confirmed the detection of THPS based on permanganate reaction with dynamic detection range 0-800 ppmv or better (Figure 4).

Table 1. Reaction conditions for absorption measurement.

Parameter	Value
Reaction temperature	40°C
Sample flow rate	150 µl/min
Injection volume (reagent)	50 µl
Reagent	$KMnO_4$ solution (1.2 mM) in 0.1M HCl
Length of reaction coil	1 m
Measurement cycle	12 min
Measurement time	6 min
Absorbance measurement	525 nm

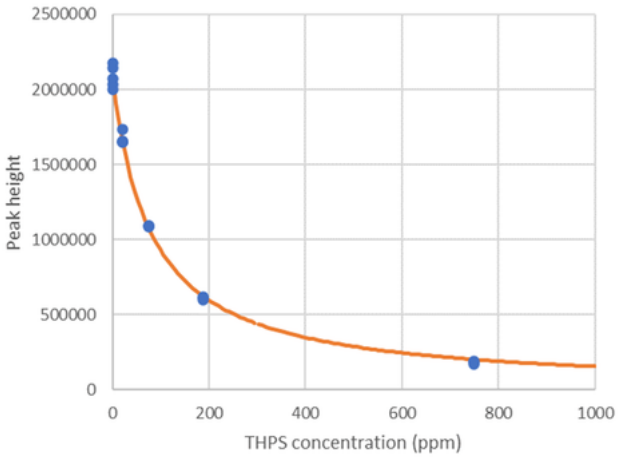

Figure 4. Measurements of various THPS concentrations based on absorption of permanganate reagent.

Construction of the THPS Analyzer

The THPS Analyzer is constructed with back-to-back mounted cabinets (Figure 5). The front cabinet houses the wet part of the system, containing the processing fluids, flow cell, reaction coils and heater, de-bubbler, valves, and pump (Figure 6). The back cabinet encloses the electronic parts of the equipment, including the control printed circuit boards (PCBs), the optical interfaces, the vacuum pump for the de-bubbler and the power supply (Figure 7).

The liquid flow and reaction in the THPS Analyzer are briefly described. During calibration cycle or sample measurement cycle, the peristaltic pump draws calibration solution (known concentration of THPS-based biocide formulation) or SW sample (or any other water sample), respectively, via a 3-way valve to 6-way valve (Figure 8). The micropump injects 50 µl of reagent (1.0~1.2 mM $KMnO_4$ solution, pH 5.0) into the stream of calibration solution or SW sample. The calibration solution or THPS-containing SW sample and the reagent are mixed thoroughly and react at 40°C when they move through the reaction coil (1 meter) (Figure 9). The mixed reaction fluid passes the de-bubbler (100 µl capacity, -0.99 barg vacuum pump) for removing bubbles in the SW stream or from the reaction of THPS and Potassium Permanganate. The de-gassed reaction fluid then flows through the Z-cell to the waste container. While flowing through the Z-cell, the absorption maximum of permanganate is measured at 525 nm. The net absorption peak signals at 0 ppmv (1st point) and another known concentration (2nd point) of THPS biocide are used to calculate the calibration factors a and b, and calibration equation (Figure 1). For unknown samples, the net absorption peak signals are used to determine the concentration of THPS-based biocide using calibration equation.

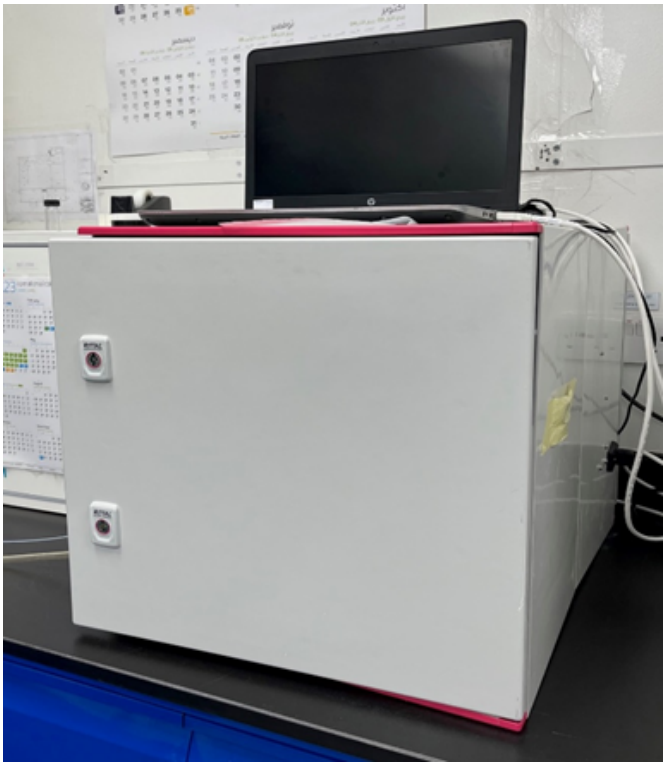

Figure 5. The THPS Analyzer, door closed.

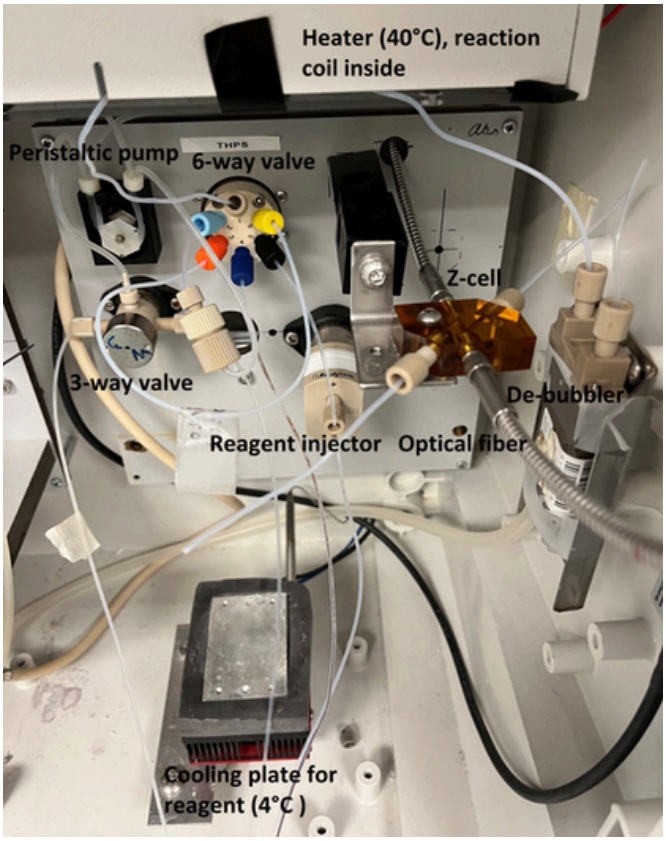

Figure 6. The THPS Analyzer with front door opened, showing liquid flow system.

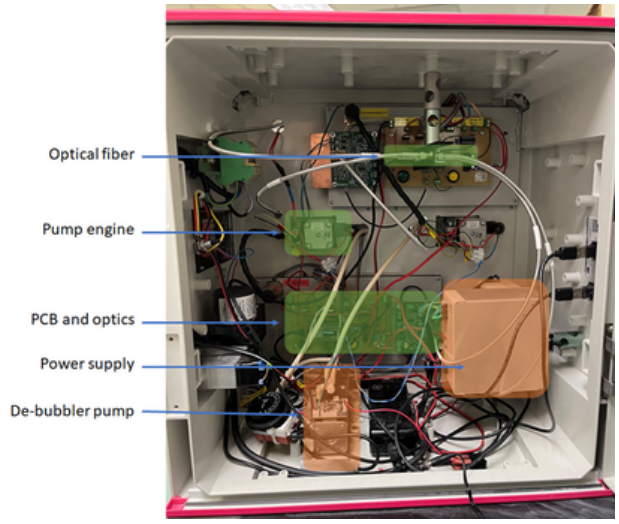

Figure 7. The THPS Analyzer with back door opened, showing electronic parts.

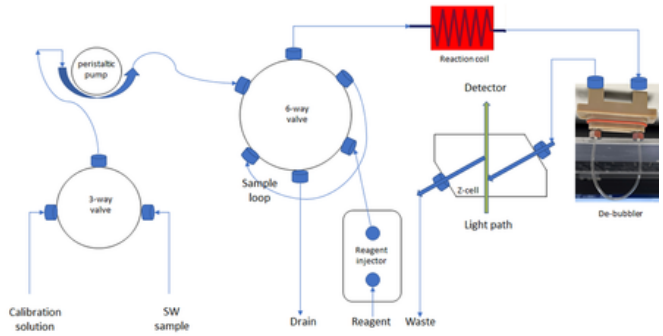

Figure 8. Schematic drawing of the THPS Analyzer's liquid flow system, showing flow direction of reagent, sample, and calibration solution.

Figure 9. Schematic view of permanganate injected into the stream of the calibration solution or SW sample, before (left) and after (right) knitted reaction coil.

The procedure for 2-point calibration is briefly described as following. The THPS Analyzer is connected to the SW sample, and the SW stream flows through the analyzer continuously. At the calibration cycle, the reagent (permanganate solution) is injected into the SW stream (containing 0 ppmv biocide), passes reaction coil for thorough mixing and reaction of THPS and permanganate. The mixed solution passes the de-bubbler and then Z-cell, where the absorption of the permanganate is

measured at 525 nm. The net absorption signals (peak height, PH) are calculated by subtracting the average baseline (BL) signals. The factor a is then determined.

$$a = \frac{1}{PH_0}$$

Next, a SW sample containing known concentration of THPS-based biocide formulation is prepared, e.g., a 625 ppmv biocide sample. The analyzer carries out the same measurement process, and obtains an absorption PH signal of permanganate. The factor b is now determined.

$$b = \frac{\frac{1}{PH_{625}} - a}{625}$$

Laboratory Acceptance Tests

The constructed THPS Analyzer has undergone extensive laboratory acceptance tests to check hardware and software functionalities, and determine the dynamic range, measurement repeatability (Relative Standard Deviation, RSD) and accuracy using commercial biocide products. The predefined criteria for passing the acceptance tests are <10% variation (RSD) for measurement repeatability and within ±20% for measurement accuracy when compared to the calculated value (Table 2).

Table 2. Predefined criteria for passing the acceptance tests of the THPS Analyzer.

Criteria		THPS Analyzer
Detection range	as active	20 – 800 ppm THPS
	as product	80-2000 ppm product
Repeatability (RSD)	peak height	<10%
Accuracy (%)	as active	±20% @ 20 ppm
		±20% @ 400 ppm
		±20% @ 800 ppm
	as product	±20% @ 100 ppm
		±20% @ 1000 ppm
		±20% @ 2000 ppm

Two biocide products (BT4535 and RO-IM-B276) were used for both calibration curve and acceptance tests. The neat biocide products are considered as 100% or 1,000,000 ppmv, and a series of dilutions was prepared in Qurayyah seawater (QSW) for calibration curves, dynamic detection range, 2-point calibrations, and acceptance tests at low, medium and high concentrations (Table 3). The concentrations of active ingredient THPS in Table 3 were estimated based on the average of active concentration range. THPS-based product BT4535 was diluted to 44-2222 ppmv of biocide product (20-1000 ppmv THPS active), and RO-IM-B276 diluted to 80-4000 ppmv of biocide product (16-800 ppmv THPS active). The concentration of the prepared biocide samples based on the product dilution is designated as calculated concentration. The low-medium-high concentrations for the acceptance tests are in the range of 90 to 2000 ppmv of biocide products (20-800 ppmv of THPS active), which cover the concentration range in the biocide injection practices. The measurement conditions in the acceptance tests were described in Table 1.

Table 3. Preparation of biocide products for various tests.

BT4535	product ppmv	THPS ppmv	RO-IM-B276	product ppmv	THPS ppmv
Calibration curve with detection range	44	20	Calibration curve with detection range	80	16
	111	50		200	40
	444	200		800	160
	1111	500		2,000	400
	2222	1000		4,000	800
2-point Cal.	556	250	2-point Cal.	625	125
Low	89	40	Low	100	20
Medium	889	400	Medium	1,000	200
High	1778	800	High	2,000	400

Measurement repeatability

To determine the peak-to-peak measurement variation/repeatability of the THPS Analyzer, two batches of $KMnO_4$·HCl reagent were prepared. Each batch was prepared using 10 ml of 2 mM $KMnO_4$ solution (Sigma Cat. No. 160322), 6.67 ml ultrapure water, and 3.34 ml 1 M HCl solution. 200 ppmv THPS was prepared as

calibration solution from 70% THPS solution in water (Sigma Cat. No. 15175). In order to obtain 200 ppmv THPS, 70% THPS solution was first diluted 100 times in ultrapure water and then further diluted 35 times in Qurayyah seawater. 200 ppmv THPS was used for 2-point calibration procedure to determine the factors a and b (Table 4). Both batches of permanganate reagent were used in two series of 6 blank seawater injections to determine the peak-to-peak measurement variation. The results indicated that the peak-to-peak variation (RSD) is less than 10%, and the measured THPS concentration of blank seawater is around 0 ppmv. (Table 5).

Table 4. Calibration measurement; Calibration solution: 200 ppmv THPS in seawater.

	Peak value (blank)	Peak value (200 ppmv THPS)	Factor a	Factor b
Batch 1	663598	177006	1.51E-06	2.07E-08
Batch 2	665012	171163	1.50E-06	2.17E-08

Table 5. Measurement peak-to-peak variation for seawater blanks with 2 batches of $KMnO_4$ reagent.

Calibration curve and measurement accuracy

BT4535 biocide

The calibration curve and dynamic detection range for the THPS-based biocide BT4535 was shown in Figure 10. The detection range of the THPS Analyzer is at least 0-2222 ppmv of biocide BT4535, which is approximately 0-1000 ppmv of THPS (assuming the average THPS concentration in the formulation is 45%). The measurement repeatability (RSD) of absorption peak height is between 1.2-4.7% among the triplicate measurements at the concentration up to 444 ppmv BT4535 (Table 6), meeting the smaller than 10% criterion (Table 2). At higher concentration (1111 and 2222 ppmv), the measurement variation is more than 10%.

A 2-point (0 ppmv and 556 ppmv) calibration procedure was used to determine the factor a and b, and the calibration fitting equation for biocide BT4535 (Figure 11). Three freshly prepared BT4535 solutions at low, medium, and high concentrations (89, 889, and 1778 ppmv) were measured in triplicate using THPS Analyzer to determine the measurement repeatability and accuracy (Table 7). The measurement repeatability (RSD) for the absorption peak height is between 3.7-6.6% among the triplicate measurements, which meets the <10% criterion (Table 2). The measurement accuracy (relative error) of the calculated vs. measured values at low, medium, and high concentrations of BT4535 are within ±14%. This also meets within ±20% criterion (Table 2). In conclusion, the measurement of biocide BT4535 passed the predefined criteria for the acceptance tests.

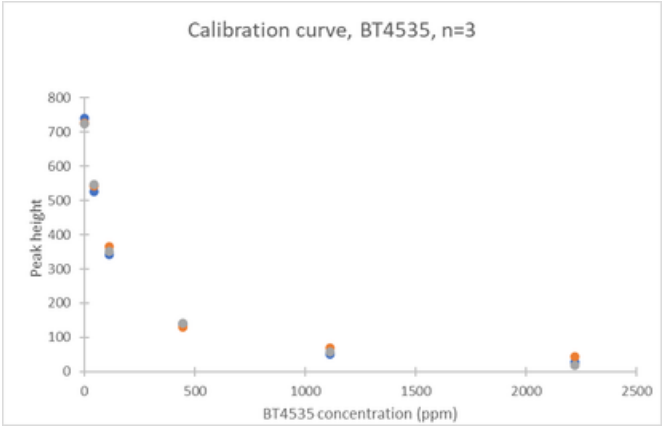

Figure 10. Calibration curve and dynamic detection range for BT4535 biocide (n=3).

Table 6. Measurement repeatability (RSD) of BT4535 biocide.

Calculated ppmv, BT4535	Peak height (PH)		
	Mean, n = 3	Stdev	RSD (%)
0	729.0	8.7	1.2%
44	538.0	10.6	2.0%
111	352.7	12.2	3.5%
444	136.3	6.4	4.7%
1111	59.3	9.1	15.3%
2222	30.3	12.7	41.7%

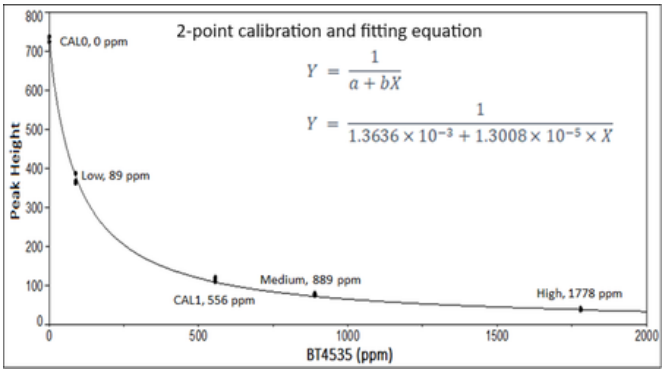

Figure 11. 2-point calibration and fitting equation for BT4535 biocide (n=3).

Table 7. Measurement repeatability (RSD) and accuracy of BT4535.

Validation w/ 2-point calibration	Peak height (PH)			BT4535 ppmv		Accuracy (%)
	mean, n = 3	Stdev	RSD (%)	Calculated	Measured	Calc. vs measured
Low	372.3	13.8	3.7%	89	101.6	14.2%
Medium	78.0	3.0	3.8%	889	880.8	-0.9%
High	40.0	2.6	6.6%	1778	1817.1	2.2%

RO-IM-B276 biocide

The calibration curve and dynamic detection range for the THPS-based biocide RO-IM-B276 was shown in Figure 12. The detection range of the THPS Analyzer is at least 0-4000 ppmv of biocide RO-IM-B276, which is approximately 0-800 ppmv of THPS (assuming the average THPS concentration in the formulation is 20%). The measurement repeatability (RSD) of absorption peak height is between 0.5-7.6% among the triplicate measurements at the concentration range of 0-4000 ppmv RO-IM-B276 (Table 8), meeting the smaller than 10% criterion (Table 2).

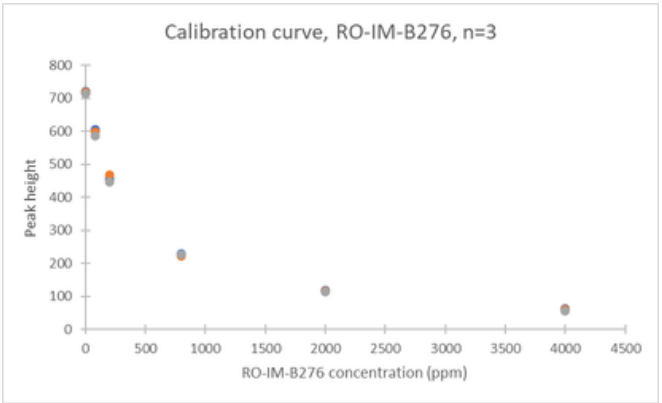

Figure 12. Calibration curve and dynamic detection range for RO-IM-B276 biocide (n=3).

Table 8. Measurement repeatability (RSD) of RO-IM-B276 biocide.

Calculated ppmv, RO-IM-B276	Peak height (PH)		
	mean, n = 3	Stdev	RSD (%)
0	718.0	3.6	0.5%
80	596.3	10.3	1.7%
200	457.0	10.5	2.3%
800	225.7	4.5	2.0%
2000	116.3	2.5	2.2%
4000	60.0	4.6	7.6%

A 2-point (0 ppmv and 625 ppmv) calibration procedure was used to determine the factor a and b, and the calibration fitting equation for biocide RO-IM-B276 (Figure 13). Three freshly prepared RO-IM-B276 solutions at low, medium, and high concentrations (100, 1000, and 2000 ppmv) were measured in triplicate using THPS Analyzer to determine the measurement repeatability and accuracy (Table 9). The measurement repeatability (RSD) for the absorption peak height is between 0.8-4.3% among the triplicate measurements, which meets the <10% criterion (Table 2). The measurement accuracy (relative error) of the calculated vs. measured values at low, medium, and high concentrations of RO-IM-B276 are within ±1.0%. This also meets within ±20% criterion (Table 2). In conclusion, the measurement of biocide RO-IM-B276 passed the predefined criteria for the acceptance tests.

It is noted that biocide RO-IM-B276 also contains 10-30% GLUT. The results indicated that the presence of GLUT has no effect on the accurate measurement of THPS-based biocide.

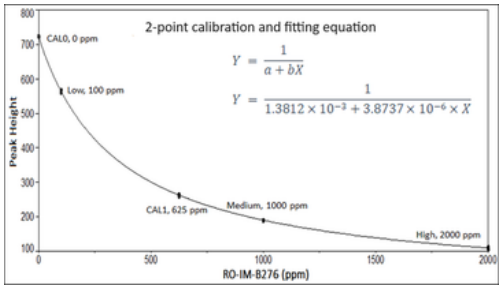

Figure 13. 2-point calibration and fitting equation for RO-IM-B276 biocide (n=3).

Table 9. Measurement repeatability (RSD) and accuracy of RO-IM-B276.

Validation w/ 2-point calibration	Peak height (PH)			RO-IM-B276 ppmv		Accuracy (%)
	mean, n = 3	Stdev	RSD (%)	Calculated	Measured	Calc. vs measured
Low	566.0	4.4	0.8%	100	99.5	-0.47%
Medium	190.3	2.1	1.1%	1000	999.7	-0.03%
High	108.7	4.7	4.3%	2000	2019.1	0.95%

Biocide slug simulation

Biocide batch treatment is most common in oil and gas industry for various reasons. If applied properly, it can be more cost-effective and achieve the same goal as the continuous treatment for microbial control. In typical batch treatment, 250-1500 ppmv of biocide is injected into the target water system at a pre-determined frequency (weekly being the most common) and for a pre-determined period of time (1-4 hours being the most common) [17]. In some oil companies, two biocides with different chemistries are used, alternating on weekly basis, for the purpose to avoid or delay the development of bacterial resistance or selection against the biocides.

Under the batch treatment, when the water system contains no THPS biocide slug, the analyzer is programmed to conduct the measurement cycles at longer intervals to save the reagents; however, when the analyzer detects the arrival of the biocide slug, it shall automatically switch to slug detection mode in order to measure THPS biocide residuals as many times as possible before the biocide slug passes the analyzer.

The logic for deciding between slug and non-slug mode was implemented in the control software by means of a comparator function on the calculated concentration of THPS biocide in ppmv. After each measurement the log output was compared to the comparator function and one of the decisions was made by the software as the following:

- System in non-slug mode - system stays in non-slug mode
- System in non-slug mode - system goes to slug mode
- System in slug mode - system stays in slug mode
- System in slug mode - system goes to non-slug mode

THPS biocide slug simulation was performed as part of acceptance tests. The comparator function was set at 80 ppmv ± 20% (i.e., ± 16 ppmv) of BT4535 biocide. While running the analyzer with blank seawater, a sample of BT4535 biocide was added to the blank seawater, aiming at an approximate product concentration of > 80 ppmv. Following the measurement of the spiked seawater, the sample supply was reverted to blank seawater and the next measurement was performed. During these alternations of biocide addition and removal, it is expected that the control software will switch between slug and non-slug mode automatically based on the measured biocide concentration compared to the pre-set comparator function 80 ± 16 ppmv. Table 10 showed the results of biocide (BT4535) slug simulation experiment. The results indicated that the software made the correct decision, switching the analyzer between slug and non-slug measurement mode based on the comparison of the set comparator function and the measured concertation of BT4535 biocide.

Table 10. Slug and non-slug measurements of BT4535 biocide.

Sample	Detected BT4535 (ppmv)	Status/Change observed
SW/blank	< 64	non-slug
Added BT4535	> 96	non-slug -> slug
Remained on BT4535	> 96	slug
SW/blank	< 64	slug -> non-slug
Added BT4535	> 64	non-slug -> slug
Remained on BT4535	> 96	slug
SW/blank	< 64	slug -> non-slug
Added BT4535	> 96	non-slug -> slug
Remained on BT4535	> 96	slug
SW/blank	> 64	slug
SW/blank	< 64	slug -> non-slug
Added BT4535	< 64	non-slug
Added BT4535	> 96	non-slug -> slug
Added BT4535	< 64	slug -> non-slug
SW/blank	< 64	non-slug

Conclusions of acceptance tests

The laboratory acceptance tests aim to check hardware and software functionalities, determine the dynamic measurement range, measurement repeatability (RSD) and accuracy using commercial biocide products. The predefined criteria for the acceptance tests are <10% measurement variation (RSD) and ±20% for measurement accuracy when compared to the calculated value (Table 2).

- Table 11 summarizes the outcomes of acceptance tests using 2 THPS-based commercial biocide products. The measurement of THPS-based BT4535 and RO-IM-B276 passed the predefined criteria for detection concentration range, measurement repeatability, and accuracy. The acceptance tests also concluded that the comparator logic performed as expected, i.e., the software switched from non-slug mode to slug mode and vice versa upon crossing the threshold of 80 ppmv ± 20% biocide concentration.

Table 11. Summary of the laboratory acceptance tests of the THPS Analyzer.

Biocide	Criteria	Detection range (ppmv)	Repeatability (RSD)	Accuracy (%)	Acceptance tests
				calc. vs measured	
		80-2000	<10%	±20%	
BT4535	Calibration curve	0-2222	1.2-41.7%	-	Pass
	Validation at L/M/H*	89/889/1778	3.7-6.6%	-0.9~14.2%	
RO-IM-B276	Calibration curve	0-4000	0.5-7.6%	-	Pass
	Validation at L/M/H	100/1000/2000	0.8-4.3%	-0.03~1.0%	

*L/M/H: low-medium-high concentration of biocide product

Conclusions

This paper described the design, construction, and validation of an online analyzer for automatic detection and quantification of THPS-based biocides. The analyzer is based on the absorption measurement of potassium permanganate solution (pH 5.0) at the maximum wavelength 525 nm for THPS detection and quantification. The THPS Analyzer has undergone extensive laboratory acceptance tests with the predefined criteria (dynamic detection range, measurement repeatability and accuracy) using commercial biocide products. The analyzer showed the dynamic detection range of 80-2000 ppmv of biocide formulation (or 20-800 ppmv of THPS). The measurement repeatability is less than 10% variation in terms of relative standard deviation (RSD), and the measurement accuracy is within ±20% of the actual biocide concentration. In addition, the THPS Analyzer can automatically switch between non-slug mode and slug mode measurement depending on the measured biocide concentration and the pre-set comparator parameters. The THPS Analyzer is currently under the field demonstration with aims to determine the analyzer's robustness in a real seawater system, identify technical issues, solutions, and improvement areas to be incorporated into the industrial version of THPS Analyzer.

References

1. Cotruvo, J.A. (2005). Water Desalination Processes and Associated Health and Environmental Issues. Magazine - Water Condition & Purification, January 2005.
2. Vance, I. and Thrasher, D.R. (2005). Reservoir Souring: Mechanisms and Prevention. In Petroleum Microbiology. B. Ollivier and M. Magot, Editors. Washington, DC: ASM Press. p. 123-142.
3. Passman, F.J. (2013) Microbial contamination and its control in fuels and fuel systems since 1980 - A review, International Biodeterioration & Biodegradation, (81): 88-104.
4. Agarry, S.E., Salam, K.K., Arinkoola, A.O., and Soremekun, I.O. (2015). Microbiologically Influenced Corrosion of Mild Steel in Crude Oil Environment. European Journal of Engineering and

Technology 3(6):40-58.
5. Amaya Hernandez, S.P., Wadei, A.H., Huwaiji, N.K., and Zhu, X.Y. (2018). Microbial Corrosion Risk Assessment in Crude Oil Trunk Lines: A Case Study. Paper No. MECCOCT18-12322. Proceedings of 17th Middle East Corrosion Conference (MECC). Kingdom of Bahrain
6. Campbell, C. (2017). Advances in testing and monitoring of biocides in oil and gas. In Trends in Oil and Gas Corrosion Research and Technologies : Production and Transmission. A.M. El-Sherik (Ed.). Woodhead Publishing, Duxford, pp. 489-511.
7. Keasler, V., De Paula, R., Nilsen, G., et al. (2017). Biocides overview and applications in petroleum microbiology. In Trends in Oil and Gas Corrosion Research and Technologies: Production and Transmission. A.M. El-Sherik (Ed.). Woodhead Publishing, Duxford, pp. 539-562.
8.Zhu, X., Grigoryan, A. and Saleh, M. A. (2025). Developing and Validating Method for Online Monitoring of THPS-Based Biocides. JCRIS 2(2):4-9.
9. Zhu, X., Grigoryan, A. and Saleh, M. A. (2025) Online Monitoring Method for Glutaraldehyde-Based Biocides in Large Seawater Injection Network. JCRIS 2(4):13-21.

Acknowledgment

The authors would like to acknowledge the Saudi Arabian Oil Company (Saudi Aramco) for granting permission to publish this paper.

Authors

Dr. Xiangyang Zhu has over 25 years of experience in teaching, R&D, and technical services in academia, research institute, and energy industries. He is a pioneer in introducing modern molecular microbiology technologies into oil and gas industry. Currently he is a Research Science Consultant at Research and Analytical Services Department of Saudi Aramco.

Dr. Alexander Grigoryan holds a Ph.D. in microbiology from the Russian Academy of Sciences. With international experience in Russia, Canada, and Denmark, his research expertise includes reservoir souring, microbially induced corrosion, and enhanced oil recovery. He has co-authored over 30 peer-reviewed publications.

Mazen Alsaleh has over 30 years of research and technical services experience in petrochemicals and oil & gas industries. His research work covers modern molecular microbiology, microbially induced corrosion and downhole microbiology. Currently he is the Manager of the Materials and Corrosion Services Division in Saudi Aramco.

Editorial Board

Dr. Shakeel Ahmed (Editor in Chief)

Dr. Shakeel Ahmed is a Research Scientist at the IRC for Refining & Advanced Chemicals at King Fahd University of Petroleum & Minerals. His primary areas of expertise include industrial catalysis, inorganic synthesis, and instrumental analysis. With over 200 publications and 77 co-invented patents to his name, Dr. Shakeel has made significant contributions to his field. He has been honored with numerous national and international awards and is recognized among the top 2% of scientists worldwide.

Dr. SK Safdar Hossain

Dr. SK Safdar Hossain is a Professor of Chemical Engineering at King Faisal University. He earned his Ph.D. in Catalysis from King Fahd University of Petroleum & Minerals (KFUPM). His research focuses on reaction engineering, energy storage devices, and chemical process control. He has published over seventy-five peer-reviewed articles and is a co-inventor on fifteen United States patents. Dr. Hossain is a Senior Member of the American Institute of Chemical Engineers (AIChE) and a Life Member of the Indian Institute of Chemical Engineers (IIChE).

Dr. Mansour Saleh Alturki

Dr. Mansour Saleh Alturki, Assistant Professor of Medicinal Chemistry at Imam Abdulrahman Bin Faisal University, specializes in synthetic chemistry and drug discovery targeting metabolic disorders, infectious diseases, and cancer. With 23+ years of experience, his expertise includes computational drug design, ADMET profiling, molecular dynamics, and AI-driven research in human health innovations.

Ms. Hissah Alqahtani

Ms. Hissah Alqahtani is a Lecturer in Physical Chemistry at Al Yamamah University, specializing in electrochemistry and advanced materials for energy and environmental applications. With expertise in corrosion, supercapacitors, solar cells, and water treatment, she has published extensively and holds three patents in these fields. Ms. Alqahtani is also a reviewer for international scientific journals, including the Molecular Structure Journal and Springer Nature.

Partners & Sponsors

" Together, advancing the frontiers of chemistry for a better tomorrow "

PRINICIPAL

Diamond

STRATEGIC PARTNERS

THE JOURNAL OF CHEMICALS RESEARCH & INNOVATION SOCIETY

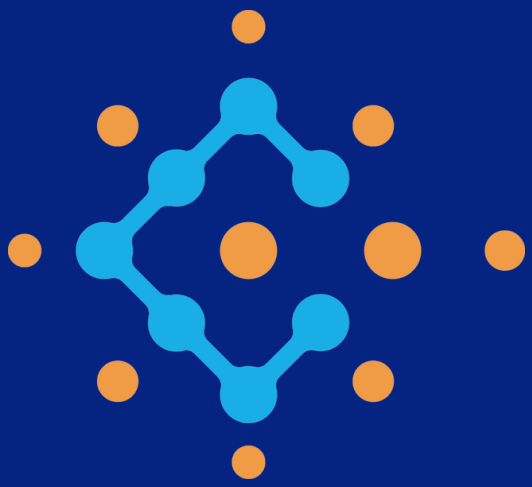

editorial@cris.org.sa

www.cris.org.sa

@chemreain